

# Near Infrared Polarimetry A Tool for Testing Properties of Sagittarius A\*

INAUGURAL-DISSERTATION

zur  
Erlangung des Doktorgrades  
der Mathematisch-Naturwissenschaftlichen Fakultät  
der Universität zu Köln



vorgelegt von

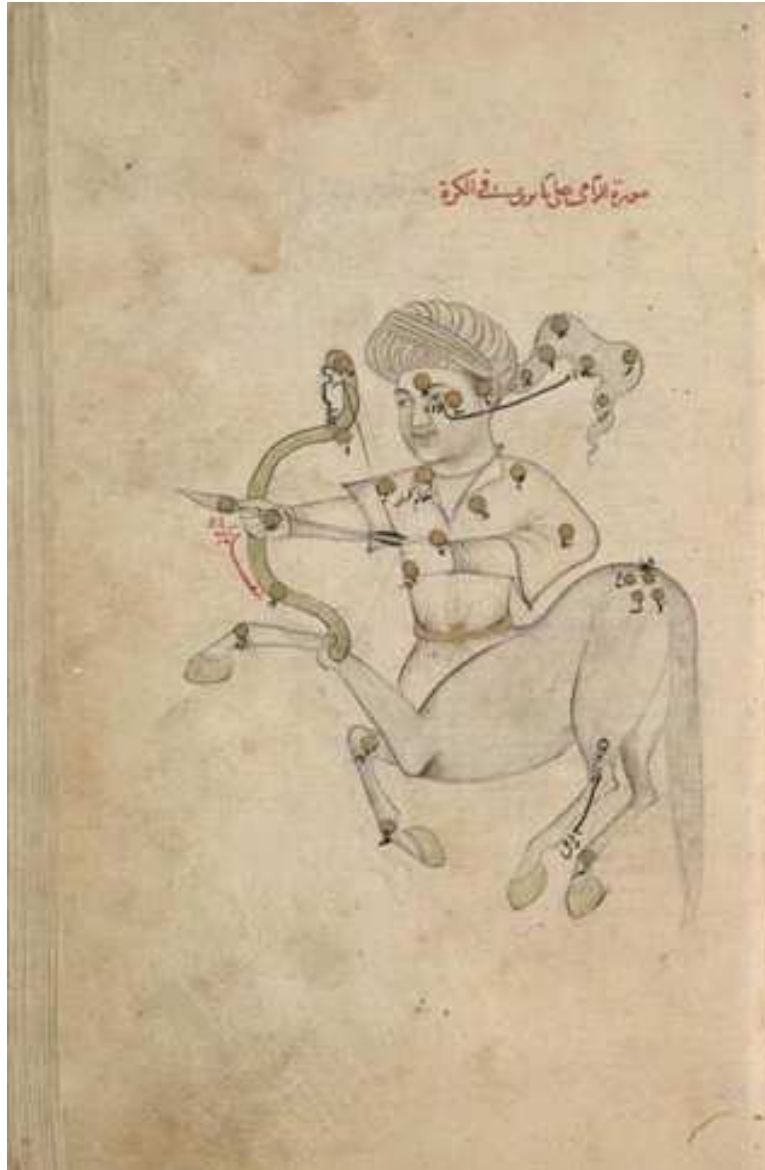
**Mohammad Zamaninasab**  
aus TorbateJam, Iran

Köln 2010

Berichterstatter:

Prof. Dr. Andreas Eckart  
Prof. Dr. J. Anton Zensus

Tag der letzten mündlichen Prüfung: 19 April 2010



*The constellation Sagittarius (Credit: Abdul Rahman Sufi (903 AD -986 AD). Kitab su-war al-kawakib (Book on the Constellations of Fixed Stars, 964)).*



## Abstract

In this thesis I focus on the results of the data modelings and simulations of near-infrared (NIR) observations of the Sagittarius A\* (Sgr A\*) counterpart associated with the super-massive black hole at the Galactic Center (GC).

My goal is to investigate and understand the physical processes behind the variability associated with the NIR flaring emission from Sgr A\*. The NIR observations have been carried out using the NACO adaptive optics (AO) instrument at the European Southern Observatory's (ESO's) Very Large Telescope (VLT) and the CIAO NIR camera on the Subaru telescope (13 June 2004, 30 July 2005, 1 June 2006, 15 May 2007, 17 May 2007 and 28 May 2008). I used a model of synchrotron emission from relativistic electrons in the inner parts of an accretion disk. The relativistic simulations have been carried out using the Karas-Yaqoob (KY) ray-tracing code. I also probed the existence of a correlation between the modulations of the observed flux density light curves and changes in polarimetric data. Furthermore, I confirmed that the same correlation is also predicted by the so-called hot spot model. Correlations between intensity and polarimetric parameters of the observed light curves, as well as a comparison of predicted and observed light curve features through a pattern recognition algorithm result in the detection of a signature of orbiting matter under the influence of strong gravity. This pattern is proved to be statistically significant against randomly polarized red noise.

The observed correlations between flux modulations and changes in linear polarization degree and angle can be a sign that the NIR flares have properties that are not expected from purely random red-noise. I found that the geometric shape of the emitting region plays a major role in the predictions of the model. From fully relativistic simulations of a spiral shaped emitting region, I concluded that the observed swings in polarization angle during NIR flares support the idea of compact orbiting spots instead of extended patterns. The effects of gravitational shearing, fast synchrotron cooling of the components, and confusion from a variable accretion disk have been taken into account.

Furthermore, I discussed the expected results from future observations of VLT interferometry (VLTI) like the GRAVITY experiment. Simulated centroids of NIR images led me to the conclusion that a clear observation of position wander of the center of NIR images with future infrared interferometers will prove the existence of orbiting hot spots in the vicinity of our Galactic super-massive black hole.

Finally, I described a novel approach to constrain the physical parameters of the Galactic black hole by using time resolved NIR polarimetric observations. Even though

basically the method is developed for Sgr A\*, it can be used to test intrinsic properties of several types of compact objects with QPO behavior.

---

## Zusammenfassung

Der Fokus dieser Arbeit liegt auf der Modellierung und Simulation von Nahinfrarot-Beobachtungen (NIR-Beobachtungen) der Quelle Sagittarius A\* (Sgr A\*), die mit dem supermassereichen Schwarzen Loch im Galaktischen Zentrum (GC) assoziiert ist.

Mein Ziel ist es, die physikalischen Prozesse zu untersuchen und zu verstehen, die hinter der Variabilität der nahinfraroten (NIR) Emission dieser Quelle stehen. Die NIR-Beobachtungen wurden mit NACO, einem Instrument mit adaptiver Optik am Very Large Telescope (VLT) der Europäischen Südsternwarte (ESO), und mit der CIAO NIR-Kamera am Subaru Telescope (13. Juni 2004, 30. Juli 2005, 1. Juni 2006, 15. Mai 2007, 17. Mai 2007 und 28. Mai 2008) durchgeführt. Ich habe ein Modell für die Beschreibung von Synchrotronemission relativistischer Elektronen in den inneren Regionen von Akkretionsscheiben verwendet. Die relativistischen Simulationen wurden mit Hilfe des Karas-Yaacob-„ray-tracing“-Kodes (KY-Kode) durchgeführt. Darüber hinaus habe ich die Existenz einer Korrelation zwischen den Modulationen der beobachteten Flussdichtelichtkurven und der Veränderungen der polarimetrischen Daten untersucht. Hierbei habe ich bestätigen können, dass diese Korrelation eine der Voraussagen des „Hot Spot“-Modells ist. Statistische Untersuchungen der Korrelationen zwischen Intensität und polarimetrischen Parametern der beobachteten Lichtkurven, sowie der Vergleich zwischen prognostizierten und beobachteten Lichtkurven mittels einer Mustererkennungsanalyse ergaben die Detektion einer typischen Signatur von Materie, die unter dem Einfluß extremer Gravitation akkretiert wird. Diese Signatur wurde gegen zufällig verteiltes rotes Rauschen getestet und statistisch signifikant detektiert.

Die beobachteten Zusammenhänge zwischen den Modulationen des Flusses und den Veränderungen des Grades der linearen Polarisation und des Positionswinkels können ein Hinweis dafür sein, dass die NIR-Flares Eigenschaften haben, die nicht von reinem roten Rauschen erwartet werden. Ich habe herausgefunden, dass die geometrische Gestalt der emittierenden Region eine große Rolle in den Vorhersagen des Modells spielt. Relativistische Simulationen emittierender Regionen mit spiralförmiger Form ergaben, dass das beobachtete Durchlaufen aller Polarisationswinkel während der NIR-Flares die Idee auf einem Orbit kreisender Knoten (Spots) gegenüber ausgedehnter Strukturen stark unterstützt. Der Effekt der gravitativen Scherung, eine schnelle Kühlung der Komponenten durch Synchrotron-Strahlung und ihre Konfusion in einer stets veränderlichen Akkretionsscheibe wurden berücksichtigt.

Desweiteren diskutiere ich die Ergebnisse, die man von zukünftigen Beobachtungen mit interferometrischen Instrumenten am VLT, wie z.B. dem GRAVITY-Experiment, erwarten darf. Die simulierten Helligkeitsschwerpunkte der zu erwartenden NIR-Bilder ergaben, dass eine klare Beobachtung der Positionsveränderungen dieser Zentroide

mit zukünftigen Interferometern im Infrarot-Bereich möglich sein sollten und die Existenz kreisender „Hot Spots“ in der Umgebung unseres galaktischen supermassereichen Schwarzen Lochs neu beleuchtet zur Diskussion stellen werden.

Schließlich beschreibe ich einen neuen Ansatz, wie es möglich ist, durch hochzeit aufgelöste polarimetrische NIR-Beobachtungen die physikalischen Parameter des galaktischen Schwarzen Lochs auf einen kleinen Bereich möglicher Werte einzuschränken. Auch wenn diese Methode grundsätzlich für die Quelle Sgr A\* entwickelt wurde, ist es möglich, damit auch intrinsische Eigenschaften anderer kompakter Objekte mit quasi-periodischem Verhalten zu testen.

# Contents

<b>1</b>	<b>Introduction</b>	<b>9</b>
1.1	Black Holes . . . . .	10
1.2	The Galactic Black Hole . . . . .	16
1.3	This Thesis . . . . .	21
<b>2</b>	<b>Observations and Data Reduction</b>	<b>25</b>
2.1	NIR Polarimetry of Sagittarius A* . . . . .	26
<b>3</b>	<b>Data Analysis</b>	<b>33</b>
3.1	Timing Analysis . . . . .	33
3.1.1	Tools of Time-Series Analysis . . . . .	33
3.1.2	Application to Real Astrophysical Data . . . . .	40
3.1.3	Timing Analysis of the Sample of Polarimetric NIR Light Curves of Sgr A* . . . . .	45
3.1.3.1	Autocorrelation . . . . .	45
3.1.3.2	Periodogram . . . . .	47

---

3.2	Cross-correlation Analysis . . . . .	54
3.2.1	Importance of Polarimetry . . . . .	54
<b>4</b>	<b>Modeling</b>	<b>61</b>
4.1	Inner Parts of an Accretion Disk . . . . .	61
4.1.1	Emission Mechanisms in Sgr A* Revisited . . . . .	62
4.1.2	An Analytical Synchrotron Self-Compton Model . . . . .	65
4.2	Numerical Simulations of an Accretion Flow . . . . .	70
4.2.1	Dynamics: The Polish Doughnut . . . . .	70
4.2.2	General Relativistic Transfer Effects . . . . .	71
4.2.3	Fully Relativistic Simulations of the Accretion Flow Into Sgr A* . . . . .	80
4.3	Pattern Recognition Analysis: Signatures of Lensing Effects . . . . .	86
4.3.1	A Spotted Accretion Disk? . . . . .	87
4.4	Alternative Models . . . . .	95
4.4.1	Relativistic Echoes . . . . .	95
4.4.2	Jet Model . . . . .	95
4.4.3	A Disk Plus a Short Jet . . . . .	99
4.5	Geometry of the Emitting Region . . . . .	100
4.6	Magnetic Field Structure and Geometrical Orientation of the System . . . . .	106
<b>5</b>	<b>Next Generation of NIR Interferometry</b>	<b>111</b>
5.1	Introduction . . . . .	111
5.2	GRAVITY at Work: Implications for Sgr A* . . . . .	113

---

<b>6</b>	<b>Near Infrared Polarimetry as a Tool for Testing Properties of Black Holes</b>	<b>119</b>
6.1	Time Delay Between Polarization Channels: Predictions of the Hot Spot Model . . . . .	120
6.2	Implications for Sgr A* . . . . .	122
<b>7</b>	<b>Summary and Conclusion</b>	<b>139</b>
	<b>Bibliography</b>	<b>141</b>
	<b>List of Figures</b>	<b>155</b>
	<b>List of Tables</b>	<b>157</b>
	<b>List of Acronyms</b>	<b>159</b>
	<b>Acknowledgements</b>	<b>161</b>
	<b>Erklärung</b>	<b>163</b>



# Chapter 1

## Introduction

*In childhood we strove to go to school  
Our turn to teach, joyous as a rule  
The end of the story is sad and cruel  
From dust we came, and gone with winds cool*

-Omar Khayyám (1048 AD - 1131 AD)  
Astronomer, mathematician, philosopher,  
physician and poet.

Our galaxy, the Milky Way has been observed for a long time by astronomers. It holds a special characteristic of being the closest to us of all galaxies in the Universe, where everything else is too far away to be studied comprehensively. Moreover, the Galactic Center (GC) is one of the most studied fields in galactic astronomy. Owing to its proximity (only  $\sim 8$  Kpc away from Earth), it is possible to observe this region with very high angular resolutions. Lies in its heart one of the most fascinating targets, the (super-)massive black hole candidate Sagittarius A\*. The number of publications dedicated to this field is overwhelmingly large which is an indicator of its importance. Here in this chapter I first review some basic aspects about black holes and why they are so important and interesting for scientists, then go over some features of the GC region, specially the galactic black hole, Sagittarius A\*.

## 1.1 Black Holes

Black holes were actually anticipated by theoreticians much before any experiment showed evidence for their existence in nature. Soon after, Albert Einstein formulated general relativity in 1916 (Einstein 1916), Karl Schwarzschild found a solution of the Einstein field equations which describes a static black hole (Schwarzschild 1916). Despite the amazing predictions of this solution, it did not get a general acceptance by the scientific community in that time. However, some theoreticians continued working on that which led to the more generalized solutions for the charged (Reissner 1916, Nordström 1918), spinning (Kerr 1963) or spinning and charged (Newman et al. 1965) black holes.

The Kerr line element in the Boyer-Lindquist coordinates  $(t, r, \theta, \varphi)$  can be written as

$$ds^2 = -\left(1 - \frac{2r}{\rho^2}\right)dt^2 - \frac{4ar \sin^2\theta}{\rho^2} dt d\phi + \frac{\rho^2}{\Delta} dr^2 + \rho^2 d\theta^2 - \left[\frac{2ar \sin^2\theta}{\rho^2} - \frac{\mathcal{A} \sin^2\theta}{\rho^2}\right] d\phi^2 \quad (1.1)$$

where  $\rho^2 \equiv r^2 + a^2 \cos^2\theta$ ,  $\Delta \equiv r^2 - 2r + a^2$  and  $\mathcal{A} \equiv (r^2 + a^2)^2 - \Delta a^2 \sin^2\theta$ . Here  $a$  is the angular momentum per unit mass ( $a = \frac{J}{M}$ ). In the above equation I have used the geometrical units which means that  $G = c = 1$ . This metric describes the space-time around a massive spinning object. The most general form of a metric (the Kerr-Newmann metric) takes the charge of the object into account. However, for most astrophysical cases it is sufficient to just include the angular momentum since normally astrophysical massive sources are surrounded by plasmas. Matter accretes into the object and thereby very soon neutralize its charge by preferably accreting particles with the opposite charge. For the rest of this thesis (specially when I will talk about the ray-transfer in the vicinity of black holes) I consider the space-time to follow the Kerr equation.

The space-time around black holes have very interesting properties. The most intriguing features are the singularities that appear in the metrics. For example, in the case of Kerr space-time, the metric is singular at the  $\rho \equiv r = 0$  and also when  $\Delta = 0$ . The later singularities occur at

$$r_{\pm} = 1 \pm \sqrt{1 - a^2} \quad (1.2)$$

which are the so-called inner and outer horizons. These singularities are removable by changing the coordinate system. Properties of the black hole's horizons and their physical interpretations are studied in details and are still subject of intensive studies. The singularity at  $r = 0$  is critical for physics. It is the place where the rules of physics

(at least in the frame work of general relativity) break down. There are hopes (and already some proposals) that a quantized version of general relativity can describe the properties of these singularities.

Furthermore, the trajectories of particles in a Kerr space-time have also interesting features. In the simplest configuration, matter can move along free stable circular orbits with a rotational velocity (see e.g. Novikov & Thorne 1973)

$$\omega = \frac{d\varphi}{dt} = \frac{1}{r^{3/2} + a}. \quad (1.3)$$

in a Keplerian disc. The disc resides in the equatorial plane of the black hole. Individual components of the four-velocity of the Keplerian disk in the Boyer-Lindquist coordinates

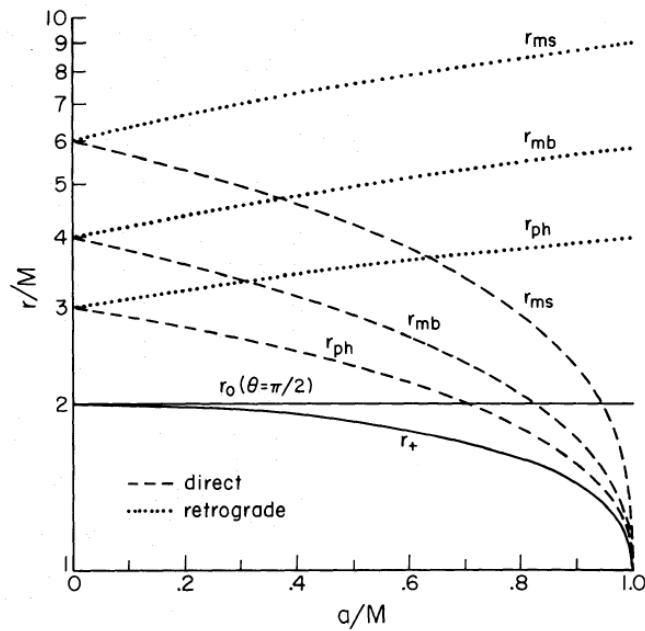


**Figure 1.1:** Specific radii in the equatorial plane of a Kerr black hole as a function of its spin. Dashed and dotted curves (for direct and retrograde orbits, respectively) show the marginally stable (*ms*), innermost bound (*mb*), and photon (*ph*) orbits. Solid curve indicates the event horizon ( $r_+$ ) and ergo-sphere ( $r_0$ ). (from: Bardeen 1972).

are

$$v^t = \frac{r^2 + a\sqrt{r}}{r\sqrt{r^2 - 3r + 2a\sqrt{r}}}, \quad (1.4)$$

$$v^r = 0, \quad (1.5)$$

$$v^\theta = 0, \quad (1.6)$$

$$v^\phi = \frac{1}{\sqrt{r(r^2 - 3r + 2a\sqrt{r})}}. \quad (1.7)$$

There is no free stable circular orbit below the marginally stable orbit (mso) defined by

$$r_{\text{ms}} = 3 + Z_2 - \sqrt{(3 - Z_1)(3 + Z_1 + 2Z_2)} \quad (1.8)$$

with  $Z_1 = 1 + (1 - a^2)^{1/3}[(1 + a)^{1/3} + (1 - a)^{1/3}]$  and  $Z_2 = \sqrt{3a^2 + Z_1^2}$ . Below this orbit the matter will experience a free fall down to the horizon. Thus the matter conserves both its specific energy and specific angular momentum. The actual accretion process into the black holes can be more complicated as it will be discussed in chapter 4.

There is another special radius that correspond to a Kerr metric which is called the *photon orbit*. This is the orbit of a test particle with infinite energy per unit rest mass (i.e. photon). The photon orbit is important for studying the so-called second images (see Luminet et al. 1979). In this case some photons may not travel directly to the observer, but orbit the black hole for one cycle and then reach the observer with a time delay. The minimum distance to a black hole where this can happen is the photon orbit. The second images of any event close to the black hole are much weaker than the original ones and happen to have time delays which scale with the mass of the black hole (see Luminet et al. 1979, Hollywood et al. 1995). Figure 1.1 shows some of the specific radii associated with a black hole as a function of its spin.

For a long time, black holes were considered as theoretical consequences from Einstein field equations. But this view started to change around late 1960s. At that time, the theoretical community was mostly convinced about the existence of black holes in nature. The first trials for finding observational evidence for the existence of such objects started in X-ray domain pioneered by observations of Riccardo Giacconi (Giacconi et al. 1962). The reason was that models for accreting black holes predicted very bright X-ray sources. The first candidate for a black hole detected in X-ray observations was Cyg X-1 (Bowyer et al. 1965).



**Figure 1.2:** Top: X-ray image of Cygnus X-1 (credit: NASA/CXC). Bottom: An artist illustration of material being gravitationally sucked off a blue super-giant variable star designated HDE 226868 onto a black hole known as Cygnus X-1 (credit: European Homepage for the NASA/ESA Hubble Space Telescope).

But finally, the first observational evidence of black holes came as a result of observing quasars in the radio frequency. The quasars are compact radio sources that are extremely bright. The amount of energy they release is so much that it can not be produced via nuclear fusion (see Fig. 1.2). On the other hand, people found that the release of gravitational bounding energy of matter accreting to a compact object can be so efficient that produce such extreme luminous sources (Schmidt 1963, Shakura & Sunyaev 1973).

These pioneer observations were followed by a large number of surveys which discovered a lot of extremely luminous sources, some of which are located at the center of the

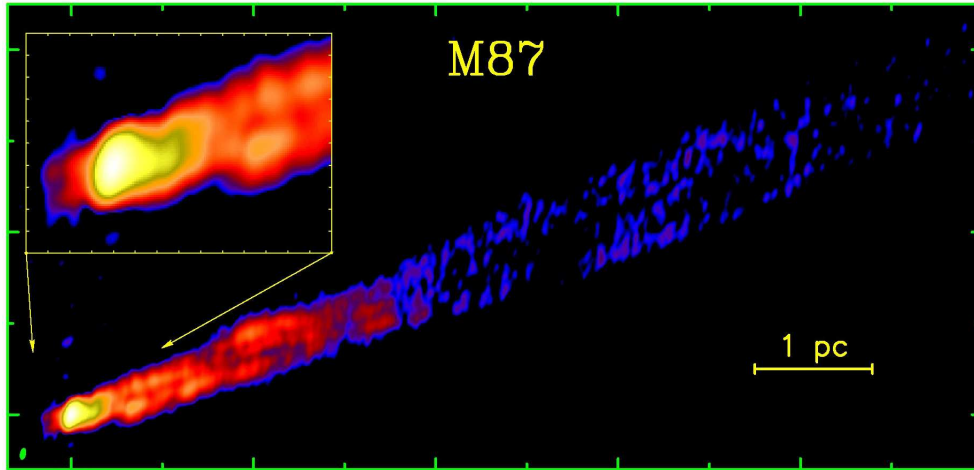


**Figure 1.3:** The Inner Jet of the Radio Galaxy M87 located in the Virgo cluster. The image shows a limb brightened jet and a faint counter-jet (credit: Y.Y. Kovalev, MPIfR Bonn).

galaxies (so called active galactic nuclei; AGN). Many AGNs emit jets of matter from a very compact source. The emission from these jets are mostly visible in the radio but some times even in the optical regime (see Fig. 1.3). The existence of such counterparts well resolved in the radio domain could be well described by a theory that relates their power with the strong gravity of black holes (Lynden-Bell & Sanitt 1969).

The other fact that supported the idea that super-massive black holes exist at the center of galaxies came from observations of the stellar and ionized gas dynamics at the core of some galaxies. These studies sped up after Hubble Space Telescope (HST) became active. Till nowadays it is a matter of very active field of research to look for black holes all over the mass spectrum (see Kormendy and Gebhart 2001, Ferrarese and Merritt 2000 and references therein).

However, the *solid* proof for the existence of black holes came from analyzing the orbits of stars in the center of our galaxy. Using very high resolution NIR observations, Eckart et al. 1997, Schödel et al. (2002) and Ghez et al. (2003) showed that the orbit of the stars at the GC can not be described but with the existence of a (super-)massive black hole with a mass of  $\sim 4 \times 10^6 M_{\odot}$  (for a recent estimation of the mass see Gillessen et al. 2009). This brings us to the subject of this thesis which studies the properties of this black hole at the center of the Milky Way. I will discuss this in more detail in the next sections.



**Figure 1.4:** Center of the Milky Way as observed in optical (top), NIR (second row), X-ray (third row) and composite image of altogether (bottom). Penetrating through the obscuring dust, NIR and X-ray reveal the intense activity near the galactic core. The center of the galaxy is located within the bright white region to the right of and just below the middle of the images. (from: website of Chandra X-ray observatory. Credit: X-ray: NASA/CXC/UMass/D. Wang et al.; Optical: NASA/ESA/STScI/D. Wang et al.; IR: NASA/JPL-Caltech/SSC/S. Stolovy.)

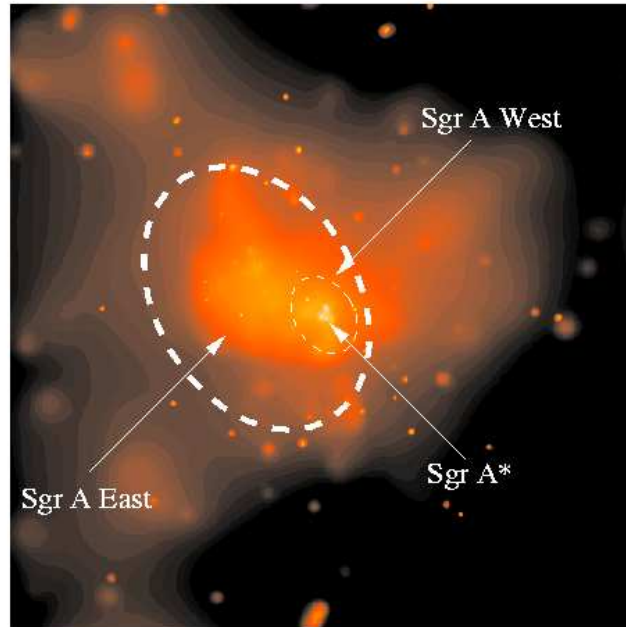


*Figure 1.5:* Smoothed X-ray intensity observed by Chandra in the 1.5-3.0 keV band from the inner  $\sim 20\text{pc} \times 20\text{pc}$  of the galaxy. (from: Maeda et al. 2002)

## 1.2 The Galactic Black Hole

The Galactic Center region at the heart of our galaxy was hidden for a long time behind the obscuring dust and gas in the line of sight from the Earth. However, the development of observational methods on a wide range of frequencies made it possible to observe this region with a very high angular resolution. These observations revealed many structures and dynamic objects which make this place one of the most interesting observing targets in our galaxy (see Fig. 1.4).

One of the most compelling objects of this region is located at its core: the massive dark mass that is the best candidate for super-massive black hole known up to now. The existence of such an object was longly anticipated by theoreticians. In fact, in

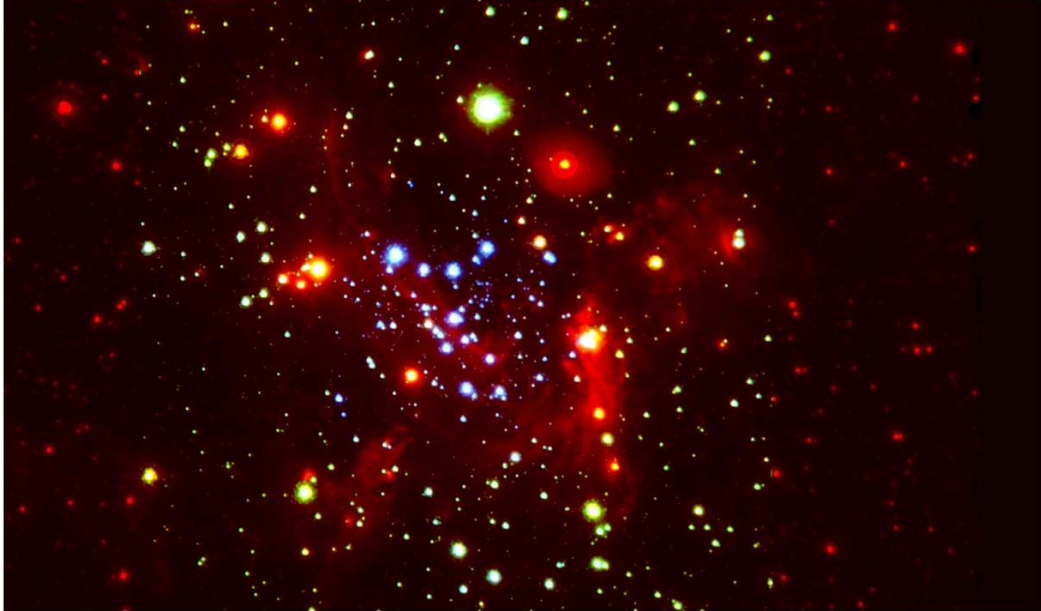


**Figure 1.6:** *H, K and L' band (1.3, 2.2 and 4.1  $\mu\text{m}$ ) composite image of the Galactic Center as it observed by NACO/VLT (credit: G. Witzel and A. Stolte, University of Cologne)*

1971 Lynden-Bell and Rees proposed that a black hole may exist in the center of our galaxy. The first observational indications for the existence of such a mass came from the early days of radio interferometry. In February 1974, Balick and Brown detected a very sharp radio source with the 14-meter radio telescope at Huntersville (NRAO). Since this source stands out in the radio maps as a bright point and the GC region is located close to the constellation Sagittarius, they named it Sagittarius A\* (or shortly Sgr A\*). The ionized gas around this bright point source show a coherent flow with a systematic motion. It is difficult to identify the kinematics of this ionized gas since we do not have a complete knowledge of its 3-dimensional geometry. Yusef-Zadeh et al. (1998) showed that the prominent motion of the gas projected in the plane of our sky is from east to west with a speed of  $\sim 100$  km/s. Assuming a Keplerian rotation around the center, this velocity at a distance of roughly three light years corresponds to a dark mass of  $\sim 3.5 \times 10^6 M_{\odot}$  concentrated in this radius.

After the launch of the Chandra X-ray observatory, a better spatial resolution X-ray imaging of the GC region became possible. This high resolution allowed for the separation of around 1000 discrete sources from the diffuse X-ray background emission in this region. At the very center, exactly at the place which coincides with the position

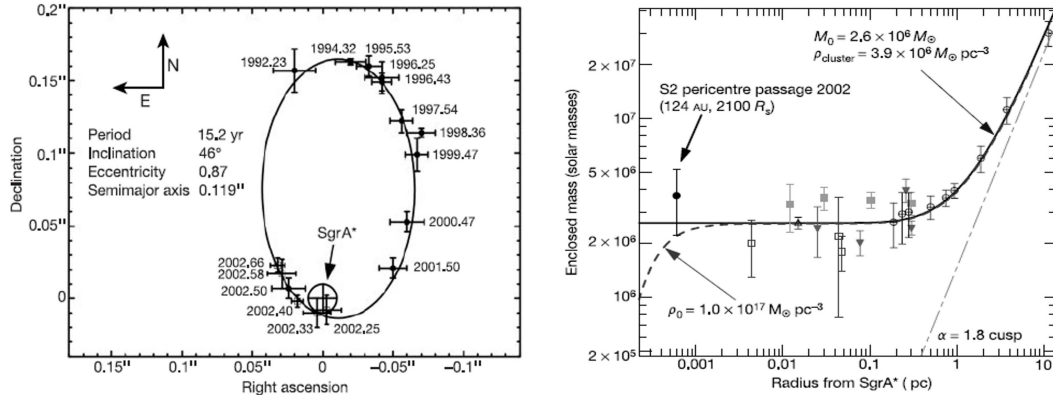


**Figure 1.7:** Left: Astrometric positions and orbital fits of the star S2 for the observations between 1992 to 2002. Right: Enclosed mass in solar mass units as a function of radius from Sgr A\* derived from the observations in the same epoch of time (images from Schödel et al. 2002).

of the radio point source Sgr A\*, Chandra can resolve a bright cloud. The limited resolution of this device does not allow for a complete separation of Sgr A\* from the other features that surround the source like Sagittarius A East (see Fig. 1.5). Sagittarius A East is a non-thermal radio source with a shell-like morphology which is probably the consequence of a supernova explosion morphology located at the Galactic Center.

The new generation of 8-10 meter ground based telescopes which can achieve unprecedented high angular resolution in near infra-red band, opened a new window for observations in the galactic center. These new telescopes like VLT, Keck or SUBARU can achieve spatial resolutions as good as  $\sim 40$  mas (see Fig. 1.6). Pioneer observations using the NIR adaptive optics (Eckart et al. 1997, Genzel 1997, Schödel et al. 2002, Ghez et al. 2003) were focused on constraining the central dark mass at the GC using the orbits of the stars in the central nuclear star cluster (also called S-cluster). Specially the stars that pass the position of Sgr A\* by distances of only of the order of light days. Eckart et al. (1997) and Genzel et al. (1997) were the first who published the enclosed mass as a function of the distance from Sgr A\*. Using the star S2 which orbits the central dark mass with a period as short as  $\sim 15$  years, they were able to constrain its mass to  $\sim 3.7 \pm 1.5 \times 10^6 M_\odot$  (Schödel et al. 2002) or  $4.0 \pm 0.6 \times 10^6 M_\odot$  (Ghez et al. 2003). They showed that the orbit can be best described by a point source with the mentioned mass at the position of Sgr A\*, including the effect of the mass of the visible stars inside the cluster (Fig. 1.7). Gillessen et al. (2009) recently published an update of this study while the star S2 completed one orbit between 1992-2008 (see Fig. 1.8 and Gillessen et al. 2009).

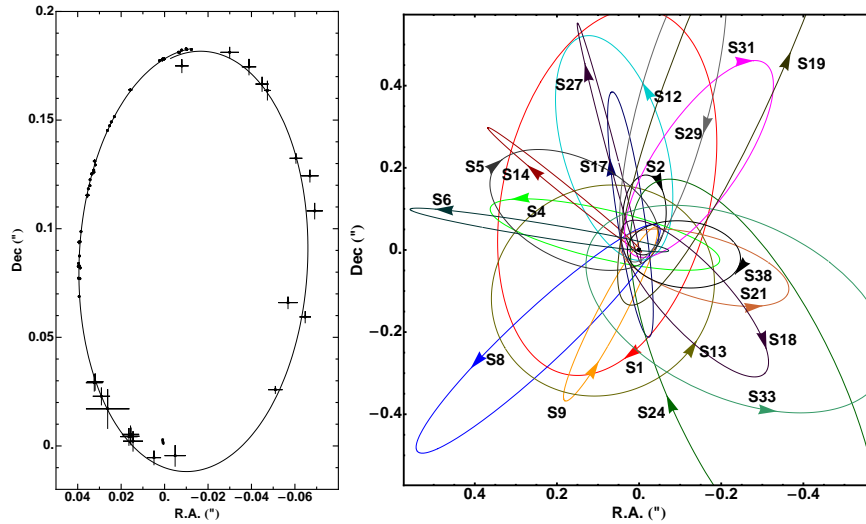


**Figure 1.8:** *Left: Astrometric positions and orbital fit of the star S2 for the observations between 1992 to 2008. Right: Stellar orbits at the nuclear star cluster around Sgr A\* (images from Gillessen et al. 2009).*

Sagittarius A\* by itself is a highly variable source in the entire range of the electromagnetic spectrum that can be resolved up to now. This provides a unique opportunity to study the physical processes happening in the environment very close to the black hole. In the radio regime it is bright enough in the sky to be constantly observed. The only problem is that in order to achieve high angular resolution one has to increase the integration time which make time resolved high spatial resolution observations of this source very difficult. On the other hand, in the NIR and X-ray bands the integration times of the orders of minutes could be achieved, but the confusion from the background (unresolved stars very close to the black hole in NIR band and the diffuse background emission of the hot gas around in X-ray) is so high that the source is (probably) only visible when it is in its so called flaring state (for a detailed discussion see Sabha et al. 2010).

By the astrophysical standards, Sgr A\* is one of the faintest black holes known yet. Its luminosity lies about nine orders of magnitude below its corresponding Eddington luminosity. This is a very surprising fact since wind from young stars in the vicinity of the black hole provide enough material that if all be accreted into the black hole it must be orders of magnitude more luminous. However, the inferred accretion rate within several Schwarzschild radii is 2 orders of magnitude lower (Marrone 2008) than the inferred Bondi accretion rate (Bondi 1952) at several arcseconds. This surprising low luminosity of Sgr A\* motivated a lot of theoretical efforts to explain it, varying

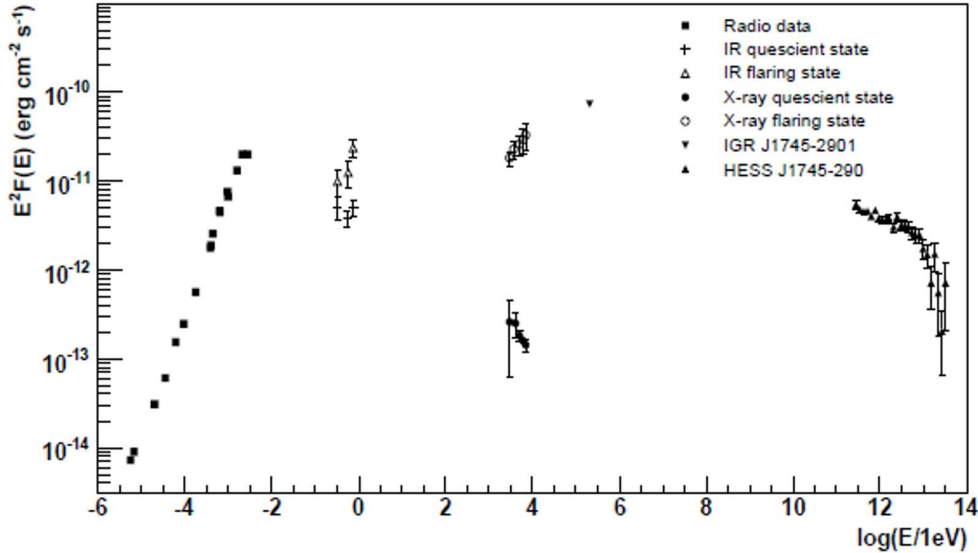


**Figure 1.9:** A composite spectral energy distribution of the Sgr A\* and its possible high-energy counterparts IGR J1745-2901 and HESS J1745-290. The radio data are from Zylka et al. (1995) and Falcke et al. (1998). The IR data are from Hornstein et al. (2002) and Ghez et al. (2004). Chandra data points come from Baganoff et al. (2001 and 2003), IGR J1745-2901 points from Belanger et al. (2006). The HESS J1745-290 spectral points are shown by filled triangles (image from Aharonian et al. 2009).

from Advection Dominated Accretion Flow (ADAF) models to the collimated outflow models (Markof et al. 2001). Recently Broderick et al. (2009) showed that the observed overall spectral energy distribution (SED) of Sgr A\* (Fig. 1.9) indicates that the source has a horizon. They claimed that the SED of Sgr A\* can only be explained by a source without a solid surface (e.g. a neutron star, see Broderick et al. 2009).

As I mentioned, the emission coming from Sgr A\* is highly variable in all the wavelengths it has been observed to date. In fact it is not clear if the source has a quiescent level (as it appears in NIR and X-ray observations) since the sensitivity of the observing devices are limited (see Fig. 1.10). Variability profiles of the emission from astrophysical sources, specifically black holes, can reveal useful information about the intrinsic properties of the source. This work is dedicated to the detection and modeling of these

variabilities of Sagittarius A\* (with the focus on NIR band), as I will discuss in the next chapters in detail.

### 1.3 This Thesis

Recent NIR and X-ray observations have revealed the non-thermal nature of high frequency radiation from Sgr A\* (Eckart et al. 2006a-c, 2008a-c; Gillessen et al. 2006; Hornstein et al. 2007). Sgr A\* is probably visible in the NIR regime only during its flaring state. The short time scale variabilities seen during several observed NIR and X-ray flares argue for an emitting region not bigger than about 10 Schwarzschild radii ( $r_s = \frac{2GM}{c^2} = 2r_g = 1.2 \times 10^{12} \left(\frac{M}{4 \times 10^6 M_\odot}\right)$  cm) of the associated super-massive black hole (Baganoff et al. 2001; Genzel et al. 2003). We have scaled the relevant physical distances according to the gravitational radius ( $r_g$ ) throughout this thesis. The NIR flares are highly polarized and normally have X-ray counterparts, which strongly suggests a synchrotron-self-Compton (SSC) or inverse Compton emission as the responsible radiation mechanisms (see chapter 2 and Eckart et al. 2004, 2006a,b; Yuan et al. 2004; Liu et al. 2006). Several observations have already confirmed the existence of a time lag between the simultaneous NIR/X-ray flares and the flares in the lower frequencies. This is interpreted as a sign for cooling down via adiabatic expansion (Eckart et al. 2006a, 2008b,c; Yusef-Zadeh et al. 2006a,b, 2007, 2008; Marrone et al. 2008, Zamaninasab et al. 2008a, Sabha et al. 2010).

The other feature related to these NIR/X-ray flares is the claimed quasi-periodic oscillations (QPOs) with a period of  $20 \pm 5$  minutes, which have been reported in several of these events (Genzel et al. 2003; Belanger et al. 2006; Eckart et al. 2006b,c; 2008a; Meyer et al. 2006a,b, Hamaus et al. 2009). Short periods of increased radiation (the so called "NIR flares", normally around 100 minutes) seem to be accompanied by QPOs. All the studies mentioned above probed this  $20 \pm 5$  minutes quasi-periodicity, by doing sliding window analysis with window lengths of the order of the flaring time. Recently, Do et al. (2009) argued that they did not find any significant periodicity at any time scale while probing their sample of observations for a periodic signal. Their method is based on the Lomb-Scargle periodogram analysis of a sample of six light curves and comparing them with several thousands of artificial light curves with the same underlying red-noise. One must note that the suggested QPOs are transient phenomena, lasting for only very few cycles (50-100 minutes). This kind of behavior, along with the inevitable uncertainty in the red noise power law index determination, makes a clear and unambiguous detection ( $> 5\sigma$ ) of a periodic signal very difficult. Whenever a flare of Sgr A\* was observed with polarimetry, it was found that it is

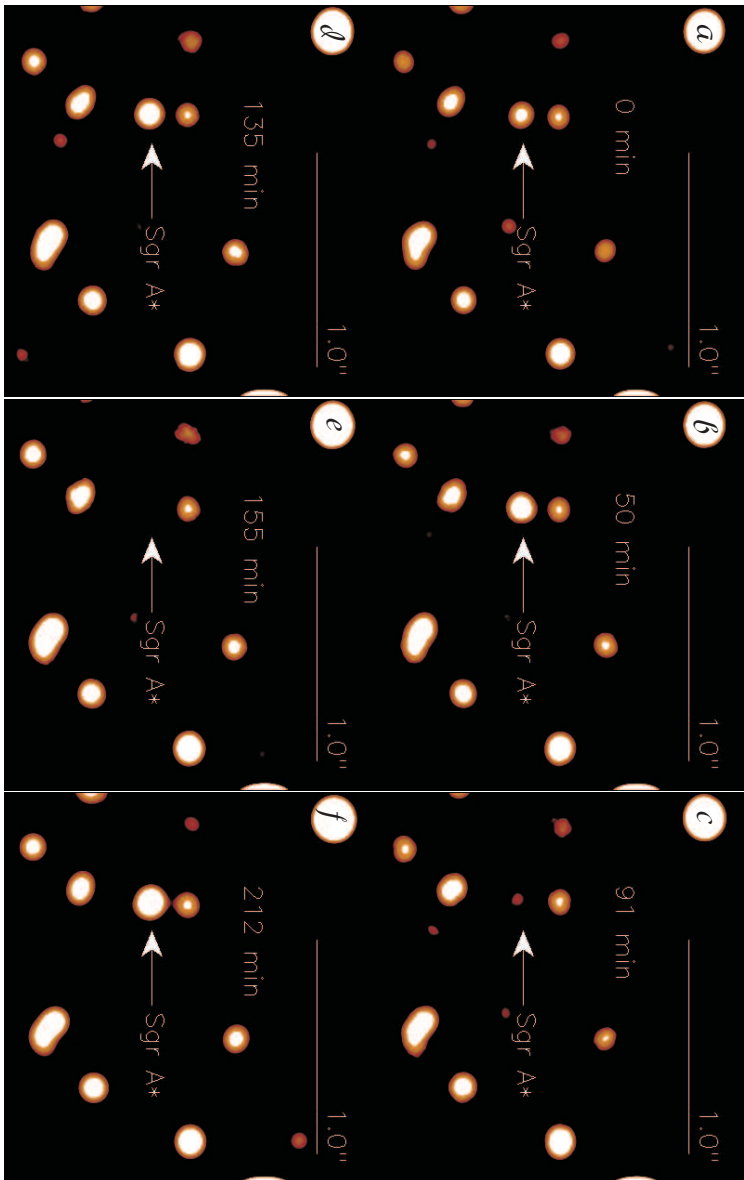


**Figure 1.10:** *Sgr A\** as it was observed in NIR I'-band ( $3.8 \mu\text{m}$ ) on 3 June 2008 between 05:29:00 - 09:42:00 (UT time). (a-f) show the observed images of *Sgr A\** after 0, 50, 91, 135, 155 and 212 minutes off the start of observation. The images show that when *Sgr A\** is in its flaring state the flux changes up to 100% in time intervals only of the order of tens of minutes.

accompanied by significant polarization that varies on similarly short time-scales as the light curve itself. By carrying out analysis only on the total flux, some pieces of the observed information are ignored. It is already known that polarimetric data have been shown to be able to reveal substructure in flares, even when the light curve appears largely featureless (e.g. see Fig. 4 in Eckart et al. 2006b). The other main advantage of polarimetric observations is that, in addition to the flux density light curve, one can analyze the changes in the observed degree of polarization and also the changes in polarization angle during flaring times.

The claimed quasi-periodicity has been interpreted as being related to the orbital time scale of matter in the inner parts of the accretion disk. According to well known observed high frequency quasi-periodic oscillations (HFQPOs) in X-ray light curves of stellar mass black holes and binaries (Nowak & Lehr 1998), this interpretation is of special interest since it shows a way to better understand the behavior of accretion disks for a wide range of black hole masses. The recent unambiguous discovery of  $\sim 1$  hour (quasi-)periodicity in the X-ray emission light curve of active galaxy RE J1034+396 provides further support to this idea, and extends the similarity between stellar-mass and super-massive black holes to a new territory (Gierliński et al. 2008).

Although the origin of the observed QPOs in the sources associated with black holes is still a matter of debate, several magnetohydrodynamics (MHD) simulations confirmed that it could be related to instabilities in the inner parts of the accretion disks, very close to the marginally stable orbit of the black hole ( $r_{ms}$ ), and also possibly connected with the so called "stress edge" (Hawley 1991; Chan et al. 2009b). If the flux modulations are related to a single azimuthal compact over-dense region (hereafter: "hot spot"), orbiting with the same speed as the underlying accretion disk, one can constrain the spin of the black hole by connecting the observed time scales of QPOs to the orbital time scale of matter around the black hole:  $T = 2.07(r^{\frac{3}{2}} + a)(\frac{M}{4 \times 10^6 M_{\odot}})$  min (Bardeen et al. 1972, where  $-1 \leq a \leq 1$  is the black hole dimensionless spin parameter and  $r$  is the distance of the spot from the black hole). The characteristic behavior of general relativistic flux modulations produced via the orbiting hot spots have been discussed in several papers (see e.g. Cunningham & Bardeen 1973; Abramowicz et al. 1991; Karas & Bao 1992; Hollywood et al. 1995; Dovčiak 2004, 2007). In this thesis, I have used a spotted accretion disk scenario to model the observed modulations of our sample of NIR light curves.

Several authors have proposed different models in order to explain the flaring activity of Sgr A\*. These models cover a wide range of hypotheses like disk-star interactions (Nayakshin et al. 2004), stochastic acceleration of electrons in the inner region of the disk (Liu et al. 2006), sudden changes in the accretion rate of the black hole (Liu et al. 2002), heating of electrons close to the core of a jet (Markoff et al. 2001; Yuan et

al. 2002), trapped oscillatory modes in the inner regions of the accretion disk in the form of spiral patterns or Rossby waves (Tagger & Melia 2006; Falanga et al. 2007; Karas et al. 2008), non-axisymmetric density perturbations which emerge as the disk evolves in time (Chan et al. 2009b), non-Keplerian orbiting spots falling inward inside the plunging region created via magnetic reconnection (Falanga et al. 2008), and also comet like objects trapped and tidally disrupted by the black hole (Čadež et al. 2006; Kostić et al. 2009).

Observational data render some of these models unlikely. For instance, the star-disk interaction model is unable to produce the repeated flux modulations and also the high degree of polarization, since it mainly deals with thermal emission. The tidal disruption of comet like objects are also unable to reproduce the observed rate of flares per day, since the estimated capture rate of such objects for Sgr A\* environment is at least one order of magnitude lower (Čadež et al. 2006). Nevertheless, several viable models exist and make different predictions that can be distinguished observationally. For example, one important characteristic prediction of hot spot models is about the wobbling of the center of the images (Broderick & Loeb 2006a,b; Paumard et al. 2006; Zamaninasab et al. 2008b; Hamaus et al. 2009). Significant efforts have been already devoted to measure this possible position wander of Sgr A\* in the mm, sub-mm and NIR regimes (Eisenhauer et al. 2005b, 2008, Gillessen et al. 2006, Reid et al. 2008, Doelleman et al. 2008). In this thesis I discuss how NIR polarimetry and the next generations of VLT interferometry (VLTI) and Very Long Baseline Interferometry (VLBI) experiments can provide data to support or reject certain models for the accretion flow/outflow related to Sgr A\*. Obtaining accurate data on the accretion flow of Sgr A\* can lead us to a better understanding of the physics of strong gravitational regimes, formation of black holes and their possible relation to the galaxy formation process in a cosmological context.

In chapter 2 I present a sample of NIR light curves observed in the polarimetry mode. A brief description about the details of observation and data reduction methods is provided also. I discuss the quasi-periodicity detection methods and present the results of a correlation analysis between the flux and polarimetric parameters in chapter 3. A general description of my model set-up and results of simulations are discussed in chapter 4. There I also show how NIR polarimetry can be used as a way to constrain physical parameters of the emitting region (like its geometrical shape). In chapter 5 I mainly discuss the predictions that the future NIR interferometer (GRAVITY) is expected to reveal and how different assumptions in the model parameters can modify the results. A straightforward method for testing the properties of the Sgr A\* based on the time resolved NIR polarimetry is discussed in chapter 6. In chapter 7 I summarize the main results of the thesis, and draw some conclusions.

## Chapter 2

# Observations and Data Reduction

*The small or large rock will fall to the Earth along the path of a line that is perpendicular to the plane of the horizon; this is witnessed by experience. And this perpendicular is away from the tangent point of the Earth's sphere and the plane of the perceived horizon. This point moves with the motion of the Earth and thus there will be no difference in place of fall of the two rocks.*

-A. A. Birjandi ( - 1528 AD)  
Physicist, astronomer and mathematician.

All NIR observations I will refer in the next chapters of this thesis have been carried out in the NIR  $K_s$  band with the NIR camera CONICA and the adaptive optics (AO) module NAOS (NACO) at the ESO VLT unit telescope 4 (YEPUN) on Paranal, Chile<sup>1</sup> and with the CIAO NIR camera on the Subaru telescope<sup>2</sup> (see Fig. 2.1). Here I will discuss very briefly some facts about these facilities, our observing runs and also the methods that have been used for reducing the data.

---

<sup>1</sup>Based on observations at the Very Large Telescope (VLT) of the European Southern Observatory (ESO) on Paranal in Chile; Programs:075.B-0093 and 271.B-5019(A).

<sup>2</sup>Based on data collected at Subaru Telescope, which is operated by the National Astronomical Observatory of Japan.

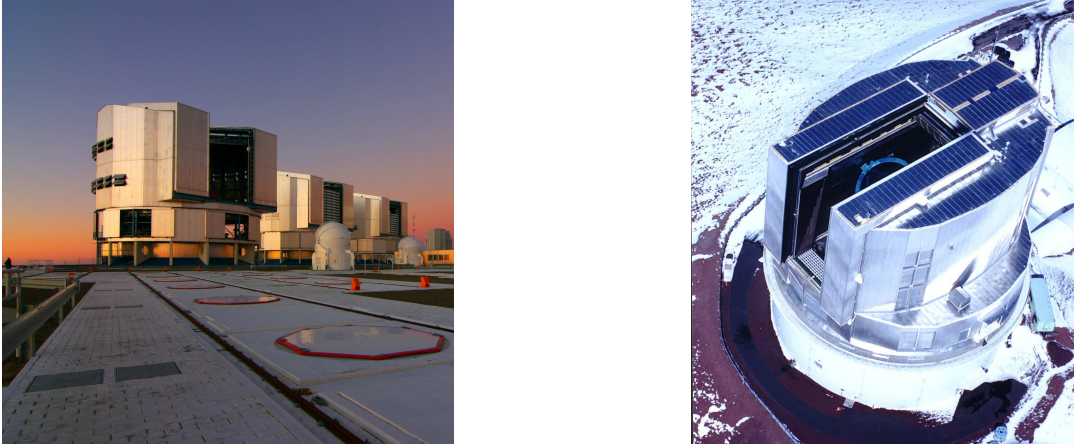


**Figure 2.1:** *Left: Very Large Telescope (VLT) 8 meter telescope of the European Southern Observatory (ESO) on Paranal in Chile (credit: MPIfR, Gerd Weigelt). Right: Subaru 8.2-m telescope of the National Astronomical Observatory of Japan located at Mauna Kea, Hawaii (credit: National Astronomical Observatory of Japan).*

## 2.1 NIR Polarimetry of Sagittarius A\*

Both VLT and Subaru NIR facilities are suited for time resolved observations of total intensity and polarimetric degree and angle as well with a sampling of about 2 to 3 minutes. The NAOS/CONICA NIR camera installed on UT4, VLT allows for simultaneous measurement of two orthogonal directions of electric field vector via a Wollaston prism. The combination with a rotary half-wave plate allows to alternate rapidly between measurements of different angles of the electric vector. This is crucial for determining the linear polarization characteristics of a time varying source. The CIAO camera uses a rotating half-wave plate combined with a fixed wire grid polarizer for measuring the linear polarization.

Since the first NIR polarimetric observation of Sgr A\* in 2004 (Eckart et al. 2006a), several polarized flares have been observed (Meyer et al. 2006 a,b, 2007; Eckart et al. 2008a, Nishiyama 2009). For the VLT observations (see Table. 2.1), the infrared wave-front sensor of NAOS was used to lock the AO loop on the NIR bright (K-band magnitude  $\sim 6.5$ ) super-giant IRS 7, located about  $5.6''$  north of Sgr A\*. Atmospheric conditions (and consequently the AO correction) were stable enough during the observations for doing high angular resolution photometry and polarimetry (typical coherence time of 2 milliseconds and larger). The exposures have been dithered. All exposures were sky subtracted, flat-fielded, and corrected for dead or bad pixels. As the most im-

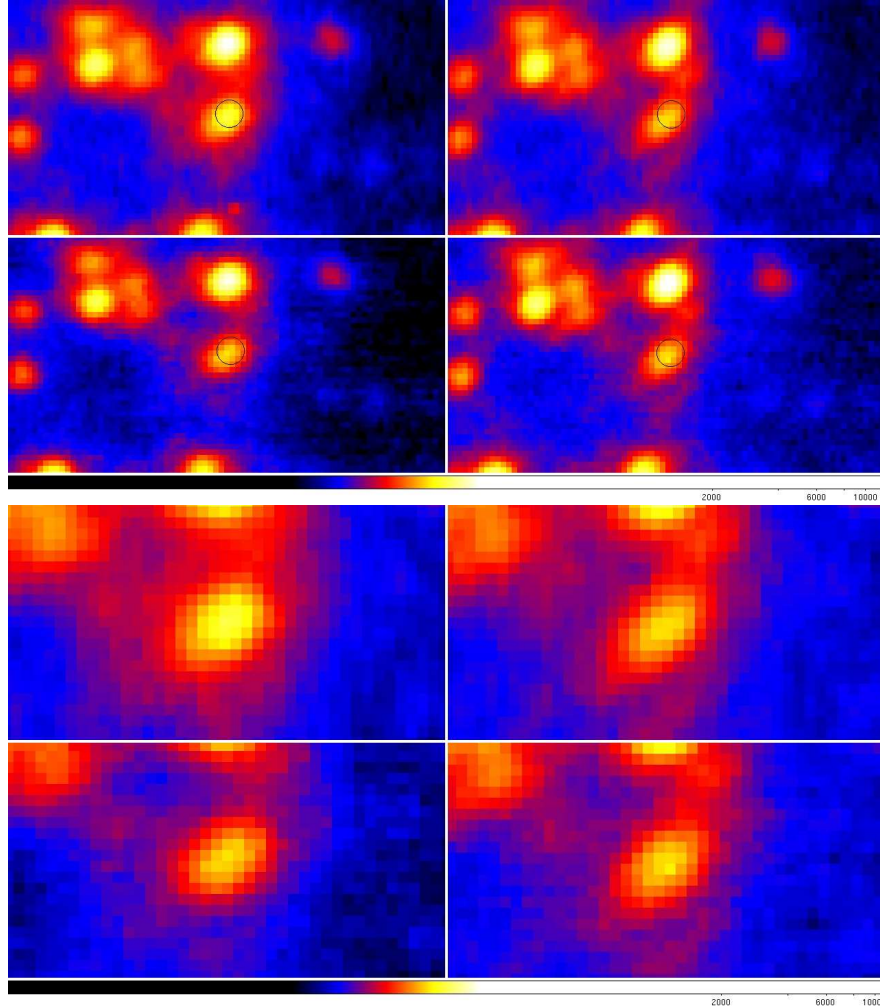


**Figure 2.2:** *Top: Central  $0.6'' \times 0.4''$  region of the GC in  $2.2\mu\text{m}$  for four orthogonal polarization channels:  $0^\circ$  (top left),  $90^\circ$  (top right),  $45^\circ$  (bottom left) and  $135^\circ$  (bottom right). The circles indicate the position of Sgr A\* in each image. The star S17, was very close to Sgr A\* at the time of observation (15 May 2007). Bottom: Zoom in view to the position of Sgr A\*. The intensity scale for all the images are logarithmic.*

portant improvement of this reduction the dithered exposures have been aligned with sub-pixel accuracy by a cross-correlation method (Devillard 1999). Point Spread Functions (PSFs) were extracted from these images with StarFinder (Diolaiti et al. 2000). The images were deconvolved with the Lucy-Richardson (LR) algorithm. Beam restoration was carried out with a Gaussian beam of FWHM corresponding to the respective

wavelength. The final resolution at  $2.2\mu\text{m}$  is about 60 milli-arcseconds (mas). Flux densities of the sources were measured by aperture photometry. Because of the high accuracy of the image alignment it was possible to separate Sgr A\* from nearby star (S17), by choosing a circular aperture of about 52 mas radius (see Fig. 15 of Eckart et al. 2006a and discussion therein). This results in a better correction for the flux contribution of these stars. The data was corrected for extinction using  $A_K = 2.8$  (Eisenhauer et al. 2005a, Schödel et al. 2007). The relative flux density calibration was carried out using known K-band flux densities and positions of 14 sources in the IRS16 cluster. This results in a K-band flux of the high velocity star S2 of  $22 \pm 1$  mJy, which compares well with magnitudes and fluxes for S2 quoted by Ghez et al. (2005b) and Genzel et al. (2003). The measurement uncertainties for Sgr A\* were obtained from the reference star S2. Figure 2.2 shows the observed images of Sgr A\* and its surroundings in four orthogonal polarimetric channels. We have used the nomenclature of the Stokes parameters for the polarization studies. For the VLT observations they are defined as:

$$I = \frac{I_{0^\circ} + I_{45^\circ} + I_{90^\circ} + I_{135^\circ}}{2} \quad (2.1)$$

$$Q = I_{0^\circ} - I_{90^\circ} \quad (2.2)$$

$$U = I_{45^\circ} - I_{135^\circ} \quad (2.3)$$

With the current NACO/VLT instrumental setup it is only possible to measure the linear polarization (i.e.  $V = 0$ ).

The data from the CIAO camera were reduced by Shogo Nishiyama (Nishiyama et al. 2009, see also Table 2.1). The observation was carried out on 28 May 2008 while the stable atmospheric condition during the observations provided a stable correction with seeing values between  $0.17''$  and  $0.21''$  in the  $K_s$  band. The source was observed in the  $0^\circ$ ,  $45^\circ$ ,  $90^\circ$  and  $135^\circ$  channels with exposure times of  $\sim 80$  seconds. A standard data reduction is performed using IRAF<sup>3</sup> and StarFinder (dark and flat fielding corrections, sky background estimation and bad pixel corrections). The same factor for the extinction correction in the VLT data analysis has been used here ( $A_K = 2.8$ ). Figure 2.3 shows the deconvolved images of the GC region while a clear flare is observable at the position of Sgr A\*.

For all the observations the degree of linear polarization ( $\Pi_L$ ) and the angle of polarization ( $\chi$ ) are defined by the following equations:

<sup>3</sup>The software *IRAF* (Image Reduction and Analysis Facility) is distributed by the *National Optical Astronomy Observatories (NOAO)* and operated by the *Association of Universities for Research in Astronomy (AURA)*.

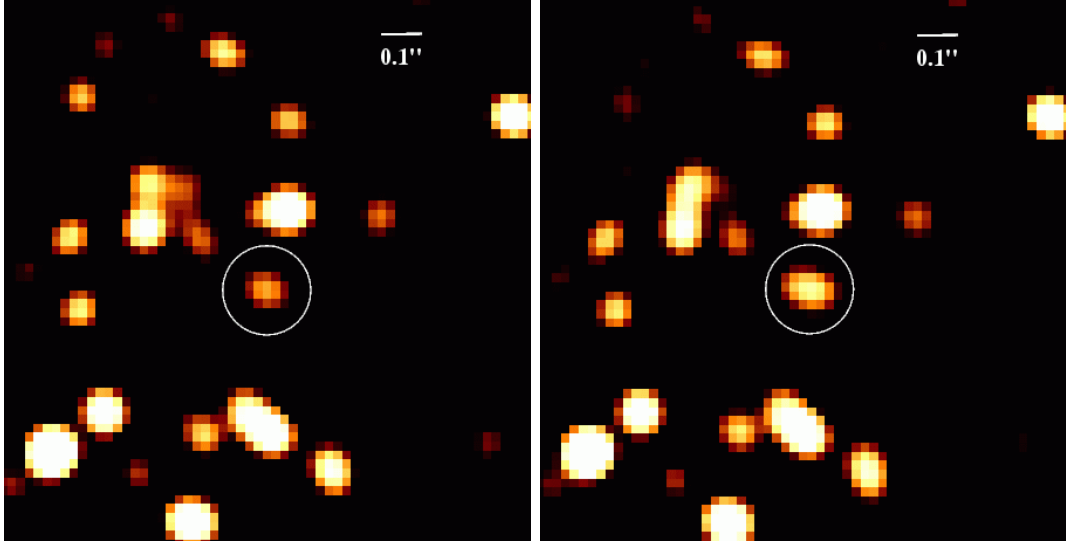


**Figure 2.3:** Central  $1.3'' \times 1.3''$  region of the GC observed in the  $K_s$  band. The time from the beginning of the observation is 145.1 (left) and 158.4 min (right). In each image, the location of Sgr A\* is marked by a circle, and a faint star (S17) is also located in the circle. The image scale is logarithmic, and the integration time is  $20 \times 4$  sec. The images were sky-subtracted, flat fielded, corrected for bad pixels and cosmic rays, and deconvolved with the Lucy-Richardson algorithm (images from Nishiyama et al. 2009).

$$\Pi_L = \frac{\sqrt{Q^2 + U^2}}{I} \quad (2.4)$$

$$\chi = \frac{1}{2} \arctan \left( \frac{U}{Q} \right) \quad (2.5)$$

Figure 2.4 shows the resultant light curves of the flux and polarization angle and degree. This sample includes all the NIR polarimetry observations that has been carried out for Sgr A\*. For more details about the observations and the data reduction procedures see (Witzel 2008, Nishiyama et al. 2009, Eckart et al. 2006a, 2008a, Meyer et al. 2007a,b).

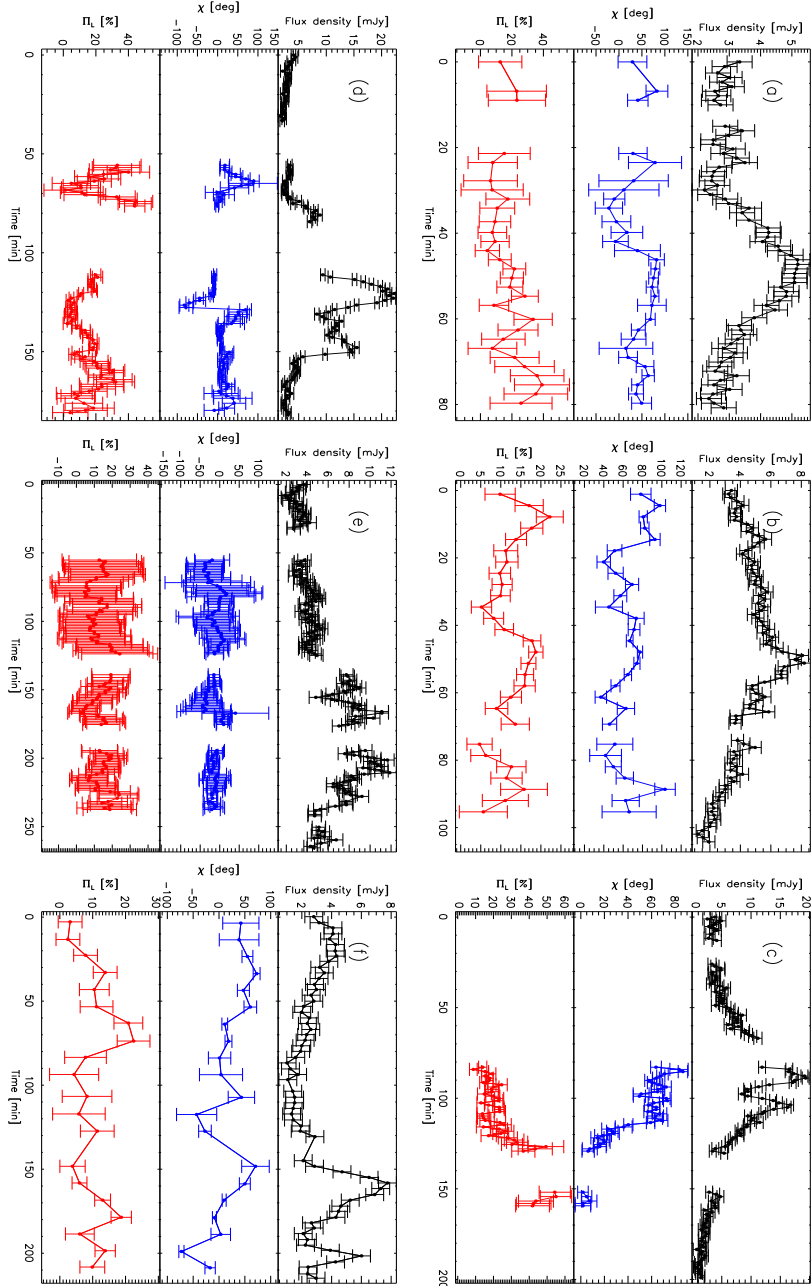


**Figure 2.4:** Our sample of light curves of Sgr A\* flares observed in NIR  $K_s$  band ( $2.2\mu\text{m}$ ) polarimetry mode. The events were observed on 13 June 2004 (a), 30 July 2005 (b), 1 June 2006 (c), 15 May 2007 (d), 17 May 2007 (e) and 28 May 2008 (f). In each panel, top shows the de-reddened flux density measured in mJy (black), the middle shows the polarization angle (blue) and the bottom shows the degree of linear polarization (red). The gaps in the light curves are due to the sky background measurements.

Date (Telescope)	Spectral domain	UT start time	UT stop time	Max. flux	Min. flux	Ave. flux sampling	Ave. pol. sampling
13 June 2004 (NACO)	2.2 $\mu$ m	07:20:02	09:15:08	5.19 mJy	2.21 mJy	1.2 min	3 min
30 July 2005 (NACO)	2.2 $\mu$ m	02:07:36	07:03:39	8.19 mJy	1.23 mJy	1.2 min	3 min
1 June 2006 (NACO)	2.2 $\mu$ m	04:26:03	10:44:27	19.33 mJy	0.72 mJy	1.5 min	2 min
15 May 2007 (NACO)	2.2 $\mu$ m	09:08:14	09:42:12	22.27 mJy	1.70 mJy	1.5 min	2 min
17 May 2007 (NACO)	2.2 $\mu$ m	04:42:14	09:34:40	11.87 mJy	1.86 mJy	1.5 min	2 min
28 May 2008 (CIAO)	2.15 $\mu$ m	09:22:51	13:00:37	7.70 mJy	0.97 mJy	3.3 min	10 min

*Table 2.1: Observations log.*



## Chapter 3

# Data Analysis

$$\begin{aligned}\sin(a + b) &= \sin(a) \cos(b) + \cos(a) \sin(b) \\ \cos(2a) &= 1 - 2 \sin^2(a) \\ \sin(2a) &= 2 \sin(a) \cos(a)\end{aligned}$$

-A. W. Buzjani (940 AD - 998 AD)  
Mathematician and astronomer.

### 3.1 Timing Analysis

In Chapters 1 and 2 I described briefly the observed features in NIR light curves of Sgr A\*. Theorists have long anticipated that a cyclic (or quasi-cyclic) modulation in Sagittarius A\* light curves ought to be detectable. This chapter describes how to look for such a periodic signal. The optimal method of extracting the signal is to use different approaches as I will demonstrate in the next sections.

#### 3.1.1 Tools of Time-Series Analysis

The convention normally used for the auto-correlation of a signal  $X(t)$  is

$$AC(\tau) = \langle [X(t)X(t + \tau)] \rangle \quad (3.1)$$

but as we saw in the previous chapter, our sample of light curves is unevenly sampled and normally have large gaps in between because of the sky background observations. One way to use the normal nomenclature for such a time series is by interpolating and re-binning, the data but it is not clear how such operations will change the result of the analysis. To reduce any artificial effects caused by these mentioned facts, I have used the convention invented by Tal Alexander (1997). This method is basically a modified version of the discrete correlation function (DCF) algorithm (Edleson & Krolik 1988), in which all points from the two light curves are ordered according to their time difference,  $\tau_{ij}$ , and binned according to the user's discretion. The cross-correlation function (CCF) of each bin is then estimated by

$$r_{dcf}(\tau) = \frac{1}{n} \sum_{r_{ij}bin} \frac{(x_i - \bar{x})(y_i - \bar{y})}{f_x f_y} = \frac{1}{n} \sum_{r_{ij}bin} u_{ij} \quad (3.2)$$

and the error is estimated by the scatter of  $u_{ij}$  terms ( $\bar{x}, \bar{y}, f_x^2$  and  $s_y^2$  are the sample means and variances). The drawback of this method is that the DCF suffers from the same problems as the closely related linear correlation coefficient  $r$ , which measures the correlation between independently drawn pairs  $(x, y)$ . The sample distribution of  $r$  is known to be very skewed and far from normal. Fisher's z-transform of  $r$  (Fisher 1920) is approximately normally distributed when  $(x, y)$  are drawn from a binormal distribution, and can therefore be used to estimate the confidence level of a measured correlation. Because the points in the light curve are not normally distributed and are auto-correlated, it is not immediately obvious that the z-transform is generally applicable for normalizing the DCF. The z-transformed discrete correlation function (ZDCF) approximates the bin's distribution by a bi-normal distribution for which the Fisher's z-transform

$$z = \frac{1}{2} \log \left( \frac{1+r}{1-r} \right), \quad r = \tanh(z) \quad (3.3)$$

is roughly normally distributed with a known mean,  $\bar{z}(\rho)$ , and variance  $f_z^2(\rho)$ . These are estimated by  $\bar{z}(r)$  and  $f_z^2(r)$ . The bin's ZDCF estimate is then

$$r_{zdcf}(\tau) = r_{-(r - \tanh(\bar{z} - f_z))}^{+(\tanh(\bar{z} + f_z) - r)} \quad (3.4)$$

The binning is then defined by equal population rather than equal  $\Delta\tau$ . The z-transform's convergence requires a minimum of  $n_{min} = 11$  points per bin. It has been shown that this method is statistically robust even when applied to very sparsely and irregularly sampled light curves (Alexander 1997).

Another common tool for searching for periodicities are periodograms. Nomenclature in power spectral analysis is often not well-determined and confusing. Here I use

the convention of Priestley (1989). The periodogram is the squared modulus of  $f(\nu)$ , the Fourier transform of the data:

$$Per(\nu) = |f(\nu)|^2 \quad (3.5)$$

For a discrete Fourier transform of a light curve of length  $T$  with  $N$  data points (Press et al. 1988) it is defined as:

$$Per(\nu) = \langle \left| \sum_{i=1}^N X(t_i) e^{i2\pi\nu t_i} \right|^2 \rangle \quad (3.6)$$

In the equation above, the frequencies occur evenly at  $\nu_{min}, 2\nu_{min}, 3\nu_{min}, \dots, \nu_{Nq}$  where  $\nu_{min} = \frac{1}{T}$  and  $\nu_{Nq} = \frac{N/2}{T} = \frac{N}{2T}$  (the Nyquist frequency). The *spectrum*, or *power spectrum* or *power spectral density* (PSD), is the smoothed version of the periodogram and represents the underlying process. The periodogram fluctuates wildly from one frequency point to the next. At any given frequency it is scattered around the true power spectrum following a  $\chi^2$  distribution with two degrees of freedom.

In my analysis I used the normalized Lomb-Scargle periodogram method (Press & Rybicki 1989). The advantage of this method compared to the normal power spectral density algorithm is that it can be used for unevenly sampled data (i.e. is suitable for our sample of NIR light curves). Given a set of data values  $h_i, i = 1, \dots, N$  at times  $t_i$  the periodogram is defined as

$$P_N(\omega) = \frac{1}{2\sigma^2} \left\{ \frac{[\sum_j (h_j - \bar{h}) \cos \omega(t_j - \tau)]^2}{\sum_j \cos^2 \omega(t_j - \tau)} + \frac{[\sum_j (h_j - \bar{h}) \sin \omega(t_j - \tau)]^2}{\sum_j \sin^2 \omega(t_j - \tau)} \right\} \quad (3.7)$$

where  $\omega$  is the angular search frequency,  $h$  and  $\sigma^2$  are the mean and variance of the data, respectively. The constant  $\tau$  is an offset introduced to keep the periodogram phase invariant:

$$\tan(2\omega\tau) = \frac{\sum_j \sin 2\omega t_j}{\sum_j \cos 2\omega t_j} \quad (3.8)$$

David Palmer (Palmer 2009) has developed a new method (called Fast- $\chi^2$  algorithm) for finding the best-fit function to any chosen number of harmonics, allowing more freedom to find non-sinusoidal harmonic functions. This method is a fast technique (FFT-based) for doing weighted least-squares analysis on arbitrarily-spaced data with non-uniform standard errors. The source code that implements this technique is available to the public<sup>1</sup>. Because data are often not sampled at uniformly spaced

<sup>1</sup><http://public.lanl.gov/palmer/fastchi.html>

discrete times, this method grids the data by sparsely filling a time series array at the sample times. All intervening grid points receive zero statistical weight, equivalent to having infinite error bars at times between samples. The Fast- $\chi^2$  technique is a statistically efficient, statistically valid method of searching for periodicity in data that may have irregular sampling and non-uniform standard errors. It is sensitive to power in the harmonics above the fundamental frequency, to any arbitrary order ( $H$ ):

$$\Phi_H(\{A_{0..2H}, f\}, t) = A_0 + \sum_{h=1..H} A_{2h-1} \sin(h2\pi ft) + A_{2h} \cos(h2\pi ft) \quad (3.9)$$

for the model periodic function. The fit quality is the  $\chi^2$  of all data, jointly minimized over the Fourier coefficients,  $A_{0..2H}$ , and the frequency,  $f$ . I have used this method to check my light curves for periodicities with the harmonics above the fundamental frequency.

Finally, I would like to review some aspects of the noise and the tests for the significance of the detection of any periodic signal (for an extended review see e.g. Press et al. 1988). In many interesting cases time series are the sum of a random component and a periodic signal. One can formulate the time series as

$$X(t) = X_n(t) + X_p(t) \quad (3.10)$$

where the  $X_n$  represents the noisy part while the  $X_p$  is the periodic signal. The PSD of the series will be the sum of the two power spectra (because  $X_n$  and  $X_p$  are considered to be independent)

$$\mathcal{P}(f) = \mathcal{P}_n(f) + \mathcal{P}_p(f) \quad . \quad (3.11)$$

This will be a mixed spectrum which contains narrow features coming from  $\mathcal{P}_p$  and continuous, broad spectral features resulting from  $\mathcal{P}_n$ . The periodogram of the periodic time series contains only narrow features with all power concentrated in them, while the stochastic part will have the power spread over many frequencies. Unfortunately, the periodogram of the stochastic process fluctuates wildly around the true power spectrum. This makes it difficult to distinguish random variations from the real spectral periodic components.

While in the literature there exist well-established methods for the detecting periodic signals when the stochastic process shows a flat PSD (white noise process,  $\mathcal{P}_n = \text{const.}$ ), there is no widely accepted method when the noise PSD is not flat (see Van der Klis 1989 and Vaughan 2010 and references therein). One of the most important aspects in detecting a periodic signal in a PSD with a non-flat (e.g. power-law,  $\mathcal{P}(f) \propto f^\omega$ ) stochastic background is the determination of its slope ( $\omega$ ). Several methods have been proposed to estimate and reduce the background stochastic PSD from the real data

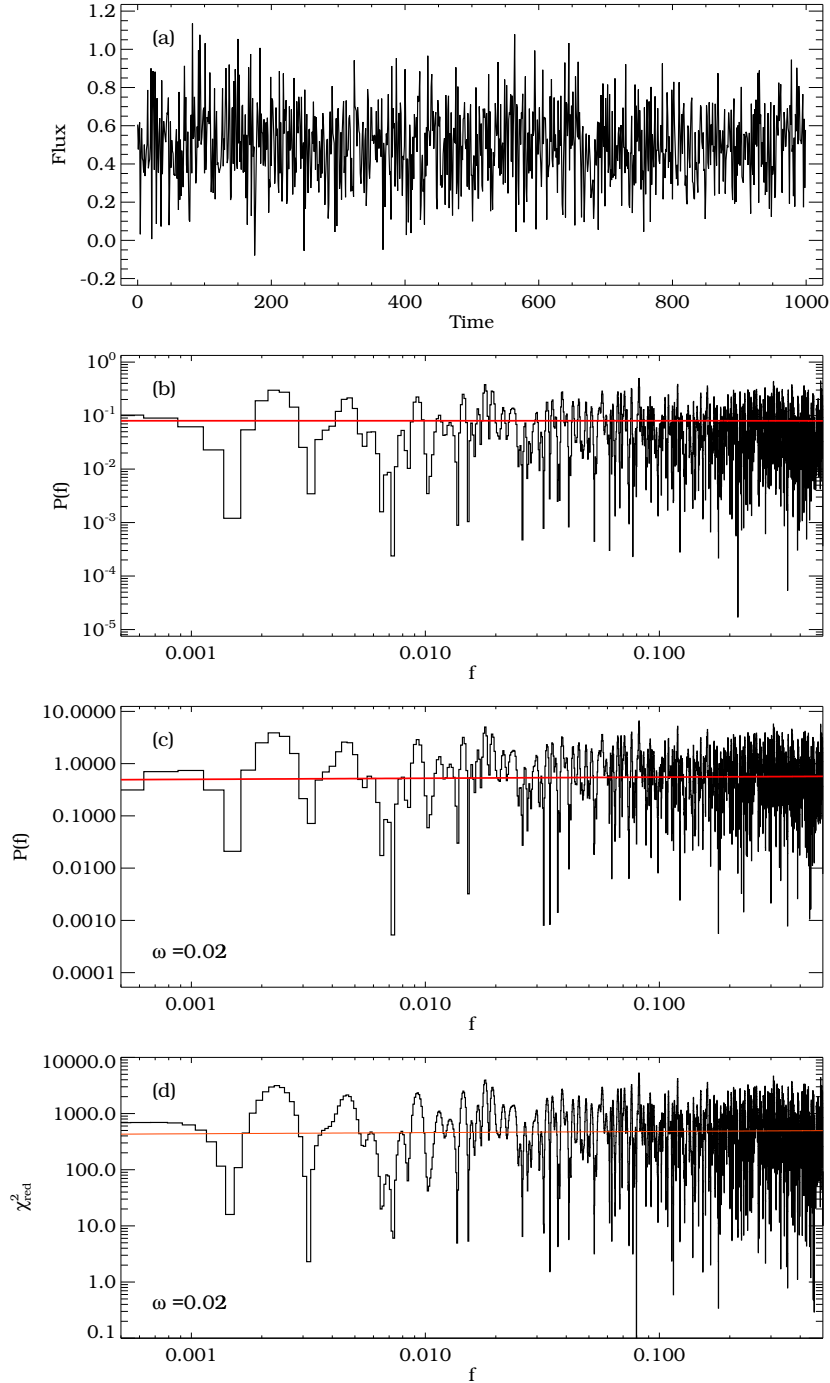


**Figure 3.1:** (a) Simulated random white noise ( $\omega = 0$ ) light curve following the method by Timmer and König (1995). (b) Periodogram (thin black line) and best fit theoretical red-noise spectrum (thick red line) based on the first-order autoregressive method. (c) Lomb-Scargle periodogram (thin black line) and best  $\chi^2$  linear fit to it (thick red line). The estimated value for  $\omega$  is depicted in the left bottom part of the panel. (d)  $F\chi^2$  (Fast- $\chi^2$ ) curve of the flux light curve with  $H = 1$  (thin black line) and the best  $\chi^2$  linear fit to it (thick red line). The estimated value for  $\omega$  is depicted in the left bottom part of each panel.

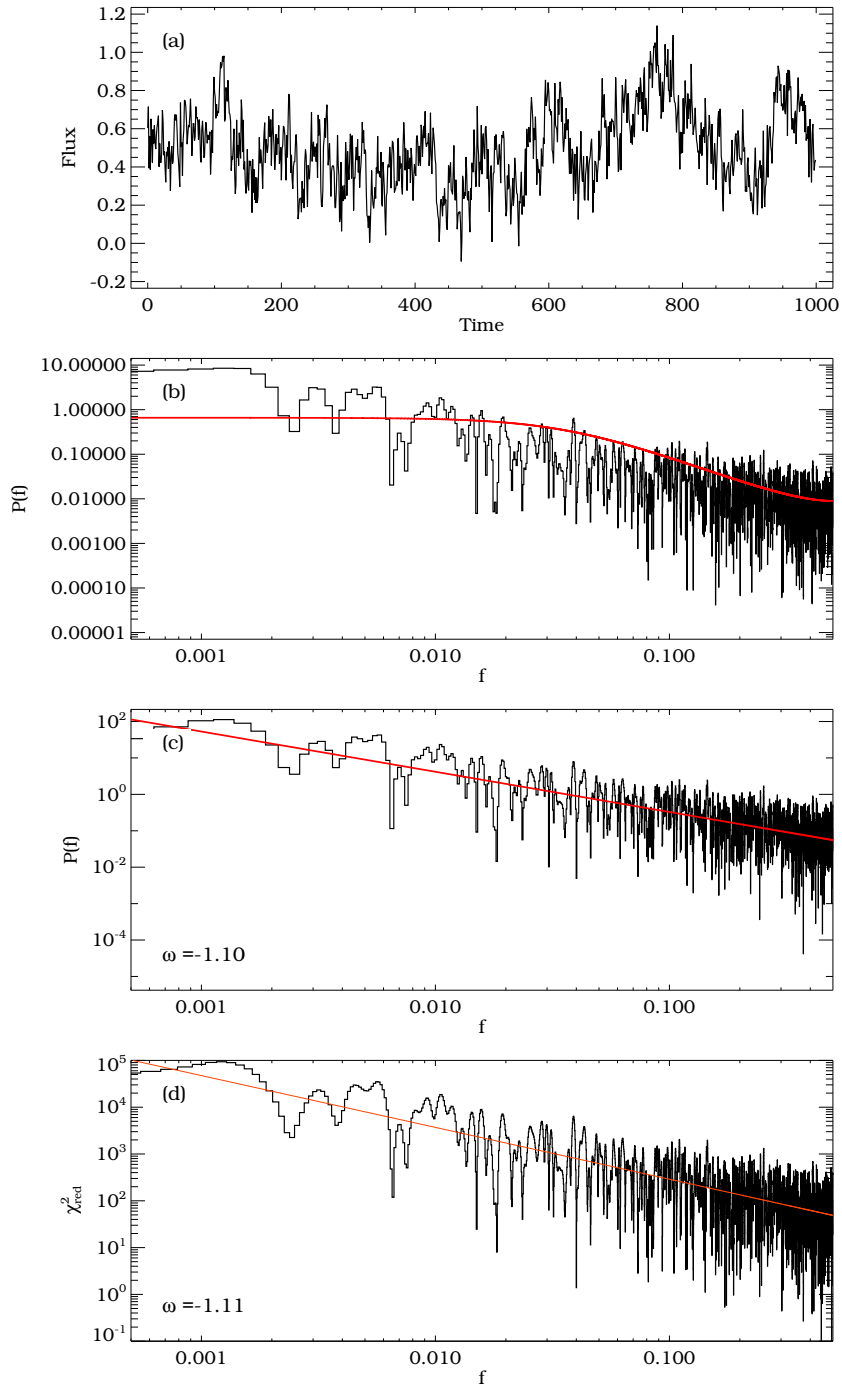


Figure 3.2: Same as Fig. 3.1 for the flicker noise ( $\omega = -1$ ).

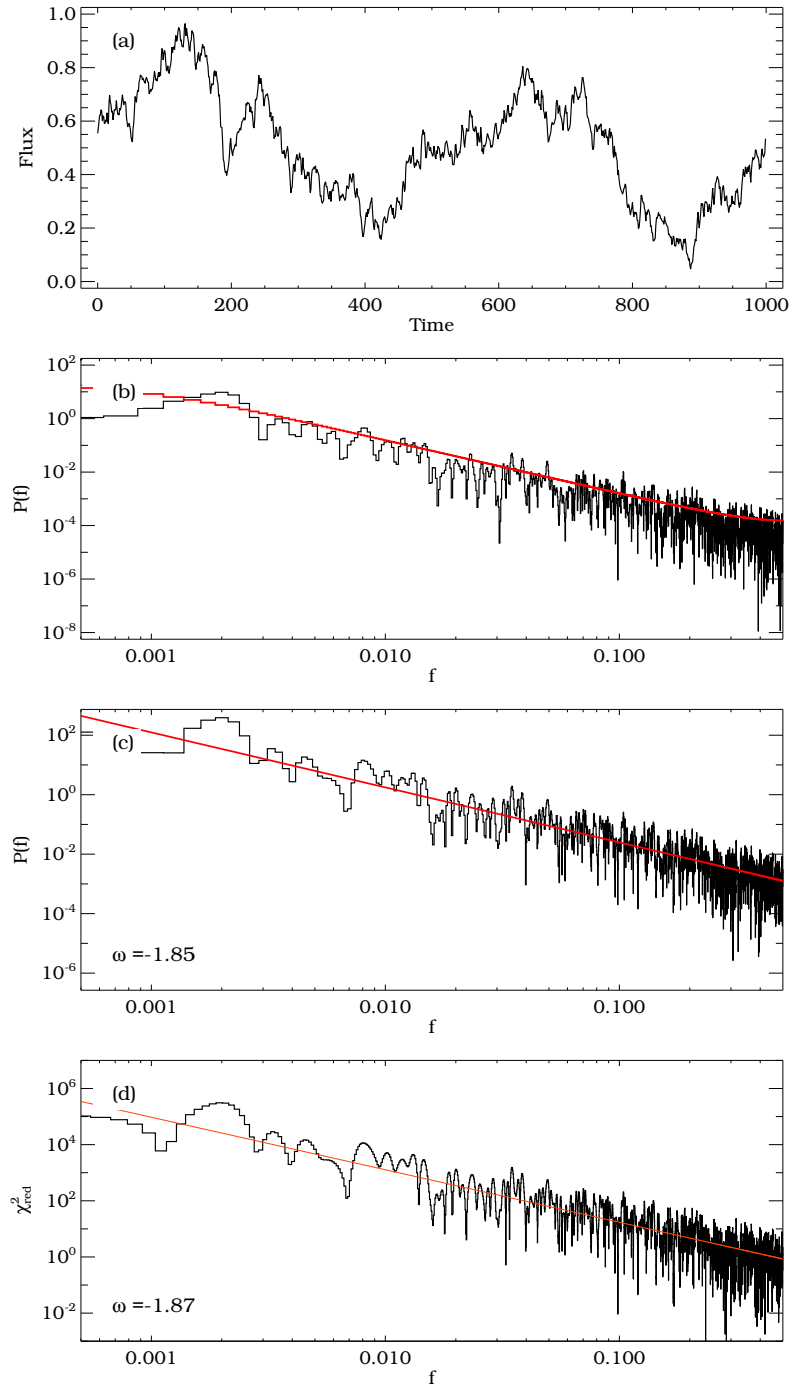


Figure 3.3: Same as Fig. 3.1 for the red noise ( $\omega = -2$ ).

(Vaughan 2005, 2010; Shulz and Mudelsee 2001). Here I have followed the algorithm developed by Shulz and Mudelsee (2001). They have estimated the random noise background by using a first-order autoregressive (AR1) function to the PSD. In this method the AR1 parameter is estimated directly from the unevenly sampled data, so there is no need for interpolation or re-binning. The method includes a significance test for the detection of any spectral peak which may be inconsistent with the first-order autoregressive stochastic origin. This method has been successfully tested for several *real world* examples (Shulz and Mudelsee 2001).

As soon as one can determine the slope of the stochastic background (via a linear fit to the PSD, auto-regressive methods, Bayesian statistics techniques or a combination of all of them) then there is another problem: to create the random time-series which resembles the same power-law spectrum that one can use to derive significance thresholds that the observed PSD could be compared to. In my analysis I have followed the method developed by Timmer and König (1995) for creating random light curves with the expected PSD slopes. To check if any features in the PSD are statistically significant or not, a large number of random light curves with the same  $\omega$  have been simulated and the standard deviations (or in case of non-Gaussian distributed values median deviations) have been derived.

Figures 3.1 - 3.3 show examples of random light curves with the different noise PSD slopes ( $\omega = 0$ ,  $\omega = -1$  and  $\omega = -2$ ; respectively), created with the method developed by Timmer and König (1995). Three different methods of estimating the stochastic background slope are also depicted in the same figures. Since the random light curves are produced by a known spectral slope as input to the Timmer-König algorithm, I have used the comparison between different methods as a tool to see how much the estimated and real value of a the slope are consistent with each other. As one can see, the linear fit estimation can have a deviation from the input slope. This deviation gets larger toward the more red spectra. Through my timing analysis of NIR light curves I have always checked the PSDs with the three different methods.

### 3.1.2 Application to Real Astrophysical Data

Here I will show the application of the methods I reviewed in the previous section to the real astronomical data. For the beginning I have chosen RE J1034+396, an AGN that shows a quasi-periodic behavior in presence of the red-noise background spectrum (Gierliński et al. 2008). The results of the three types of analysis are shown in Fig. 3.4. As one can see, the estimated stochastic background is quite different with different methods when real data are used (i.e. a limited number of data points).

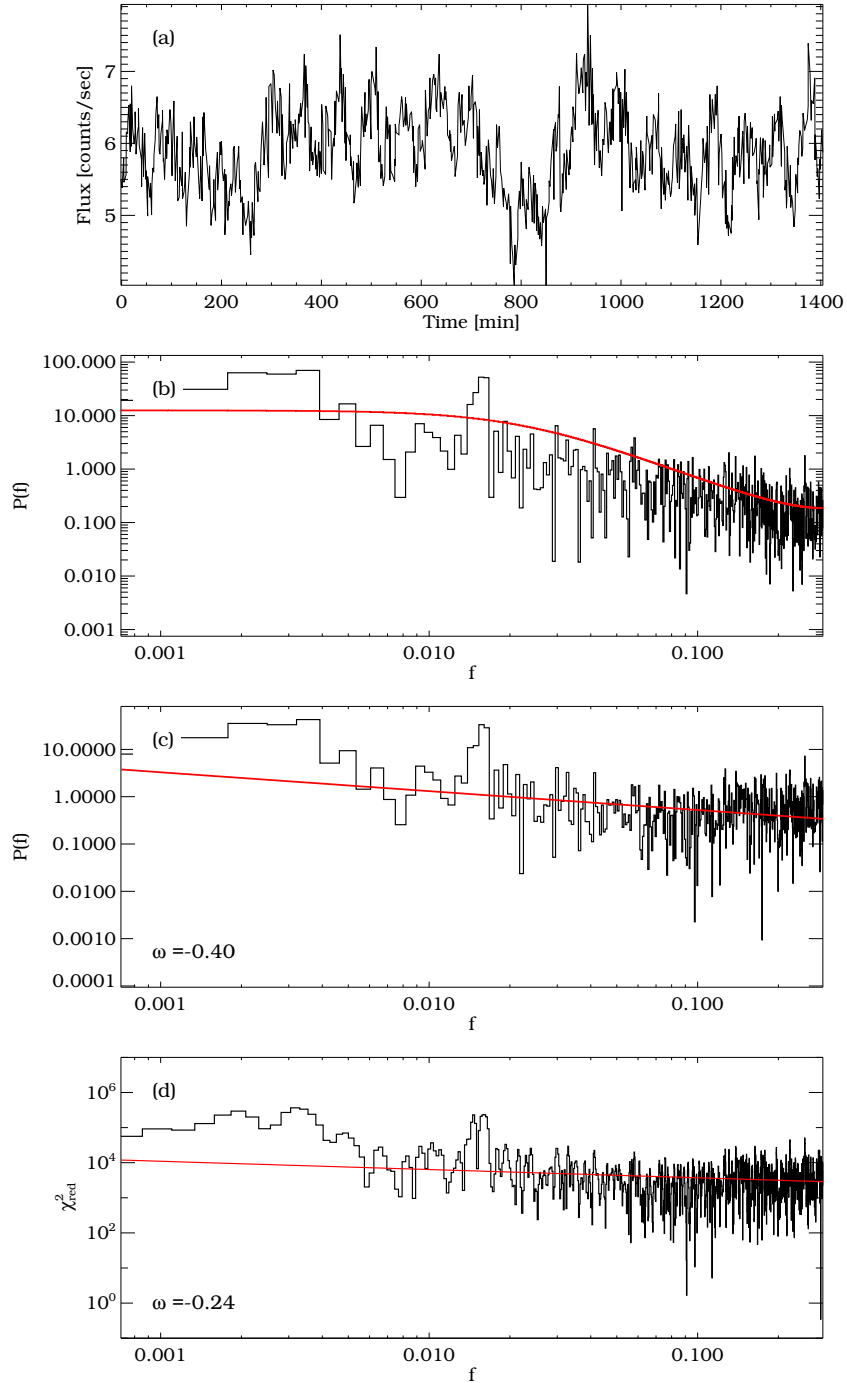


**Figure 3.4:** Same as Fig. 3.1 for the X-ray flux light curve of RE J1034+396 observed by XMM Newton on 2007-05-31 with the starting point at 20:10:12 UTC.

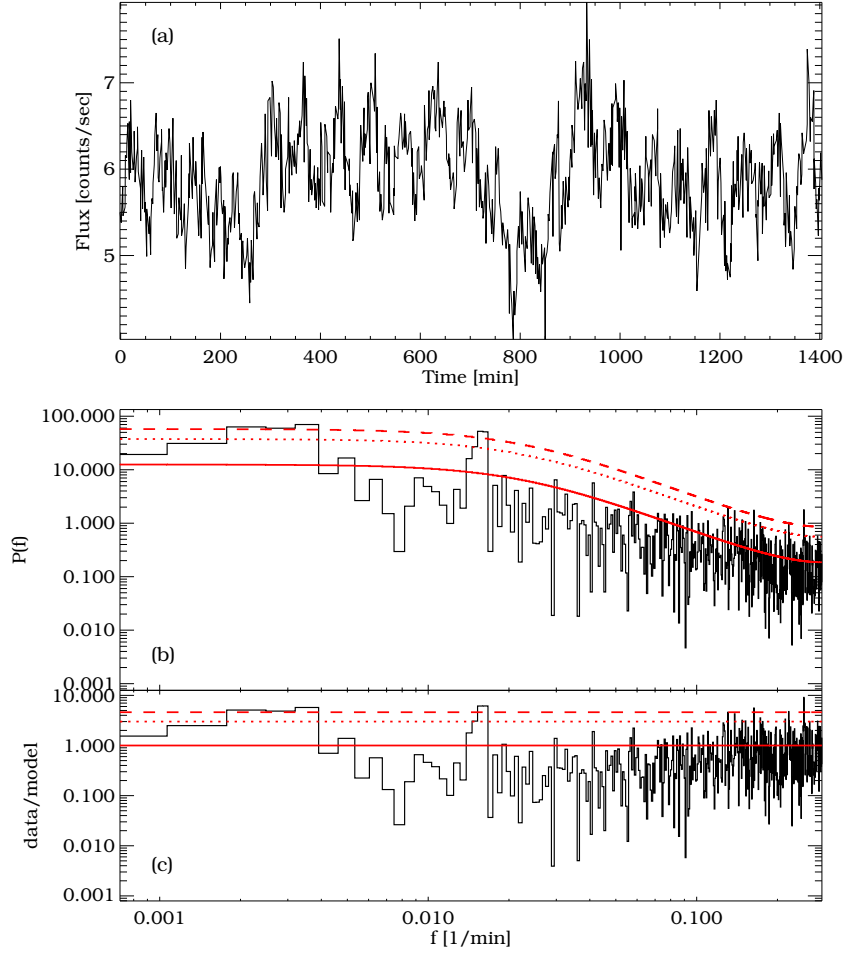


**Figure 3.5:** (a) X-ray flux light curve of RE J1034+396 observed by XMM Newton on 2007-05-31. (b) Lomb-Scargle periodogram of the light curve (thin solid line) and 95% (dotted line) and 99.6% (dashed line) confidence levels. (c) The data/model residual presented on a logarithmic scale for a better view.

Using the AR1 method for estimating the background noise and deriving the levels of significance according to it leads to Fig. 3.5. The periodogram shows a peak at  $\sim 1.6 \times 10^{-2} \text{min}^{-1}$  that is the detected QPO in this source. Here we have the other peak in the low frequency regime which is close to the Nyquist frequency (see Gierliński et al. 2008 and Vaughan 2010). Vaughan (2010) has proposed a new way for removing the colored noise background based on the Bayesian statistics.

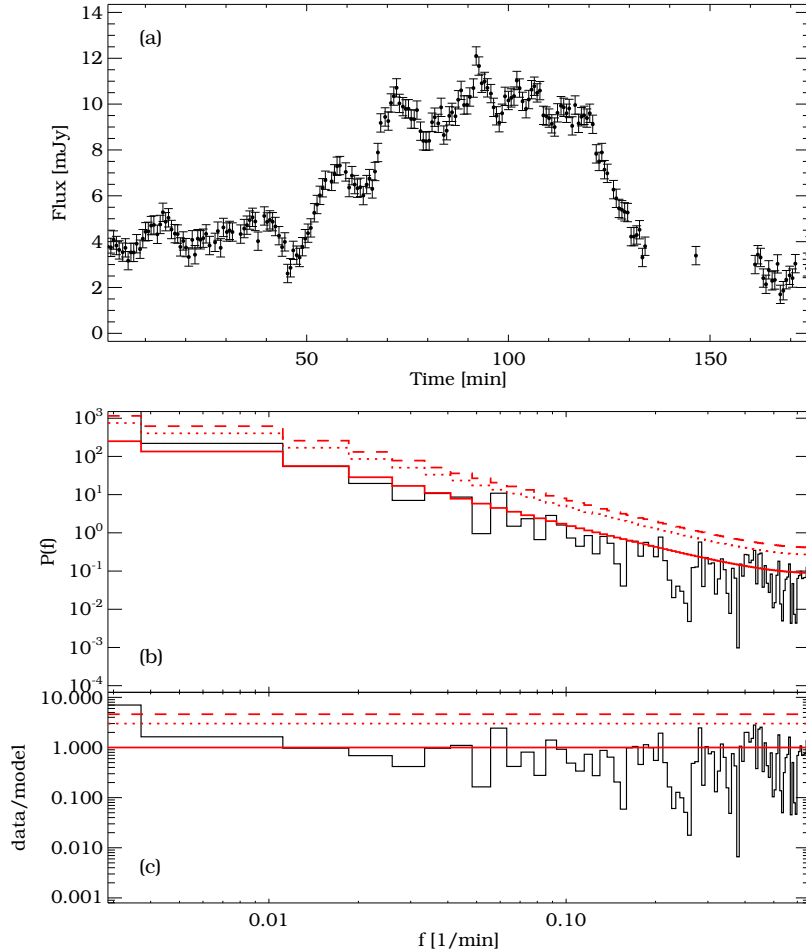


**Figure 3.6:** Same as Fig. 3.5 for the NIR light curve observed on 16 June 2003 (see Genzel et al. 2003). The data was re-reduced by G. Witzel using the ESO archive and a new data reduction pipeline (Witzel 2008).

For more examples, I have applied the same method to the NIR light curves of Sgr A\* observed at different dates using different facilities (VLT, Keck and HST). As the first step Fig. 3.6 shows the Lomb-Scargle periodogram and false alarm thresholds of the first NIR light curve observed during a flaring state of Sgr A\* (Genzel et al. 2003). As one can see there is no significant peak detection of a periodic signal, specially at around  $0.05 \text{ min}^{-1}$  frequency as first claimed to be present in the data (for details see Genzel et al. 2003, Belanger et al. 2006, Meyer et al. 2006a, Do et al. 2008, Zamaninasab et al. 2010 and also the next section). The same analysis is performed on the longest

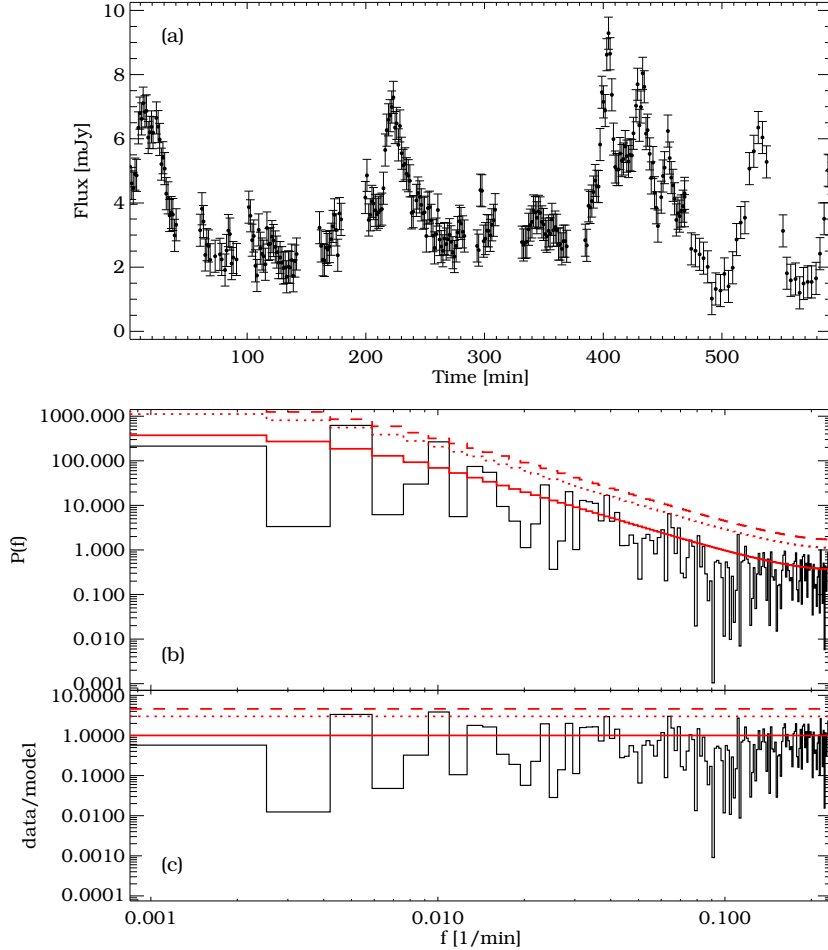


**Figure 3.7:** Same as Fig. 3.5 for the NIR light curve observed on 2005 July 30-31 (see Meyer et al. 2008).

NIR light curves of Sgr A\* observed using VLT, Keck and HST (Figures. 3.7 and 3.8; see also Meyer et al. 2008, Yusef-Zadeh et al. 2009). For the 2005 July 30-31 light curve there is no power above the 99.6% threshold, consistent with the result by Meyer et al. (2009). The result for the HST light curve observed by Farhad Yusef-Zadeh on April 2007 shows a peak at  $\sim 99.6\%$  significance level at around 40 minutes while the Yusef-Zadeh et al. (2009) only reported a peak at about 2 hours. The differences comes from the fact that I have combined all the HST observing windows into one light curve ignoring the fact that there exist huge gaps between them.

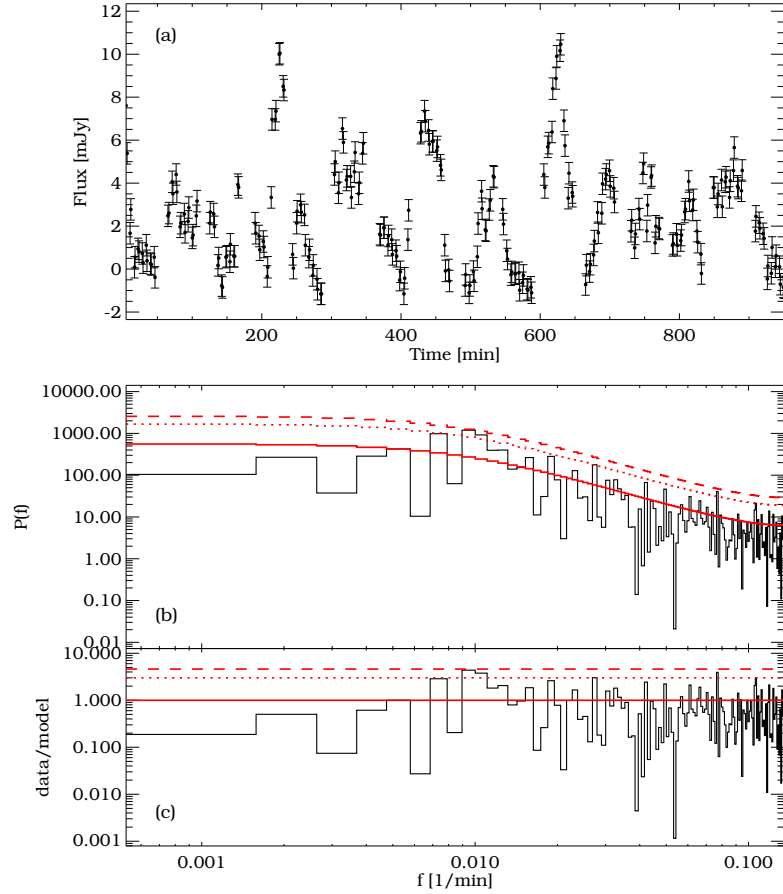


*Figure 3.8:* Same as Fig. 3.5 for the combined HST NIR light curve observed 2007 April 1-7 (see Yusef-Zadeh et al. 2009).

### 3.1.3 Timing Analysis of the Sample of Polarimetric NIR Light Curves of Sgr A\*

#### 3.1.3.1 Autocorrelation

As I discussed in the previous chapter, Fig. 3.9 shows flare events observed in the NIR K-band ( $2.2\mu\text{m}$ ) on 13 June 2004, 30 July 2005, 1 June 2006, 15 May 2007, 17 May 2007 and 28 May 2008. This sample includes all flare events observed in NIR polarimetry during recent years according to my knowledge. The flux densities rise and come back to their quiescent level in time intervals of roughly 100 minutes. The measured values

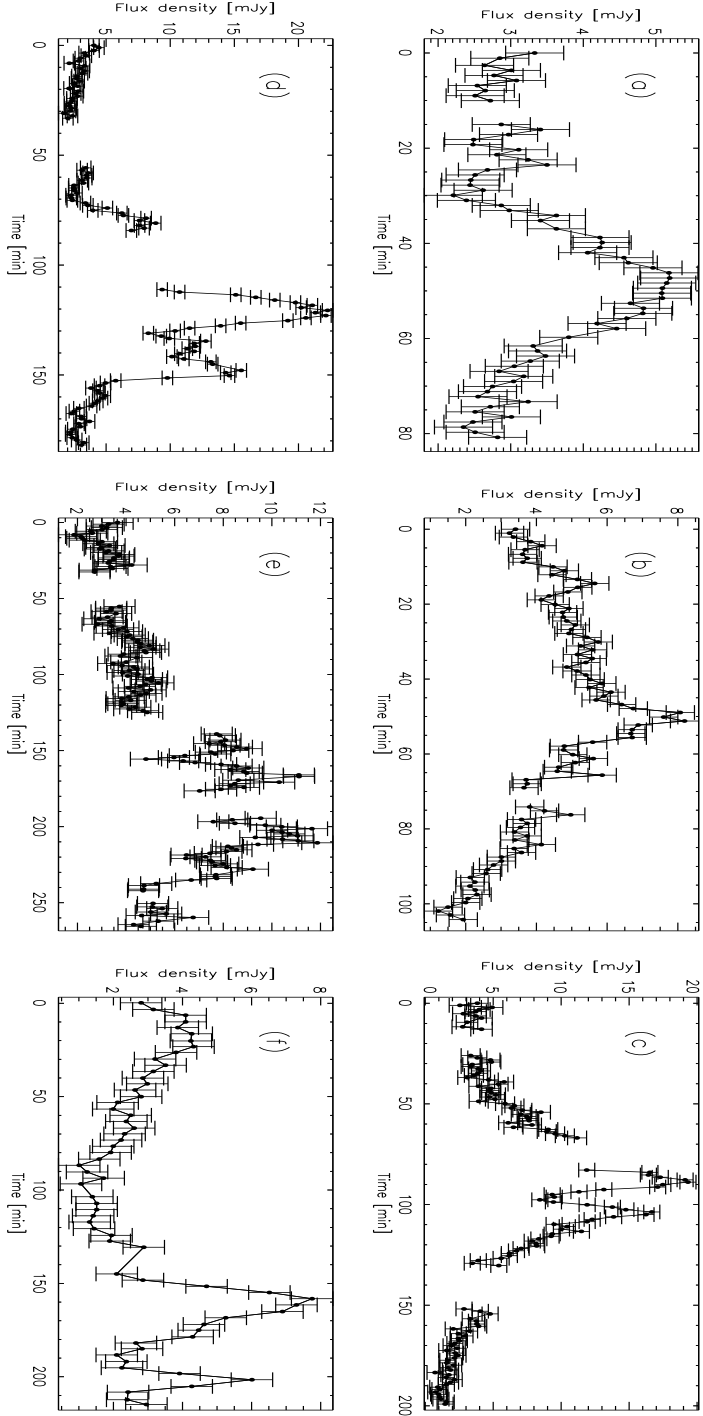


**Figure 3.9:** Our sample of light curves of Sgr A\* flares observed in NIR K<sub>s</sub> band ( $2.2\mu\text{m}$ ) polarimetry mode. The events were observed on 13 June 2004 (a), 30 July 2005 (b), 1 June 2006 (c), 15 May 2007 (d), 17 May 2007 (e) and 28 May 2008 (f). Each panel shows the de-reddened flux density measured in mJy for that event. The gaps in the light curves are due to the sky background measurements.

of total flux, degree of polarization, and angle of polarization vary significantly on time scales of  $\sim 10$  minutes. These abrupt changes can be more clearly detected when the events are in their brightest state. Even if the flares are different in some aspects (e.g. the ratio of the flux variations, the maximum brightness achieved, or the degree of linear polarization) there could exist some repetitive features in our sample. Here I perform a quantitative analysis in order to probe such features, focusing first on detecting periodic signatures in flux density light curves.

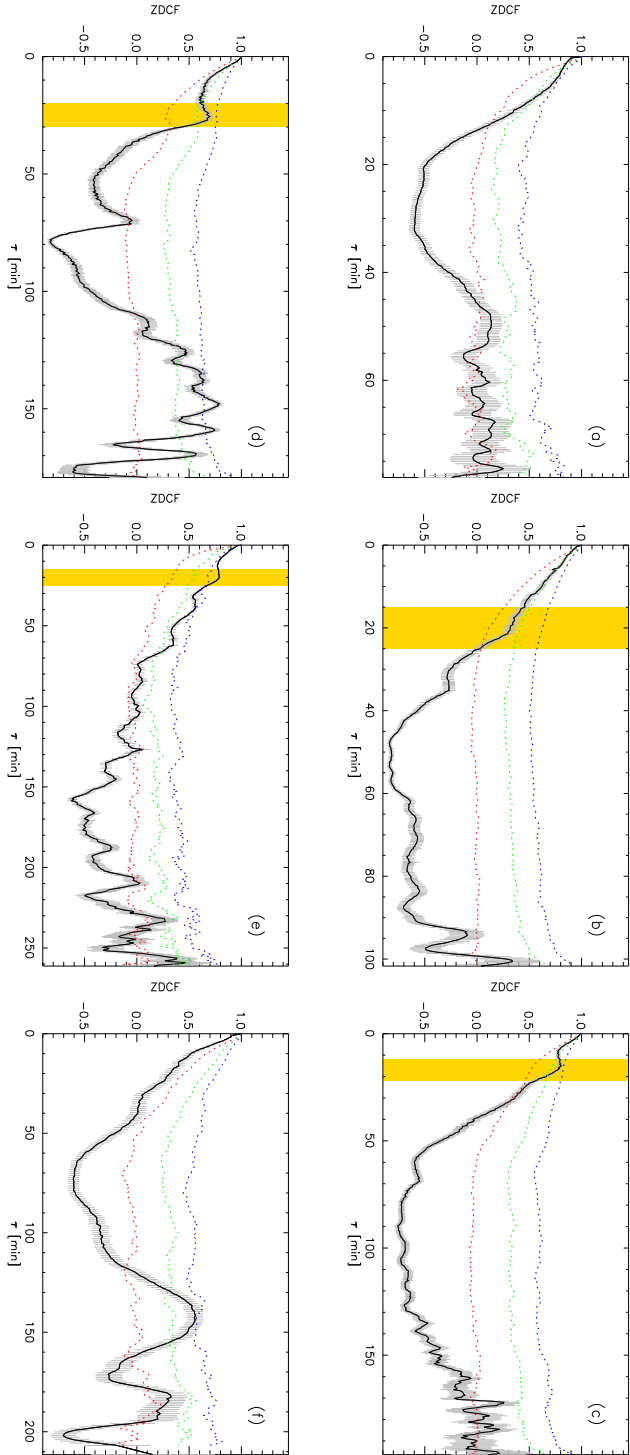
The autocorrelation function and Lomb-Scargle periodograms can be used to detect signatures of time periodic structures (see section 3.1.1). For autocorrelation analysis I used the z-transformed discrete correlation function (ZDCF) algorithm (Alexander 1997), which is particularly useful for analyzing sparse, unevenly sampled light curves. For Lomb-Scargle periodograms I followed Press and Rybicki (1989).

Figure 3.10 shows the cross-correlation of the flux density light curves of our sample with themselves by using ZDCF method. The ZDCF of the 30 July 2005, 1 June 2006, 15 and 17 May 2007 flares show peaks around  $20 \pm 5$  min time-lag and specially for 15 and 17 May 2007 the peaks look significant. These peaks can be signs of a possible periodicity. But as one can see, only the 17 May 2007's ZDCF shows a peak above the 99.8% significance threshold. The false alarm values have been derived by repeating the same ZDCF analysis on the  $10^4$  random red-noise light curves. The criteria for this comparison and the way the light curves are produced are described below. Here I must note that since the ZDCF values are normalized and distributed in  $[-1:1]$  interval, the distribution of the values for each time lag ( $\tau$ ) is not Gaussian (see Fig. 3.11). As a result I have used the median and percentile nomenclature instead of the normal standard deviation formalism for deriving the false alarm levels.

I have highlighted the time windows in which ZDCFs show a peak around  $20 \pm 5$  min, coinciding with the claimed quasi-periodicity. Even though the 1 June 2006 and 15 May 2007's ZDCFs do not show peaks above 99.8% significance, they still however reach 99% and 95.4% levels, respectively. Also, by a rough estimate, the significance of the ZDCF peaks are correlated to the brightness of the flares and for the faint events, as is observed for example in 2004, there is no detectable peak.

### 3.1.3.2 Periodogram

Figure 3.12 shows again the Lomb-Scargle periodograms of the NIR light curves sample shown in Figure 3.9. All periodograms show power law behavior,  $\mathcal{P} \propto f^\omega$ , showing greater power at lower frequencies. Here  $\mathcal{P}$  is power,  $f$  is frequency and  $\omega$  is power



**Figure 3.10:** ZDCF of the flux light curves of 13 June 2004 (a), 30 July 2005 (b), 1 June 2006 (c), 15 May 2007 (d), 17 May 2007 (e) and 28 May 2008 (f). The vertical colored boxes indicate the position of the closest peaks to the zero time lags. Dotted lines show the median (red), 68.3% (green) and 99.8% (blue) thresholds derived from  $10^4$  red noise simulated light curves.

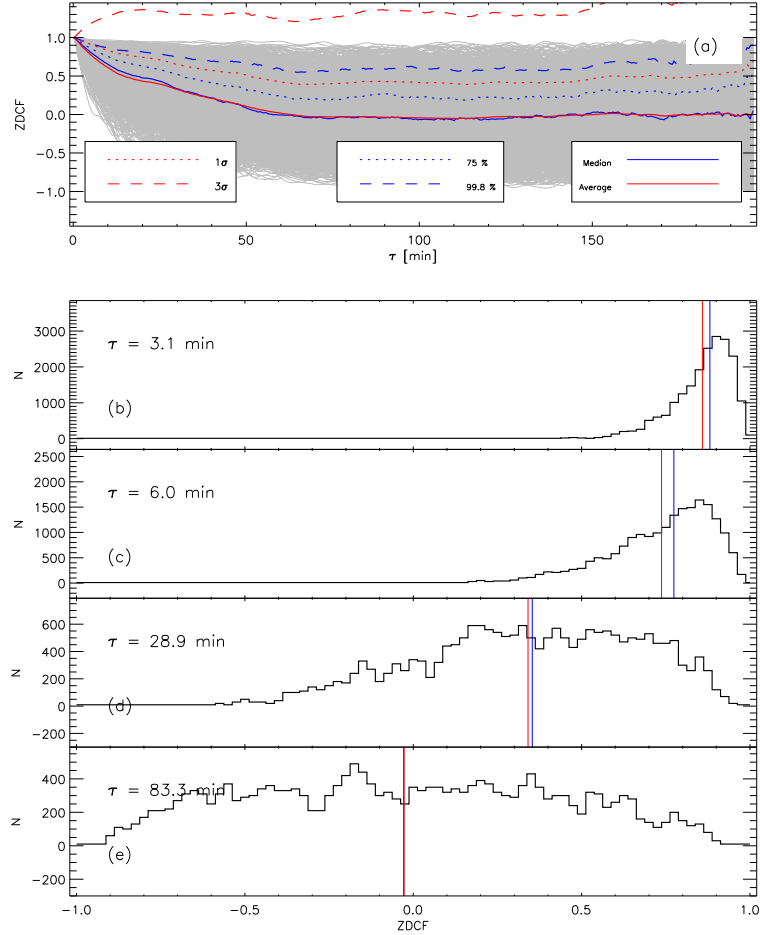


**Figure 3.11:** ZDCF of  $10^4$  simulated red noise light curves over-plotted in one image (a). The resultant average and standard deviation, as well as the median and percentile values are presented. The distribution of ZDCF values for different time lags ( $\tau$ ) are also depicted (b-e); they clearly show non-Gaussian distributions, specially for small values of  $\tau$ .

law index. All light curves follow a red noise underlying power spectral density with  $-1.19 \leq \omega \leq -1.77$  (derived from a linear fit, see below). The best theoretical fit for the background colored noise derived from the first auto-regressive function fit, and the corresponding false alarm levels, have been depicted in the same figure. For each event the corrected PSD after dividing by the theoretical background is also presented. One can see that only the 17 May 2007 light curve shows a peak around  $17 \pm 2$  min which reaches close to the 99.6% false alarm level (panel e). This can be seen better in the

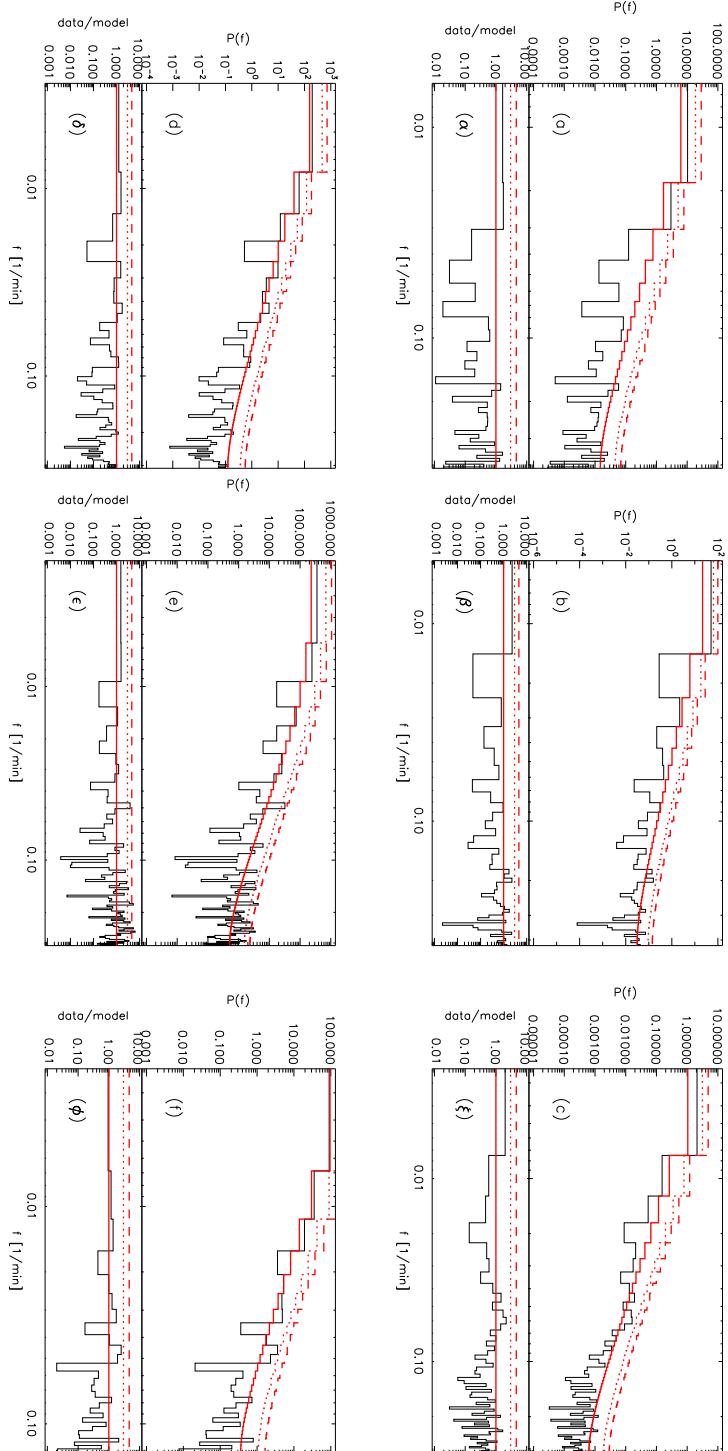


**Figure 3.12:** Lomb-Scargle periodograms (thin solid lines), best theoretical fit for the underlying red noise (thick red line), 95% (dotted line) and 99.6% (dashed line) levels of confidence for the flux light curves for 13 June 2004 (a), 30 July 2005 (b), 1 July 2006 (c), 15 May 2007 (d), 17 May 2007 (e) and 28 May 2008 (f). The data/model residuals are also presented for a better view (panels  $\alpha - \phi$ ).

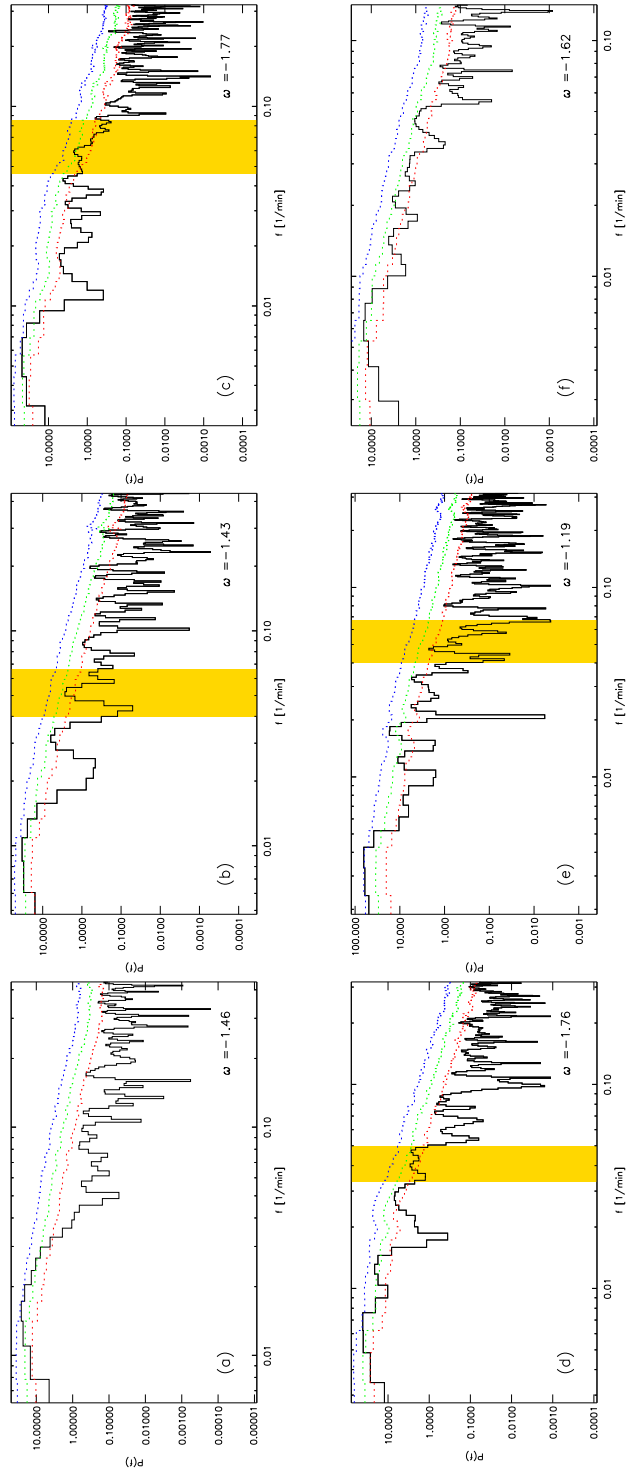


**Figure 3.13:** Lomb-Scargle periodograms of the flux light curves for 13 June 2004 (a), 30 July 2005 (b), 1 June 2006 (c), 15 May 2007 (d), 17 May 2008 (e) and 28 May 2008 (f). The dashed lines show the median (red) and 68.3% (green) and 99.8% (blue) thresholds derived from  $10^4$  red noise simulated light curves. The highlighted boxes show the band of frequencies that have corresponding ZDCF peaks.

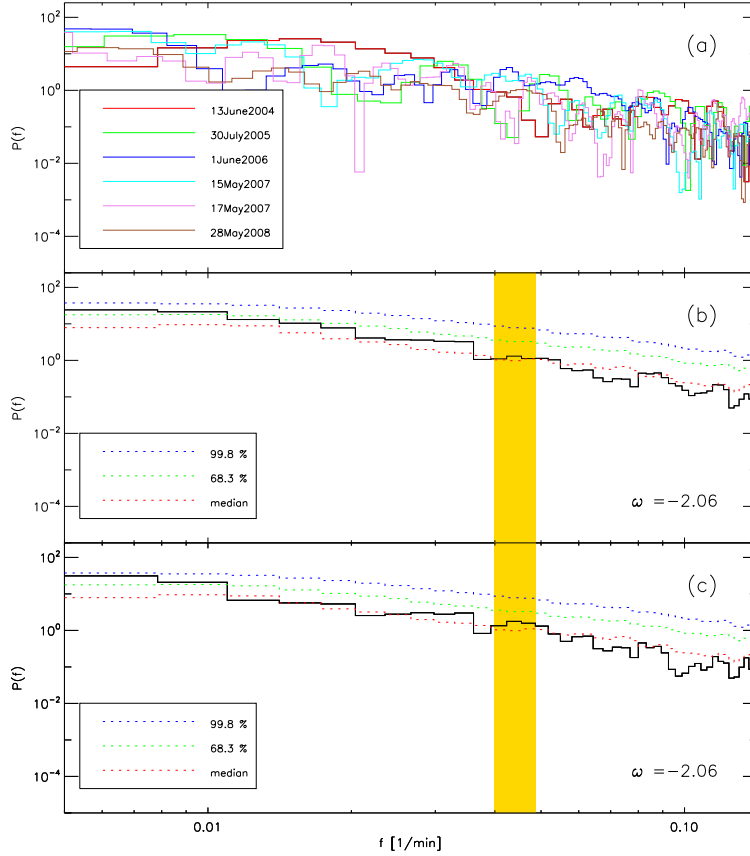


**Figure 3.14:** Lomb-Scargle periodograms of the flux light curves of our sample over-plotted in the same plot (a). Averaged result of all periodograms together (b) and excluding the 13 June 2004 flare (c). Highlighted box shows the expected  $20 \pm 5$  minutes periodicity band.

corresponding  $\frac{\text{data}}{\text{model}}$  plot (Fig. 3.12 panel  $\epsilon$ ).

Figure 3.13 shows the Lomb-Scargle periodogram for each flux light curve. This time a factor of 4 times over-sampling was applied in order to increase the sensitivity. To test the significance of the peaks in the periodogram I have repeated the Lomb-Scargle analysis for  $10^4$  simulated red noise light curves. For simulating the red noise I have followed the algorithm by Trimmer and König (1995) (see Figs. 3.1, 3.2 and 3.3 for examples). The red noise light curves were produced for each event separately following the procedure below: (1) Determining the slope of the observed PSD for each event using a linear fit to the periodogram in log-log space (the resulted  $\omega$  is presented in the

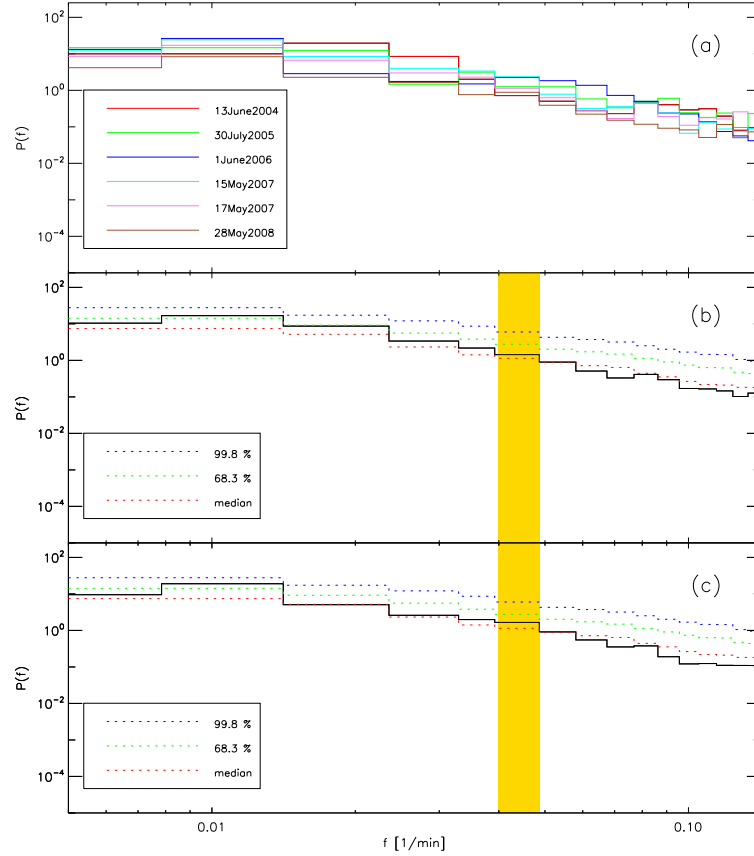


**Figure 3.15:** Same as Fig. 3.14 but averaged for a band of frequencies with the same size as highlighted region.

lower right corner of each plot in Fig. 3.13). (2)  $10^4$  red noise light curves produced with the related  $\omega$  following the method of Timmer and König (1995).

The light curves have been produced by selecting the middle part of a light curve with a length at least 10 times longer than the observed light curve following the argument by Uttley et al. (2002). The selected segment of the light curve is sampled to the same time bin of the corresponding observation. This will correct for any artificial effects caused by time lags which exist in our light curves, and also for the uneven sampling of our observations. (3) The value of the flux has been multiplied by a factor as the mean of the simulated flux has the same value as the observational one for each night.

Almost none of the periodograms of Fig. 3.13 shows a peak that exceeds the 99.8%

threshold except the ones correlated to the lengths of the flare events (for the case of 17 May 2007 light curve one can see that two methods of estimating the underlying red-noise gives different results). I specially highlighted the windows in which the corresponding ZDCFs peak. In order to see if there exists a persistent frequency peak in the PSDs, I averaged together all observed periodograms (Fig. 3.14 (b)). The average periodogram does not show a significant peak in comparison with the false alarm level even if I exclude the 13 June 2004 light curve (Fig. 3.14 (c)). As I mentioned before, the short time scale of the flares and limited number of cycles make a significant detection of any periodicity very difficult. In addition, the possible quasi-periodic structure can be variable during the flare if it is connected to the falling clumps of matter into the black hole (Falanga et al. 2008). In this case the Lomb-Scargle algorithm finds different frequencies and allocates them separate values of power. This effect can result in a periodogram in which the values of power are higher in a band of frequencies instead of a specific value. As one can see in Fig. 3.13, 1 June 2006 and 15 May 2007 can be the candidates for such an effect, since the value of PSD function remains high in the highlighted window. To test for such an effect, I averaged the periodograms with a new bin size and repeated the same procedure for the random red noise PSDs (Fig. 3.15). Again, the resulted averaged periodogram does not show any significant peak (Fig. 3.15 (b)), even if I exclude the 13 June 2004 event (Fig. 3.15 (c)). Since this procedure is very sensitive to the size of the chosen window (which can vary from event to event), a more detailed analysis is needed to study the possible evolution of any periodic signal.

## 3.2 Cross-correlation Analysis

### 3.2.1 Importance of Polarimetry

Here I focus on finding any possible correlation between changes in flux and polarimetric light curves. I have performed cross correlation analysis between variations of flux and degree (angle) of polarization. A search for any short time-lag correlation has been carried out by scanning the light curves using a sliding window method (see Fig. 3.18 panel (a)). The size of the scanning window ( $\epsilon$ ) is fixed at 40 minutes since I am interested in magnifying any short lag correlation related to the possible  $20 \pm 5$  minutes quasi-periodicity. Fig. 3.16 shows the cross-correlations of the two sets of mentioned light curves for all events in our sample. The time steps of the scans were fixed to be 5 minutes. The presented results are the average of all scans weighted by the flare signal to noise ratio (i.e. each part of the flare that is brighter has more weight). Since the ZDCF algorithm needs at least 11 points per bin for reliable results (specially for the error estimation; see Alexander 1997), a linear interpolation of the polarimetric data

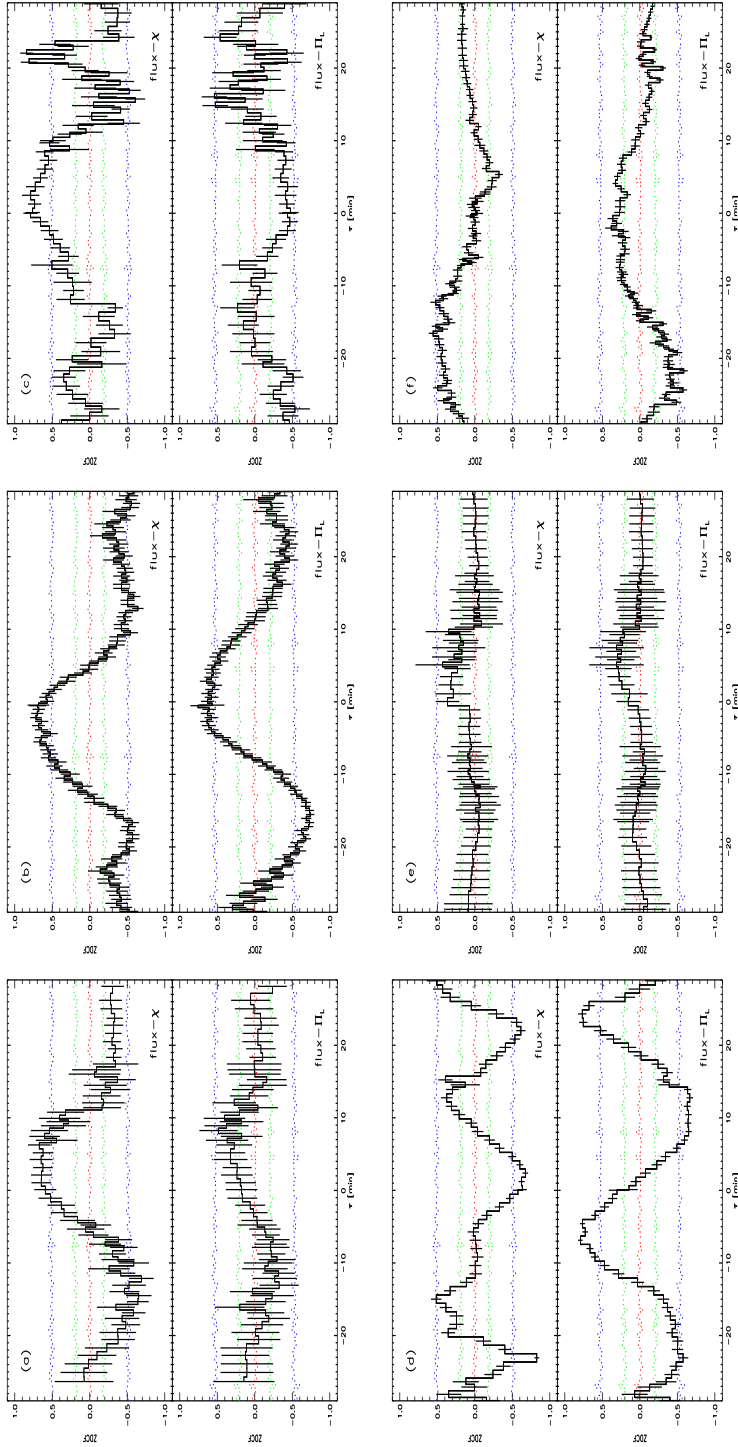


**Figure 3.16:** Cross-correlation between the flux and polarization angle (degree) light curves of Fig. 2.4 [13 June 2004 (a), 30 July 2005 (b), 1 June 2006 (c), 15 May 2007 (d), 17 May 2008 (e) and 28 May 2008 (f)]. In each panel, top (bottom) shows the correlation between the flux and the polarization angle (degree of linear polarization). Dashed lines indicate the position of the median (red), 68.3% (green) and 99.8% (blue) significance levels derived from  $10^4$  simulated red noise light curves.

points has been performed. I must mention that due to the confusion from nearby stars and the diffuse background emission, the accuracy of measuring polarimetric parameters is related to the brightness of Sgr A\*. This means that the most reliable polarimetric data are measured when strong flares happen, specially when the source is in its brightest state.

In order to test whether a random red noise model can produce the same correlation patterns I needed to simulate red noise light curves including polarimetric data. For this purpose, I have simulated random  $E$  vectors for four perpendicular directions:

$$\vec{E}_\theta = E_\theta e^{-i\phi t} \hat{\theta} \quad (3.12)$$

where  $\theta = 0^\circ, 45^\circ, 90^\circ, 135^\circ$ ,  $\hat{\theta}$  is the corresponding normal vector,  $\phi$  is the phase and  $E_\theta$  is a random value following the algorithm by Trimmer and König (1995). Following the detection of the signal, including the cross-talk from non-orthogonal neighboring channels, the polarized flux in each channel is then produced by using the Mueller matrix formalism. The resultant four different channels ( $F_0, F_{45}, F_{90}$  and  $F_{135}$ ) show the same power law index (Fig. 3.17 (a)). Using

$$F = F_0 + F_{90} \quad (3.13)$$

$$Q = F_0 - F_{90} \quad (3.14)$$

$$U = F_{45} - F_{135} \quad (3.15)$$

$$\chi = \frac{1}{2} \arctan\left(\frac{U}{Q}\right) \quad (3.16)$$

$$\Pi_L = \frac{\sqrt{Q^2 + U^2}}{F} \quad (3.17)$$

(where  $F$ , is the total flux,  $Q$  and  $U$  are the Stokes parameters,  $\chi$  is the polarization angle and  $\Pi_L$  is the degree of linear polarization) the flux and polarization light curves for each set can be derived. Fig. 3.17 shows examples of such light curves with three different PSD slopes:  $\omega = 0$  (white noise),  $\omega = -1$  (flicker noise) and  $\omega = -2$  (red noise).

As one can see in Fig. 3.17, for  $\omega = -2$  some random correlations between changes in the total flux and polarimetric parameters can occur. In order to see whether the observed correlations in our sample are just the same random coincidences or they show signs of a more subtle process, I have simulated  $10^4$  artificial light curves for each value of  $\omega$  as derived from the average PSD of observations. Then for each set of light curves the correlation function between flux and polarization angle (degree) has been

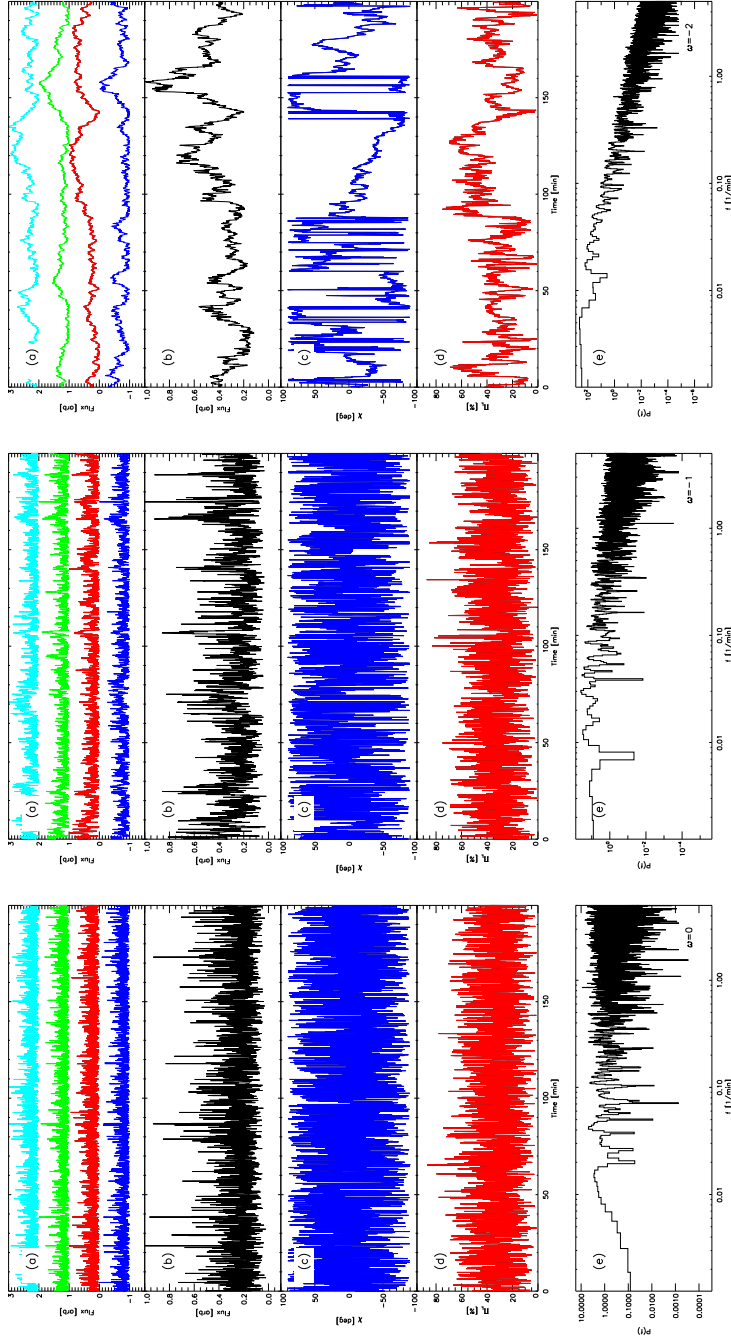


**Figure 3.17:** Left: (a) Simulated light curves of four different polarimetric channels all showing white noise behavior ( $\omega = 0$ ). (b) Total flux. (c) Angle of polarization. Middle: (d) Degree of polarization. (e): Lomb-Scargle periodograms of the total flux. Right: Same as the left panel for  $\omega = -1$  (flicker noise). Same as the left panel for  $\omega = -2$  (red noise).

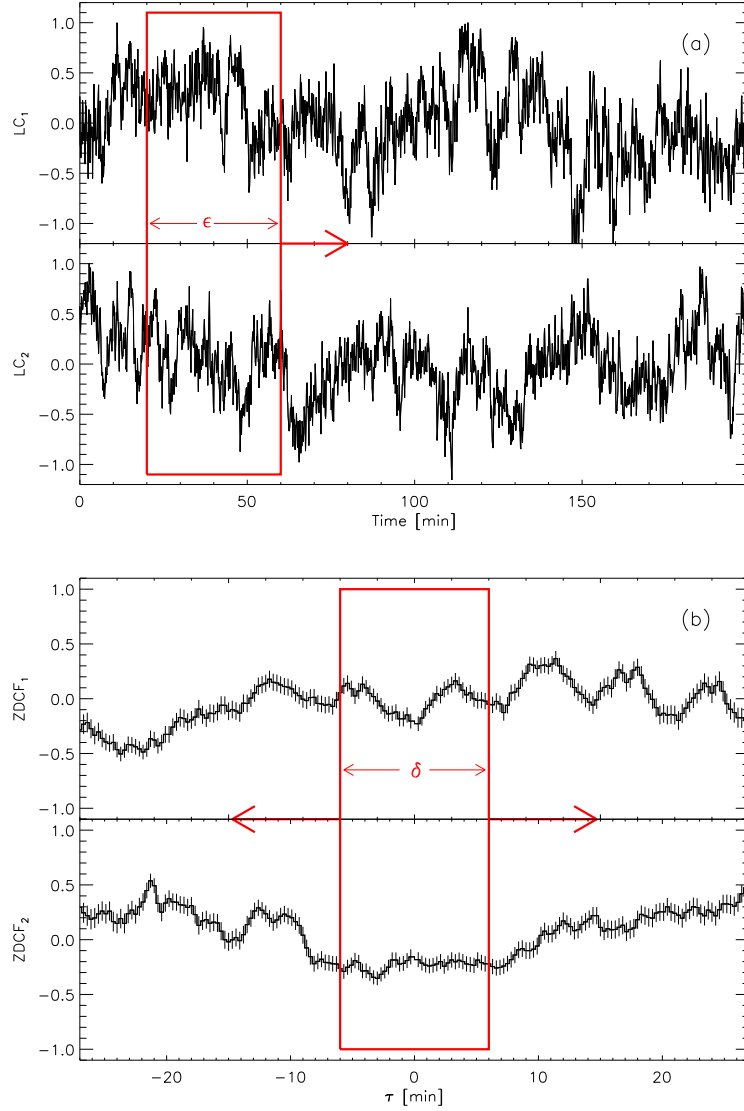


**Figure 3.18:** (a) Sketch showing how the cross-correlations of Fig. 3.16 have been derived. A moving window of the size  $\epsilon$  scans flux and polarization angle (degree) light curves. The final cross-correlation is the average of all windows. (b) Sketch showing how the probability function in Fig. 3.19 has been derived. The algorithm finds the number of events in which two ZDCFs show at least one point over  $3\sigma$  threshold of red noise correlation in a window of size  $\delta$ . By repeating the same procedure for  $10^4$  cross-correlation of red noise light curves the probability that a significant correlation is expected to happen in that window is derived.

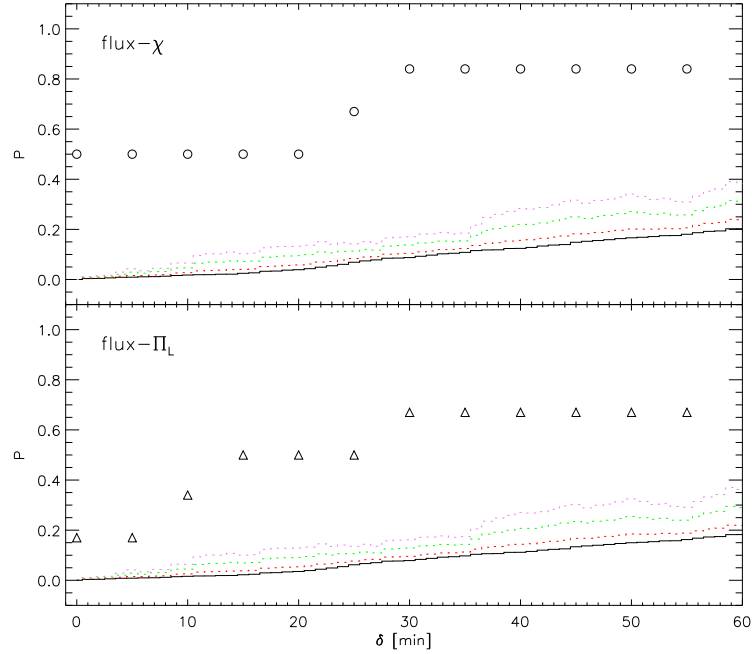


**Figure 3.19:** Top: Probability that two sets of  $10^4$  simulated red noise light curves show significant correlation between total flux and polarization angle in a window of the size  $\delta$  minutes (solid line). Bottom: Same as top panel for the correlation between flux and polarization degree. Dotted lines show  $1\sigma$  (red),  $3\sigma$  (green) and  $5\sigma$  (violet) levels of confidence for the probability function, calculated by repeating the whole analysis 100 times. The circles and triangles indicate the probabilities derived from our sample of NIR light curves (see Fig. 2.4 and 3.16).

calculated. Dashed lines in Fig. 3.16 show the median, 68.3% and 99.8% false alarm values. One can see that some of the observed correlations are above 99.8% significance level. Even though most of the mentioned cross-correlation peaks happen around the same value (around zero time-lag), all of them are not exactly in the same  $\tau$ . To examine how probable it is that a strong deviation from the average in the red noise simulation repeatedly happens in a specific window I have calculated the probability that the mentioned cross correlations show significant peaks (above 99.8%) in a window of size  $\delta$  (see Fig. 3.18 (b)).

Figure 3.19 shows this probability as derived for the simulated light curves (solid line) and observations (circles and triangles). This analysis shows that it is very unlikely to observe correlation between total flux and polarimetric parameters approximately at the same time lags (small  $\delta$ ) while our observations show that strong correlations exist

in the light curves of Sgr A\* and repeat themselves for approximately the same time lag. I must note here that the value derived for the observed probability in Fig. 3.19 (circles and triangles) are derived from a sample of only 6 sets of light curves. In order to make a more reliable statistical analysis more NIR observations of Sgr A\* in polarimetric mode must be done in the future. Furthermore, the method described here can in principle be used for polarimetric observations of other sources showing the same variability; this may help in understanding the general underlying physical process causing this kind of behavior.

The physical models which have been already proposed to simulate the observed red-noise light curves of AGNs (Lyubarskii 1997; Armitage & Reynolds 2003, Vaughan et al. 2003) would have difficulties in reproducing this type of correlation between the behavior of polarimetric parameters and the total flux. As a result, the observed correlation between changes in flux and polarimetric data suggests a way to distinguish between the possible physical processes responsible for the overall red-noise behavior. A semi-analytical study by Pecháček et al. (2008) showed that a signal generated by an ensemble of spots randomly created on the accretion disk surface can produce red noise signals with PSD slopes of the order of -2. In their simulations the spot generation is governed by Poisson or Hawkes processes (see Pecháček et al. 2008). In combination with our observations of Sgr A\* the spotted disk scenario is a possible explanation for this commonly observed red noise behavior, while some exceptionally luminous events can show their signature in polarized light. This could point out to the transient occurrence of QPOs that may appear recurrently during the bright flares, which seems to be a rather natural possibility. This will be discussed in the next sections in detail.

## Chapter 4

# Modeling

$$\binom{n}{m} = \binom{n-1}{m-1} + \binom{n-1}{m}$$

-A. Karaji (953 AD - 1029 AD)  
Mathematician and engineer.

$$(a + b)^n = \sum_{k=0}^n \binom{n}{k} a^k b^{n-k}$$

-Omar Khayyám (1048 AD - 1131 AD)  
Astronomer, mathematician, philosopher,  
physician and poet.

In this chapter, I first describe in detail the emission model I have used in the simulations, which is mainly based on synchrotron emission from accelerated electrons in the inner parts of a relativistic accretion disk. I also describe the ray-tracing method which is used, and the predictions of the model.

### 4.1 Inner Parts of an Accretion Disk

Since the discovery of X-ray and NIR flares from Sgr A\*, several theories tried to describe the physics behind them, varying from abrupt changes in the accretion rate of

a Keplerian disk (Melia et al. 2001) to the interaction of the accretion disk with nearby stars (Nayakshin et al. 2004). Although none of these scenarios can be ruled out, there are observational evidences that give more support to some of them. For example, as I mentioned before, the frequent observed rate of NIR flares (4-5 flares/day) makes it hard for disk-star interaction or tidal capture scenarios to describe the events.

Of special interest to us are the observed quasi-periodic flux modulation during the NIR and X-ray flares. The recent unambiguous discovery of (quasi-)periodicity in an active galaxy (RE J1034+396) reported by Gierliński et al. (2008), brings more support to the idea that the similarity in behavior of black holes extends from stellar-mass black holes to super-massive ones. The most interesting scenario could be a relation to the orbital time scale of the accretion disk, with a possible connection to the plunging region which feeds the black hole through a channel of inflow, or a possible clumpy in-falling flow. As I describe here and in the next section, my interpretation of these variable signals (which relates flux modulations mainly to lensing and boosting effects) can open a new window to study physics in very strong gravitational regimes, very close to the event horizon of black holes.

#### 4.1.1 Emission Mechanisms in Sgr A\* Revisited

NIR spectroscopy has shown that a power-law fit:

$$F_\nu \propto \nu^{-\alpha} \quad (4.1)$$

where  $F_\nu$ ,  $\nu$  and  $\alpha$  are the flux, frequency and spectral index respectively, can describe the observed spectrum of NIR flares. Although all the observations are in agreement with the fact that NIR flares show a soft spectrum ( $\alpha > 0$ ), the value of the spectral index is still not well determined. The first NIR spectroscopy observations in July 2004 (Eckart et al. 2004) proposed the  $\alpha$  value to be  $\sim 0.8 - 1.3$  during the peak of the flare. In 2006, Gillessen et al. (2006) observed a correlation between flux and spectral index in their observations. However, recent observations by Hornstein et al. (2007) are consistent with a constant spectral index,  $\alpha = 0.6 \pm 0.2$ .

The actual value of the spectral index shows its importance in the modelling of the physical process responsible for the flaring emission. Here I review the radiation model I will use in rest of the text mostly based on (Melia et al. 2001, Liu et al. 2006, Eckart et al. 2006a,b Yuan et al. 2007). The main idea behind all of them is that during flares a fraction of electrons near the event horizon of the black hole are accelerated. This can be described in the simplest form by a power law distribution in the energy of radiating

electrons:

$$N(\gamma) = N_0 \gamma^{-p} \quad (4.2)$$

where  $N(\gamma)$ ,  $N_0$ ,  $\gamma$  and  $p$  are the energy distribution function of electrons, normalizing constant, Lorentz factor of the electrons and the energy spectral index, respectively. For high values of  $\alpha$  one will need a sharp cut-off to the energy spectrum of electrons ( $\gamma_c$ ) while a lower value of  $\alpha$  ( $\alpha \sim 0.6$ ) allows for a relatively milder distribution in the energy of electrons. Liu et al. (2006) have shown that simultaneous NIR and X-ray spectral measurements can well constrain the parameters of the emitting region.

Before describing the details of my simulations, here I discuss how the existing observations limit the possible range of free parameters. Observationally it is proven that in the Sgr A\* spectrum there exists a turn-over frequency in the sub-millimeter to NIR range (the turn-over frequency is the frequency where the system changes its optical depth behavior). By using the turn-over frequency relation:

$$\nu_c = 2.8 \times 10^6 B \gamma_c^2 \text{ GHz} \quad (4.3)$$

one can put an upper limit on  $\gamma_c^2 B$ , where  $B$  is the magnetic field strength in Gauss. Here I have used  $\gamma_c = 100$  and  $B = 60\text{G}$  which give the best fit to the NIR/X-ray models that already exist (Liu et al. 2006; Eckart et al. 2008a).

In my simulations I first considered a scenario in which the main flare is caused by a local perturbation of intensity close to the marginally stable orbit (via magnetic reconnection, stochastic acceleration of electrons due to MHD waves, magneto rotational instabilities (MRI) etc.). These instabilities spread out and produce a temporary bright torus around the black hole. In this scenario, the mentioned variabilities are mainly due to relativistic flux modulations caused by the presence of an azimuthal asymmetry in the torus.

Simulations are dealing with two important velocities: radial ( $v_r$ ) and azimuthal ( $v_\phi$ ). The radial velocity can be parametrized in the following way:

$$v_r \sim \left( \frac{4\beta_P\beta_\nu}{9} \right) \left( \frac{GM}{r} \right)^{\frac{1}{2}} \quad (4.4)$$

which depends on the ratio of the stress to magnetic field energy density,  $\beta_\nu$ , and the ratio of the magnetic energy density to thermal pressure,  $\beta_P$  (Melia 2007). The use of the typical values of  $\beta_P$  and  $\beta_\nu$  from MHD simulations give us an estimation ( $\beta_P\beta_\nu \sim 0.05$ , Melia 2007). This leads to a radial velocity of the order of  $0.1 \left( \frac{r_g}{min} \right)$ . For azimuthal velocity, I assumed that above the marginally stable orbit plasma is in a Keplerian orbit

$$v_\phi = \left( \frac{r^2 - 2a\sqrt{r} + a^2}{\sqrt{\Delta}(r^{3/2} + a)} \right) \quad (4.5)$$

where  $\Delta = r^2 - 2r - a^2$ , and inside the plunging region matter experiences free fall with the same angular momentum as at the marginally stable orbit. More details about the dynamics of the accretion disk are presented in the next section.

Furthermore, two important time scales are at work: heating and cooling time scales. Heating time scale strongly depends on the physical processes which act as the engine of the whole event (MHD instabilities, magnetic reconnection etc.) and one can just put an observational constraint on that according to the averaged observed rise time of the events ( $\bar{t}_{rise} \sim 40\text{min}$ ). Cooling time is mainly controlled by the Keplerian shearing and synchrotron loss time:

$$t_{syn} = 5 \times 10^5 B^{-\frac{3}{2}} \nu^{-\frac{1}{2}} \text{ min}, \quad (4.6)$$

where  $B$  must be set in Gauss and  $\nu$  is in GHz.

In a differentially rotating accretion disk, a not confined emitting region will lose its cohesion via shear within a few orbital periods. For a synchrotron cooling time of only a few minutes at  $2.2 \mu\text{m}$ , which is significantly shorter than the time the emitting region has before disintegration because of shearing. This cooling time will determine the time scale within which the emitting spot will continue to exist in the absence of any occurring heating. Adopting  $B \sim 60\text{G}$  and  $\nu = 300 - 1600\text{GHz}$  as typical flare characteristics (see Eckart et al. 2006a, 2008a) we get a synchrotron cooling time of the order of 1 – 2 hours for the THz-peaked flare emission which matches a typical flare event length observed in K-band, and also the 2.5 hour time scale found at a wavelength of  $3\text{mm}$  by Mauerhan et al. (2005). At a wavelength of  $2.2\mu\text{m}$  I find a much shorter cooling time scale of  $t_{syn} \sim 4.3\text{minutes}$ .

Combining the cooling time scale with the synchrotron spectrum upper frequency expression and setting it equal to the observing frequency  $\nu$ , we get

$$t_{syn} \propto \nu^{-2}. \quad (4.7)$$

This shows that a source component that is bright in the  $L'$ -band ( $3.8\mu\text{m}$ ) will have a life time of  $\approx 13$  minutes, three times longer compared to a component seen in the K-band ( $2.2\mu\text{m}$ ). Since the upper frequency of the synchrotron spectrum is a strong function of the peak synchrotron cut-off frequency and the source size, any small alterations in these quantities will bring out a large change in the value of the upper synchrotron cut-off frequency and hence a significant alteration of the infrared flux density (and potentially the infrared spectral index; see Eckart et al. 2006a).

In a model by Schnittman (2005) emitting spots are created and destroyed around a single radius inside the accretion disk with random phases and exponentially distributed

lifetimes  $\tau$ , resulting in Lorentzian peaks in the power spectrum at the orbital frequency with a width of  $\Delta\nu=(4\pi\tau)^{-1}$ . The typical lifetimes of spots in this model are proportional to the orbital period  $T$  at their radius. From MHD calculations Schnittman et al. (2006) find over a large range of radii that disk perturbations indeed have a nearly exponential distribution of lifetimes, with  $\tau\sim 0.3T$ .

### 4.1.2 An Analytical Synchrotron Self-Compton Model

The observed NIR/X-ray properties of the Sgr A\* light curves raise a number of questions: Can we expect a sub-flare structure in the X-ray domain using a synchrotron self Compton model? What is the approximate flux distribution within a temporary accretion disk around Sgr A\*? This is also closely related to more general questions of how the observed light curve properties vary if the life time of the emitting regions, shearing and synchrotron cooling time scales are considered.

In contrast to the global solutions for the observed SED of Sgr A\*, here I limit my analysis to modeling the NIR to X-ray spectrum of the most compact source component at the location of Sgr A\*. My analysis is based on a simple SSC model describing the observed radio to X-ray properties of Sgr A\* using the nomenclature given by Gould (1979) and Marscher (1983). Inverse Compton scattering models provide an explanation for both the compact NIR and X-ray emission by up-scattering sub-mm-wavelength photons into these spectral domains. The models do not intend to explain the entire low frequency radio spectrum and IQ state X-ray emission. However, they give a description of the compact emission from Sgr A\* during low and high flux density flare periods. A more detailed explanation is also given by Eckart et al. (2004, 2006a).

I assume synchrotron sources with typical size  $R$ , of the order of a few Schwarzschild radii. The emitting sources become optically thick at a frequency  $\nu_m$  with a flux density  $F_m$ , and has an optically thin spectral index  $\alpha$  following the law  $F_\nu\propto\nu^{-\alpha}$ . The upper synchrotron cut-off frequency is  $\nu_2$ . This allows me to calculate the magnetic field strength  $B$  and the inverse Compton scattered flux density  $F_{SSC}$  as a function of the X-ray photon energy (Marscher 1983):

$$F_{SSC} \propto \ln\left(\frac{\nu_2}{\nu_m}\right) R^{-2(2\alpha+3)} \nu_m^{-(3\alpha+5)} F_m^{2(\alpha+2)} \nu^{-\alpha} . \quad (4.8)$$

The synchrotron self-Compton spectrum has the same spectral index as the synchrotron spectrum that is up-scattered i.e.  $F_{SSC}\propto\nu^{-\alpha}$  (see Marscher et al. 1983 for further details). I find that Lorentz factors  $\gamma$  for the emitting electrons of the order of typically  $10^3$  are required to produce a sufficient SSC flux in the observed X-ray domain. A

model	$\alpha$	$\theta$ $\mu\text{as}$	$S_m$ Jy	$\nu_m$ GHz
A	0.80	3.5	0.40	1100
	0.80	2.9	0.11	600
B	1.30	6.9	2.40	1200
	1.30	1.5	0.10	1100

**Table 4.1:** Input parameters for the synchrotron (A) and synchrotron self Compton models (B). Multi component models of the temporary accretion disk around Sgr A\* are calculated using component properties that are bracketed by these parameters.

possible relativistic bulk motion of the emitting source results in a Doppler boosting factor  $\delta = \Gamma^{-1}(1 - \beta \cos \phi)^{-1}$ . Here  $\phi$  is the angle of the velocity vector to the line of sight,  $\beta$  the velocity  $v$  in units of the speed of light  $c$ , and Lorentz factor  $\Gamma = (1 - \beta^2)^{-1/2}$  for the bulk motion. With *bulk motion* I mean the collective motion of the emitting material of an entire source component with respect to the observer, rather than the motions of the individual electrons. Relativistic bulk motion is not a necessity to produce sufficient SSC flux density, but I have used modest values for  $\Gamma = 1.2 - 2$  and  $\delta$  ranging between 1.3 and 2.0, representing a suitable coverage of the inclinations used in the models of the temporary accretion disk around Sgr A\*. Such values will also be relevant in cases of mild relativistic outflows - both of which are likely to be relevant to Sgr A\*.

With  $\gamma \sim 10^3$ , the upper synchrotron cut-off frequency  $\nu_2$  lies within or just shortward of the NIR bands such that a considerable part of the NIR spectrum can be explained by synchrotron emission, and the X-ray emission by inverse Compton emission. This is supported by SSC models presented by Markoff et al. (2001) and Yuan, Quataert & Narayan (2003) that result in a significant amount of direct synchrotron emission in the infrared (see also synchrotron models in Yuan, Quataert & Narayan 2004 and discussion in Eckart et al. 2004).

For this analytical multi-component model for the temporal accretion disk I combined the light amplification curves for individual orbiting spots and a simple SSC model. Thereby I obtained zero order time dependent flare characteristics from the NIR to the X-ray domain. I assume that the essential quantities of the SSC models, i.e. the turnover flux density  $F_m$ , frequency  $\nu_m$ , and the source size  $R$  of the individual source components, are distributed as power laws with the number distributions of flux

components within the temporal accretion disk

$$\mathcal{N}(F) \propto F_m^{\beta_F} \quad (4.9)$$

$$\mathcal{N}(\nu) \propto \nu_m^{\beta_\nu} \quad (4.10)$$

$$\mathcal{N}(R) \propto R^{\beta_R} \quad (4.11)$$

For example, if  $\beta_F = 0$ , the flux densities of the source components cover the full range between the minimum and maximum values. For  $\beta_F > 0$  and  $\beta_F < 0$  there is an increasing preference towards larger and lower flux density values, respectively. Similarly this is true for  $\beta_\nu$  and  $\beta_R$ .

With source components sizes of the order of  $1 - 2 r_g$  (Liu et al. 2006, Broderick and Loeb 2006, Meyer et al. 2006a,b) I can therefore safely assume that the accretion disk is well sampled using a total of  $\sim 10$  Gaussian shaped disk sections with random values of  $F_m$ ,  $\nu_m$  and  $R$  taken from the described power law distributions in order to model the entire accretion disk. As a simple - but still general - model I assumed the source components to be equally spaced along the circumference of a constant orbit. While orbiting, the flux density of each component will follow the achromatic magnification curves that can be calculated as a function of spin parameter  $a$ , inclination  $i$  and orbital radius (see e.g. Broderick and Loeb 2006, Meyer et al. 2006a,b). In addition, I infer a Gaussian shaped weight function with a FWHM of about 3 orbital periods, which resembles the observed flare lengths quite well.

Here no truncation at or just within the last stable orbit has been applied (note that this is not the case in a fully relativistic simulation due to the gravitational redshift close to the black hole; see e.g. Fig. 4.9). As a result I obtain NIR and X-ray light curves that are modulated corresponding to the random distribution of component flux densities as a function of the source component flux density  $\beta_F$  and the product  $R\nu_m^{5/4}$  (which is proportional to  $B^{-4}F_m^2$ ). For each pair of these quantities I calculated 100 random models and computed median values of a number of diagnostic quantities (Fig. 4.1). The quantity  $\mathcal{C}$  (second row in Fig. 4.1) is a measure of the flux modulation due to the presence of sub-flares during a single flare of the characteristic duration of about 100 minutes. I also calculate the NIR flux density weighted magnetic field strength times the contrast of the light curve modulation. I take this quantity  $\mathcal{FC}$  (field contrast, third row in Fig. 4.1) as a measure of detectable NIR polarized flare and sub-flare structures. Finally I show in Fig. 4.1 the NIR flux density and the corresponding synchrotron and SSC contributions. In detail the left and right hand panels show the results for a synchrotron (A) and a synchrotron self Compton model (B), respectively. For both models I list input parameters in Tab. 4.1. The first row ( $\alpha$ ) shows the  $\exp(-\chi^2/2)$  results, the second row panels ( $\beta$ ) show the sub-flare contrast, the third

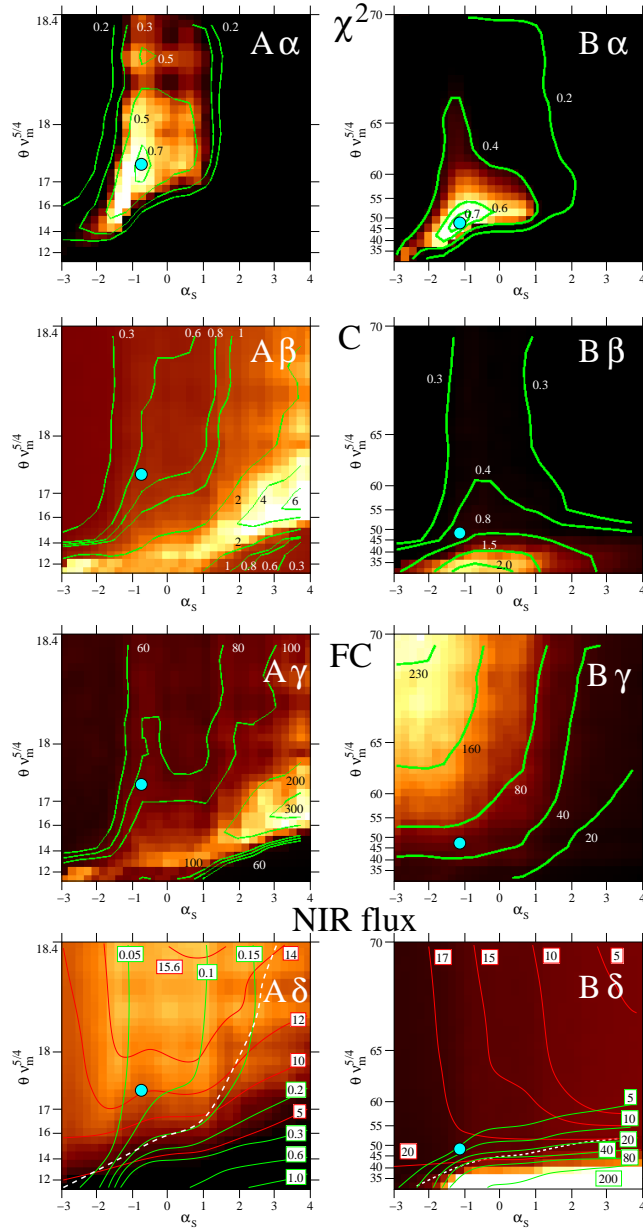


**Figure 4.1:** Diagnostic diagrams for two representative synchrotron models of the flare emission of Sgr A\* (figure from Eckart et al. 2008a).

row panels ( $\gamma$ ) show the NIR flux weighted magnetic field, and the last row ( $\delta$ ) the near-infrared emission. The red and green contour lines indicating the synchrotron

and SSC contribution in that wavelength range. The white dashed line indicates the median short wavelength cut-off of the synchrotron spectrum. Significant synchrotron contribution to the total NIR flux density occurs above this line. The blue filled circle in all panels indicates the location of the minimum  $\chi^2/2$ , i.e. maximum likelihood  $\mathcal{ML}=\exp(-\chi^2/2)$ .

In order to determine the agreement between the measurements and the predicted NIR and X-ray flux density and NIR contrast,  $\mathcal{C}$ , I perform a maximum likelihood ( $\mathcal{ML}$ ) analysis. As a  $\mathcal{ML}$  score I use

$$\log(\mathcal{ML}) = -\frac{\chi_{F_{NIR}}^2}{2} - \frac{\chi_{F_{X-ray}}^2}{2} - \frac{\chi_{FC}^2}{2} . \quad (4.12)$$

where  $\chi^2 = \frac{(F_{th}-F_{obs})^2}{\sigma^2}$ . For the sub-flare contrast  $\mathcal{C}$  I used a value of  $0.6\pm 0.3$  as derived from the May 2005 NIR data (Eckart et al. 2006b). In Fig. 4.1 I show selected diagnostic diagrams for two representative synchrotron models of the flare emission of Sgr A\*. The models are based on the input parameters of the high and low flux density cases listed in Tab. 4.1. These parameters represent the boundary values between which the component flux density, size and peak cut-off frequency follow a power law. I chose a spectral index of  $\alpha = 0.8$  for the synchrotron model (A) in order to be consistent with the constant infrared spectral index of  $\alpha = 0.6 \pm 0.2$  reported by Hornstein et al. (2007). For the SSC model (B) I have chosen a spectral index of  $\alpha = 1.3$  in order to obtain a significant contribution of SSC radiation in the NIR bands, which is impossible to achieve with flatter spectral indices for the given X-ray flare brightness. The SSC X-ray flux has the same distribution as the SSC NIR flux in the NIR flux panel in Fig. 4.1. For the synchrotron (A in Tab. 4.1) and SSC (B) cases, it is scaled down by a factor of  $\sim 1.4$  and  $\sim 110$ , respectively.

The claimed quasi-periodicity of the NIR light curves indicates that the spin value  $a \geq 0.5$  (Genzel et al. 2003, Eckart et al. 2004, Meyer et al. 2006a,b). I calculated the data shown in Fig. 4.1 using an inclination of  $i=70^\circ$  (Eckart et al. 2006b, see also Meyer et al. 2006ab) and obtained  $\chi^2 > 0.9$  and similar values for  $i \geq 70^\circ$ . For  $a \rightarrow 1.0$  or  $i \rightarrow 0^\circ$  the best  $\chi^2$  value drops to 0.6 and 0.3 and its location in the panels shown in Fig. 4.1 moves to the lower left.

An important result of the simulations is that the observed total NIR and X-ray flux densities can successfully be modeled simultaneously with the observed sub-flare contrast. In addition, the best fits to the NIR and X-ray flux densities lie within or close to regions of high NIR flux density weighted magnetic field strength. This demonstrates that the combination of the SSC modeling and the idea of a temporary accretion disk can realistically describe the observed NIR polarized flares that occur synchronous with

the 2-8 keV X-ray flares. I also find that the exponential  $\beta_F$  of the assumed power law distribution for the synchrotron peak flux  $F_m$  results in the best models in values around  $\beta_F = -1 \pm 1$ . A value of  $\beta_F = 0$  (which is included) represents scenarios in which source components cover the entire range of flux densities with an equal probability for each value, rather being biased towards similarly faint or bright components. This provides high sub-flare contrast values. An exponent of  $\beta_F = -1$  favors lower flux density values. In the SSC model (B) high contrast is provided by the SSC contribution to the NIR spectral range also allowing for  $\chi^2$ -fits at lower flux density weighted magnetic field strengths around 30 G rather than 60 G as for the synchrotron model (A). These magnetic fields are comparable to the range of field strengths of the order of 0.3 Gauss to about 40 Gauss, that have been previously reported (Eckart et al. 2004, Eckart et al. 2006ab). The fields are also within the range expected for RIAF models (e.g. Markoff et al. 2001, Yuan, Quataert, Narayan 2003, 2004), and well above the minimum value required to have the cooling time of the flare less than the duration of the flare (Yuan, Quataert, Narayan 2003, 2004, Quataert 2003).

## 4.2 Numerical Simulations of an Accretion Flow

### 4.2.1 Dynamics: The Polish Doughnut

Since we still lack the knowledge of several significant characteristics of accretion processes, it is still not possible to simulate accretion flow models that are physically steady from first principles, without the use of some ad hoc assumptions or simply neglecting important processes. As a result, the hydrodynamical simulations (which use the ad hoc constant viscosity prescription for example) or the nowadays MHD simulations (which e.g. neglect radiative transfer) could not be considered sufficient. So I follow the analytic models of black hole accretion invented by Qian et al. (2009) to simulate the dynamics of the inner parts of the accretion disk.

In practice it is far easier to guess and work with the specific angular momentum and entropy being functions of  $r$  and  $\theta$ . One can guess a certain form of these functions for different models. For instance, two of these models which have brought a great deal to the understanding of the physics of black-hole accretion; the *Shakura-Sunyaev* thin disk model that assumes the angular momentum distribution to be Keplerian,

$$L(r, \theta) = L_K(r) \equiv \frac{M^{1/2} (r^2 - 2aM^{1/2}r^{1/2} + a^2)}{r^{3/2} - 2Mr^{1/2} + aM^{1/2}}, \quad (4.13)$$

and the *cold-disk-hot-corona* model that postulates a flat disk of low entropy surrounded by a spherical corona of high entropy.

However, a simpler mathematical assumption for the distribution of the angular momentum and entropy is that both of these functions remain constant. This postulate was used in Warsaw by Paczynski and his team in order to present what is known as the *Polish doughnut* model. A thick-disk model with a characteristic toroidal shape, like a doughnut.

Such Polish doughnuts have been useful in many studies, such as semi-analytic astrophysical appearance studies of super-Eddington accretion, and in analytic computations of small-amplitude fluctuations of accretion structures related to QPOs. The model can give out many of the features of the numerical results, e.g. the locations of the cusp and pressure maximum, and also the vertical thickness of the disk, if one chooses the correct parameters. So far all that can be achieved is qualitative agreements.

For the distribution of angular momentum in my simulations, I have adopted their study as an ansatz which resulted in confining it to the equatorial plane of the accretion disk, in other words a slim-disk scenario. The distribution now is of the following form:

$$L(r, \pi/2) = \begin{cases} L_0 \left( \frac{L_K(r)}{L_0} \right)^\beta & \text{for } r \geq r_{ms} \\ L_{ms} & \text{for } r < r_{ms} \end{cases} \quad (4.14)$$

where,  $L_K(r)$  is a Keplerian angular momentum. As it can be seen, for  $\beta = 0$  the angular momentum will be constant  $L = L_0$  and for  $\beta = 1$  it will be equal to the Keplerian one  $L = L_K$ . For radii larger than  $r_{ms}$  the angular momentum  $L(r)$  is smaller than  $L_K(r)$  (Keplerian). Below  $r_{ms}$  it is constant. For radius larger than  $r_{ms}$ , the matter is orbiting on constant radii in the disk while for smaller it is falling with constant energy and angular momentum.

In figures 4.2 and 4.3 I show the angular momentum distribution and orbital time scale, for a test particle on the equatorial plane, as functions of the distance to the black hole for different parameter sets of  $\beta$  and the black hole spin.

### 4.2.2 General Relativistic Transfer Effects

Since all these physical processes happen very close to the black hole and in a very strong gravitational regime, we must take into account the effects of curved space-time. The importance of the general relativistic effects on the spectra of the accreting

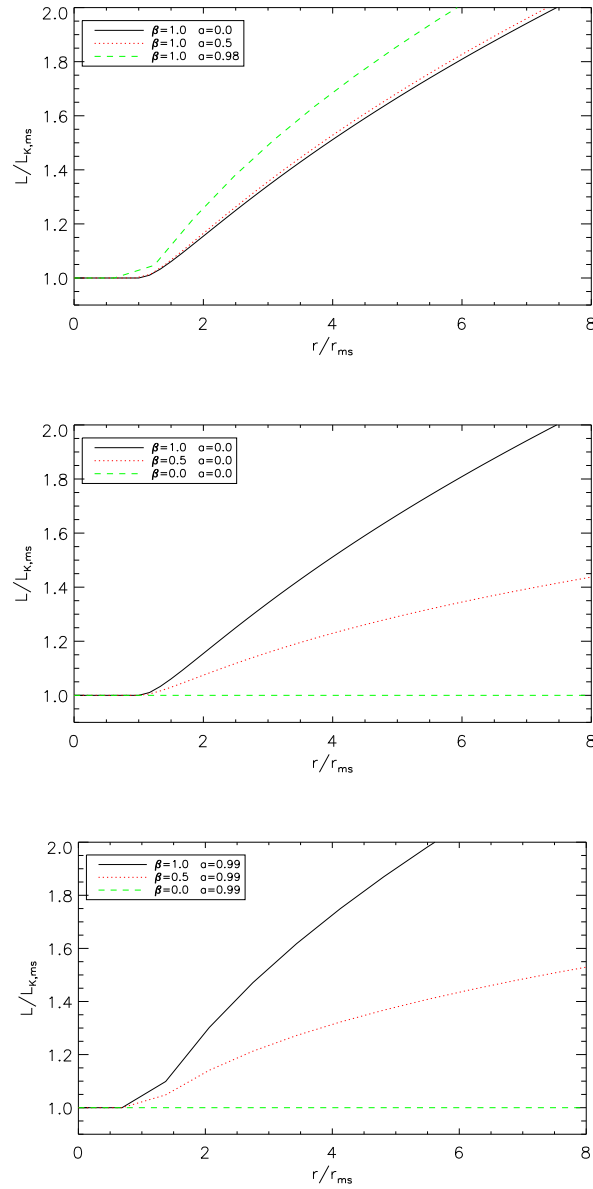


**Figure 4.2:** Distribution of angular momentum on the equatorial plane of the accretion disk for different sets of the mentioned parameters. In each panel different curves correspond to the different values of the spin of the black hole (top),  $\beta$  for a Schwarzschild (middle) and extremely spinning black hole ( $a = 0.99$ , bottom).

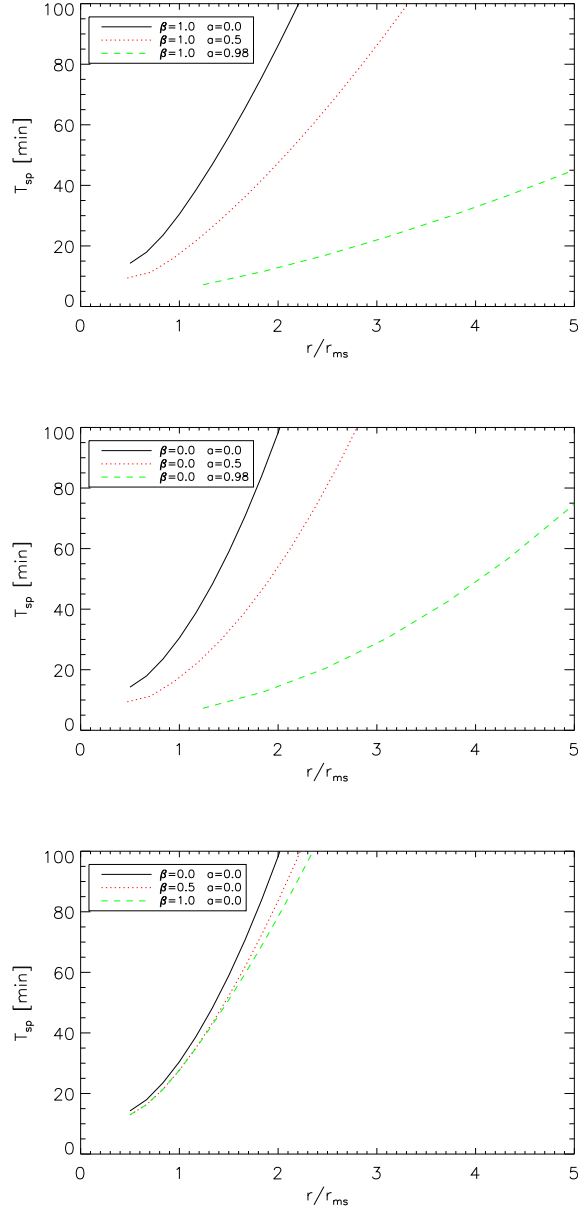


**Figure 4.3:** Orbital time scale on the equatorial plane of the accretion disk for different sets of parameters. In each panel different curves correspond to the different values of the spin of the black hole (top),  $\beta$  for a Schwarzschild (middle) and extremally spinning black hole ( $a = 0.99$ , bottom).

black holes first appeared in a paper by Cunningham (1973). He studied the effects of gravitational and Doppler shifts, plus the gravitational lensing effects for the radiation from an optically thick geometrically thin accretion disk. He packaged all the effects by introducing the concept of the transfer functions to go from the local emissivity to the observer at infinity. Since then numerous authors studied the strong gravity effects on the emission of the accretion disks of relativistic outflows (Connors, Piran & Stark 1980; Asaoka 1989, Kojima 1991; Laor 1991; Karas, Vokrouhlicky & Polnarev 1992; Viergutz 1993; Matt, Fabian & Ross 1993; Bao, Hadrava & Ostgaard 1994; Hameury, Marck & Pelat 1994; Zakharov 1994; Bao et al. 1997; Bromley, Chen & Miller 1997; Martocchia, Karas & Matt 2000; Beckwith & Done 2004).

To simulate the changes in paths and polarization properties of photons from the emitting electrons to the observer at infinity, I have used the KY ray-tracing code (Karas et al. 1992; Dovčiak et al. 2004). KY is able to calculate all the effects of GR, like light bending and changes in the emission angle, changes in the polarization angle of photons, gravitational lensing and red-shift, Doppler boosting (since matter inside the accretion disk is in orbit) and frame dragging (in case of Kerr black holes) in a thin disk approximation. In the geometrical optics approximation, photons follow null geodesics and their propagation is not affected by spin-spin interaction with a rotating BH (Mashoon 1973). This means that wave fronts do not depend on the photon polarization, and so the ray tracing through the curved space-time is adequate to determine the observed signals. Since my analysis is focused on high frequency regimes, I have mainly ignored radiative transfer effects. In the most general case, the propagation of light through the plasma inside the accretion disk influenced the light rays and the light rays are not any more the null geodesics. However, these plasma effects are mostly important for the longer wavelengths and can be neglected for higher frequencies (in my case NIR and X-ray photons).

To make KY work, we must initialize the properties of radiated photons at each point of the emitting region. The straightforward way is to define the intrinsic emission of each point in the context of the Stokes parameters. For the flux densities (mJy) and source sizes ( $\mu\text{as}$ ) of Sgr A\*, optically thick synchrotron emission in the NIR can safely be disregarded (see discussion in Eckart et al. 2009). Since in this report I focus only on the modeling of NIR flares, it is sufficient to pick up a model for the energy distribution of non-thermal electrons, radiating in an optically thin regime:

$$N(\gamma) = \begin{cases} N_0 \gamma^{-p} & \gamma \leq \gamma_c \\ 0 & \gamma > \gamma_c \end{cases} \quad (4.15)$$

which leads to the formulae for polarized emission:

$$I_\nu \propto n (B \sin \theta_e)^{\left(\frac{p+1}{2}\right)} \nu^{-\left(\frac{p-1}{2}\right)} \quad (4.16)$$

$$Q_\nu = \Pi_L \cos(2\chi_e) I_\nu \quad (4.17)$$

$$U_\nu = \Pi_L \sin(2\chi_e) I_\nu \quad (4.18)$$

$$V_\nu = \Pi_C I_\nu \quad (4.19)$$

where  $n$ ,  $\chi_e$ ,  $\Pi_L$  and  $\Pi_C$  are number density of the electrons, the angle between a reference direction and the plane of an observer co-moving with the disk frame and degree of linear and circular polarization, respectively. Throughout this thesis I assume that in the NIR regime the light is not circularly polarized ( $\Pi_C = 0$ ).  $I_\nu$ ,  $Q_\nu$ ,  $U_\nu$ , and  $V_\nu$  represent the Stokes parameters.  $\theta_e$  is the angle between the direction of the magnetic field and the direction toward the co-moving observer.

$$\theta_e = \theta_e(\eta, \psi, \phi_e, \delta_e) = \arccos\left(\sqrt{\frac{(\mathcal{B}^\alpha \kappa_{e\alpha})^2}{(\kappa_e^\beta \kappa_{e\beta})(\mathcal{B}^\gamma \mathcal{B}_\gamma)}}\right) \quad (4.20)$$

where I have picked the disk co-moving frame as the reference, so that the normal to the disk,  $\hat{n}$ , coincides with the  $\hat{z}$  direction. In this frame, the geometrical orientation of the global magnetic field vector ( $\mathcal{B}$ ) dominant component can be defined with a set of angles  $[\eta, \psi]$  ( $0 \leq \eta \leq \pi$ ,  $0 \leq \psi \leq 2\pi$ , see Fig. 4.4).  $\delta_e$  is the angle between the direction of the photon momentum ( $\kappa$ ) and the normal to the disk ( $\hat{n}$ ):

$$\delta_e = \arccos\left(-\frac{\kappa_{e\alpha} n^\alpha}{\kappa_{e\beta} v^\beta}\right) \quad (4.21)$$

where  $v$  is the four-velocity of matter in the disk.  $\phi_e$  is the azimuthal emission angle, defined as the angle between the projection of the three momentum of the emitted photon into the equatorial plane and the radial tetrad vector:

$$\phi_e = \arctan\left(\frac{\kappa_e^\alpha \hat{e}_{(\phi)\alpha}}{\kappa_e^\mu \hat{e}_{(r)\mu}}\right) \quad (4.22)$$

The combined gravitational and Doppler shift (g-factor) is defined as the ratio of the energy of a photon received by an observer at infinity to the local energy of the same photon when emitted from an accretion disc

$$g = \frac{\nu_o}{\nu_e} = \frac{\kappa_{ot}}{\kappa_{e\beta} v^\beta} \quad (4.23)$$

Here  $\nu_o$  and  $\nu_e$  denote the frequency of the observed and emitted photons, respectively.

By using this formalism I can calculate the transfer functions with high accuracy, even when it is very close to the black hole horizon. Some transfer functions depend on the matter's motion in the disk, which was defined to follow the terminology I gave earlier for the dynamics of the inner parts of an accretion disk. Approximately  $10^5$  geodesics have been used in numerical simulations, where they have covered the disk (with decreasing covering density) from the horizon to an outer radius  $r_{out} \sim 1000$ . As a result, transfer functions values were derived from a non-regular grid over the disk's region which were then interpolated using Delaunay triangulation to a regular grid in the coordinates  $r$  and  $\phi$ . Figure 4.5 shows a geometrical representation of the transfer functions.

There are two global parameters which affects the transfer functions: black hole dimensionless angular momentum,  $0 < a < 1$ , and observer inclination angle,  $0^\circ < i < 90^\circ$ . A non-rotating Schwarzschild black hole has  $a = 0$ , while extremely rotating Kerr black hole has  $a = 1$ ; observer located along the rotation axis (pole-on) has inclination  $i = 0^\circ$ , while equatorial (edge-on) observer has  $i = 90^\circ$ .

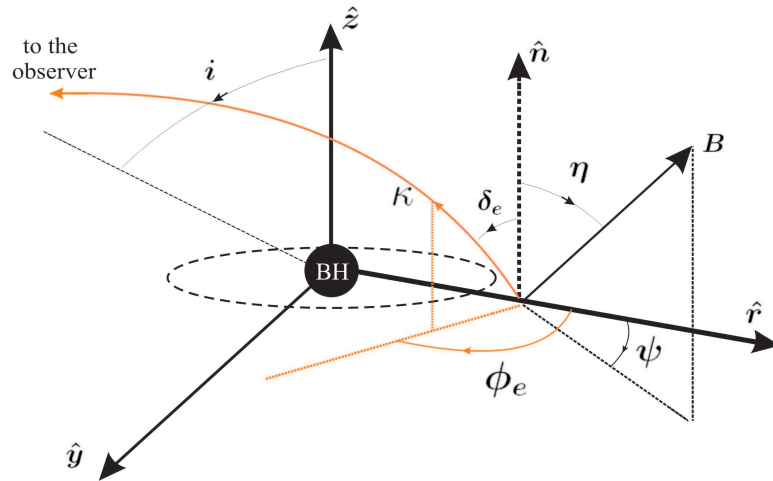


**Figure 4.4:** The geometry I considered in my emission model. The accretion disk around the black hole lies on the  $\hat{y} - \hat{r}$  plane and  $\hat{n}$  is the normal to the disk. The direction of the magnetic field lines ( $B$ ) corresponding to the disk frame is defined by two angles  $\eta$  and  $\psi$ .  $\kappa$  represents the momentum of the emitted photon and its direction determined by a set of angles  $[\delta_e, \phi_e]$ . The distant observer is looking to the system along a line of sight inclined by a certain angle  $i$ .

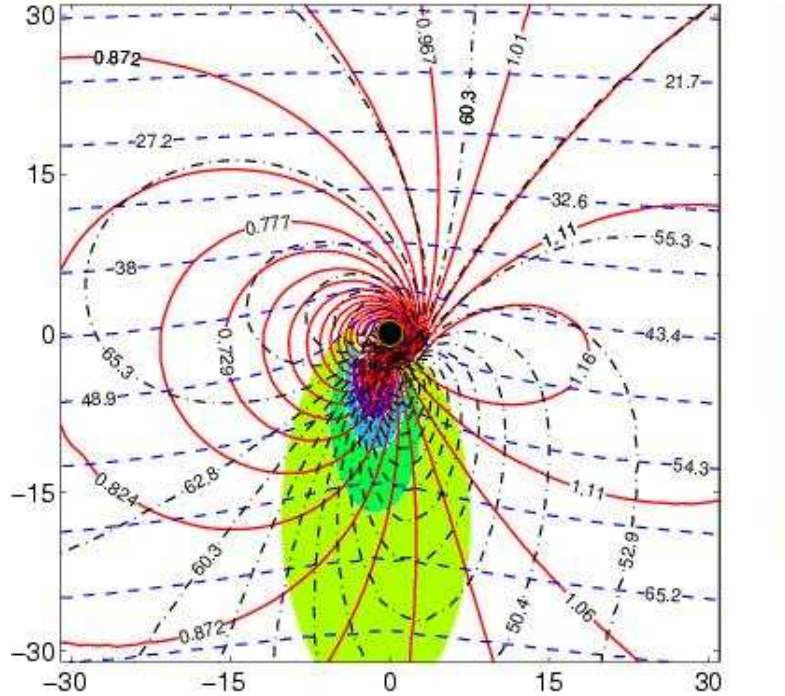


**Figure 4.5:** Content of data tables is illustrated by this plot, showing contour levels of various quantities. The equatorial plane of a Kerr black hole is considered (the view along rotation axis). Observer is located towards top of the figure with inclination of  $60^\circ$ . See text for details (credit: M. Dovciak).

The content of these transfer functions are illustrated for a set of parameter values in figure 4.5. It shows an equatorial plane view along a rotation axis with the use of Schwarzschild coordinates (units of  $M$ ). The observer is located at spatial infinity on top of the figure. The black circle in the center refers to the black hole, while the inner and outer circles are the photon circular orbit and the innermost stable orbit (co-rotating), respectively. These radii are identical when we have an extremely rotating black hole. We have four sets of contour lines (corresponding to four data tables):

#### 1. Solid red curves

They correspond to levels of redshift function. When the values are greater than unity, they represent a shift towards higher values for the energy and the observed flux. Doppler effect and gravitational redshift have an effect here, the latter especially near the horizon. In the case of neglecting the relativistic effects, symmetry with respect to the vertical axis would prevail (butterfly-shaped curves).

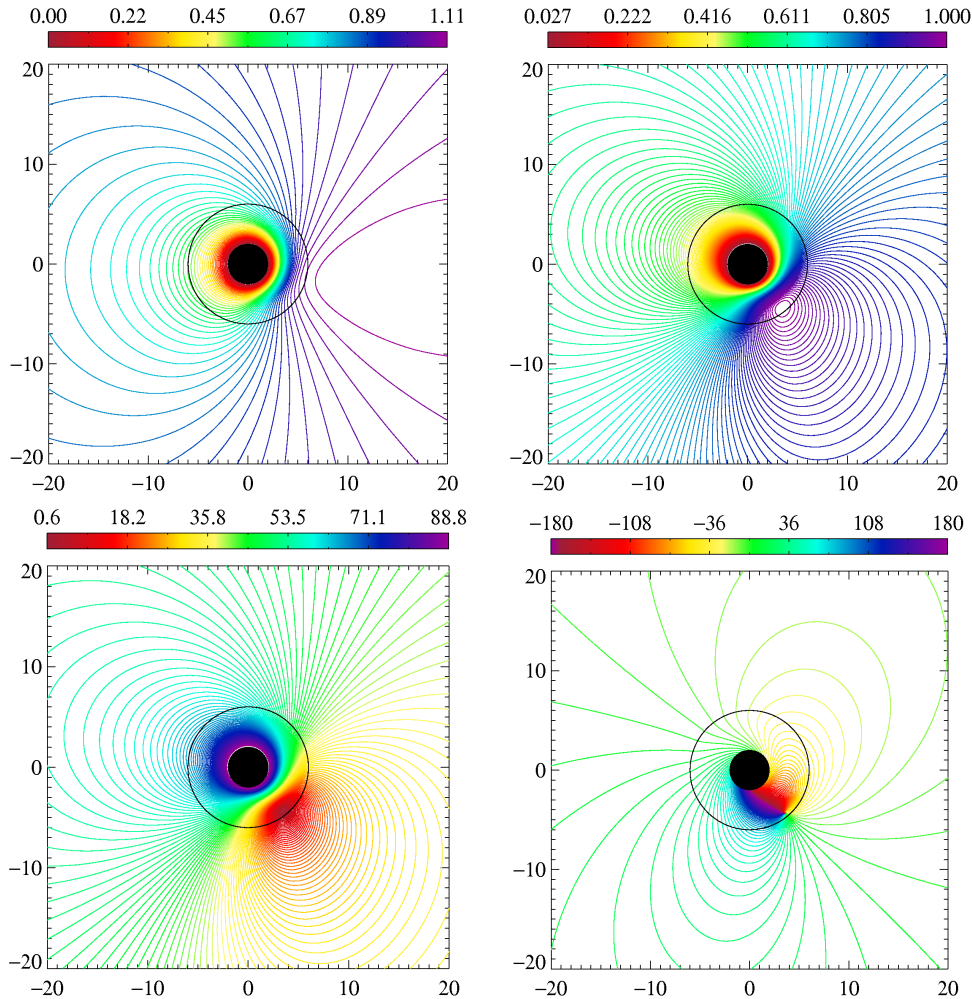


**Figure 4.6:** Contour levels of  $g$ -factor (top left),  $\cos(\delta_e)$  (top right),  $\phi_e$  (bottom left) and the change of polarization angle (bottom right) for a Schwarzschild black hole while the observer is located towards top of the figure with an inclination of  $45^\circ$ . See text for details (credit: M. Dovciak).

## 2. Dashed blue lines

They show levels of constant time delay. In neglecting relativistic effects the lines would be perfectly horizontal. The values here are in geometric units and scaled with the mass of the black hole.

## 3. Dash-dotted black curves

They show levels of constant emission angle with respect to the normal to the

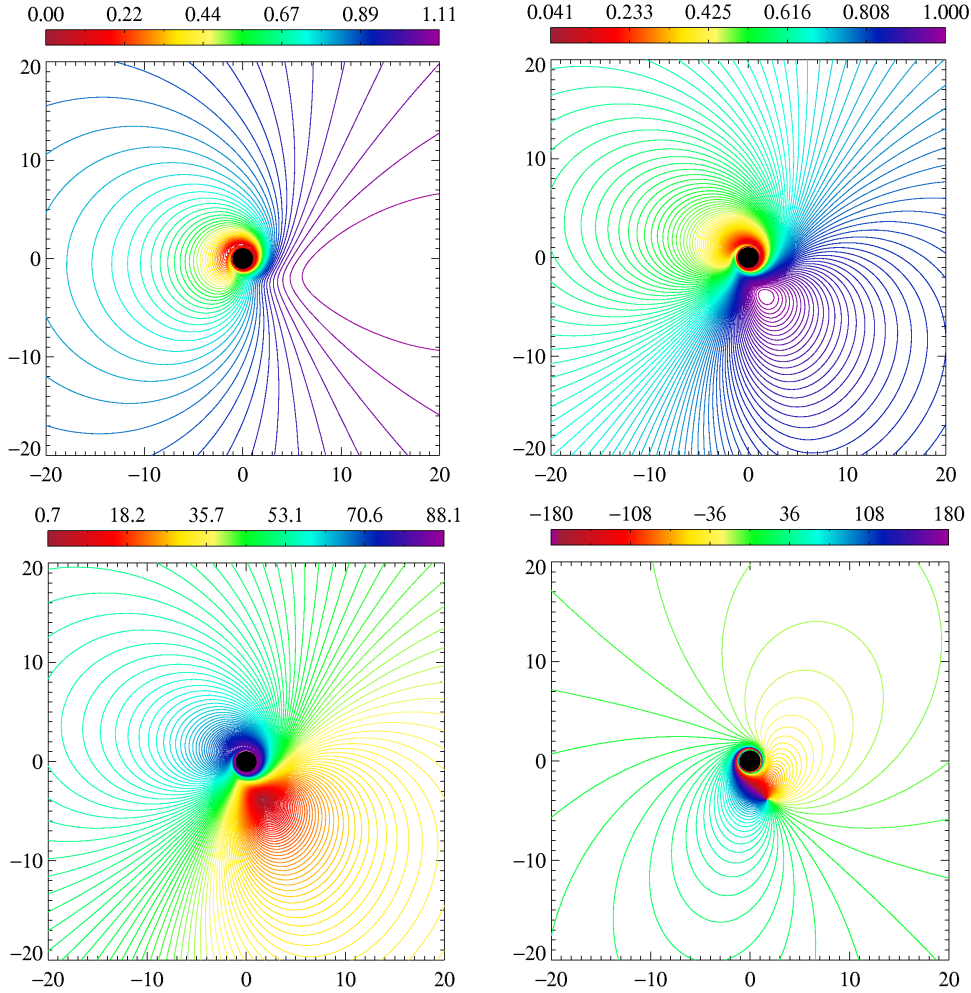


*Figure 4.7:* Same as Fig. 4.6 but for an extremal spinning black hole ( $a = 0.99$ ) (credit: M. Dovciak).

plane of the disk, in a co-rotating frame with the disk material. The values of the emission angles are determined by aberration and lensing effects; when they are far from the black hole they have the same value as the observer's inclination. In the case of anisotropic emissivity the local emission angle should be taken into account.

#### 4. Solid magenta curves

They represent levels of constant magnification (lensing effect). They were obtained by integrating the geodesic deviation equation that determines the change

in the cross-sectional area between adjacent light rays (at infinity they are parallel to each other, giving then a zero change in area in case of flat space). A significant effect occurs only, even with black hole geometry, for light rays originating near behind it (i.e. the place of upper conjunction for the observer,  $r < 15M$ ) and also when the observer is located close to the equatorial plane (large inclination,  $i > 60^\circ$ ). The values approach  $\cos(i)$  asymptotically when it is far from the black hole, which in the euclidean geometry correspond to simple effects of geometrical projection (without lensing); larger values show light enhancement from the corresponding disk region.

The contours of each function are shown in separate figures (Figs. 4.6 and 4.7) for a better representation. They show a top view of the black hole's equatorial plane with an observer inclination of  $45^\circ$  with respect to the normal of the plane. I used the graphical presentation for a practical and quick way to estimate the order-of-magnitude, even though they are not really important for the process of calculations and actual data fitting. Expected values of various quantities can be obtained almost immediately most of the times. For instance one can estimate from these graphs, taking into account only the light emitting region basic parameters, the magnitude and range of the energy shift, the importance of the relative time delay, the effect of gravitational lensing etc. Dovciak et al. 2004a,b explain in details the KY code and the ray-tracing in the Kerr metric.

The images that are expected to be observed, for different possible inclinations with respect to the black hole/accretion disk system, can be simulated by fixing free parameters such as the emitting electrons spatial density distribution, the magnetic field strength and its global configuration, and the flux spectral index (e.g. see Fig. 4.9). In the next section I will show how compact azimuthal anomalies inside a uniform density distribution of the emitting plasma can reproduce the observed behavior of Sgr A\* in high frequency regimes.

### 4.2.3 Fully Relativistic Simulations of the Accretion Flow Into Sgr A\*

The synchrotron cooling time at NIR frequencies is only of the order of a few minutes, which is significantly shorter than the time scale of the observed flares. One way that a spot can survive long enough to be responsible for the observed  $\sim 4 - 5$  time flux modulations is that a SSC mechanism up-scatters the sub-mm seed photons to the NIR and X-ray frequencies (Eckart et al. 2006a-c, 2008a). The other possibility is that the heating time of orbiting NIR component is related to the rise time of the main flare,  $\tau \propto t_{rise}$  where the emissivity profile of the emitting component follows  $F(t; t_0, \tau) = F_0 \exp(-(t - t_0)^2/2\tau^2)$ .

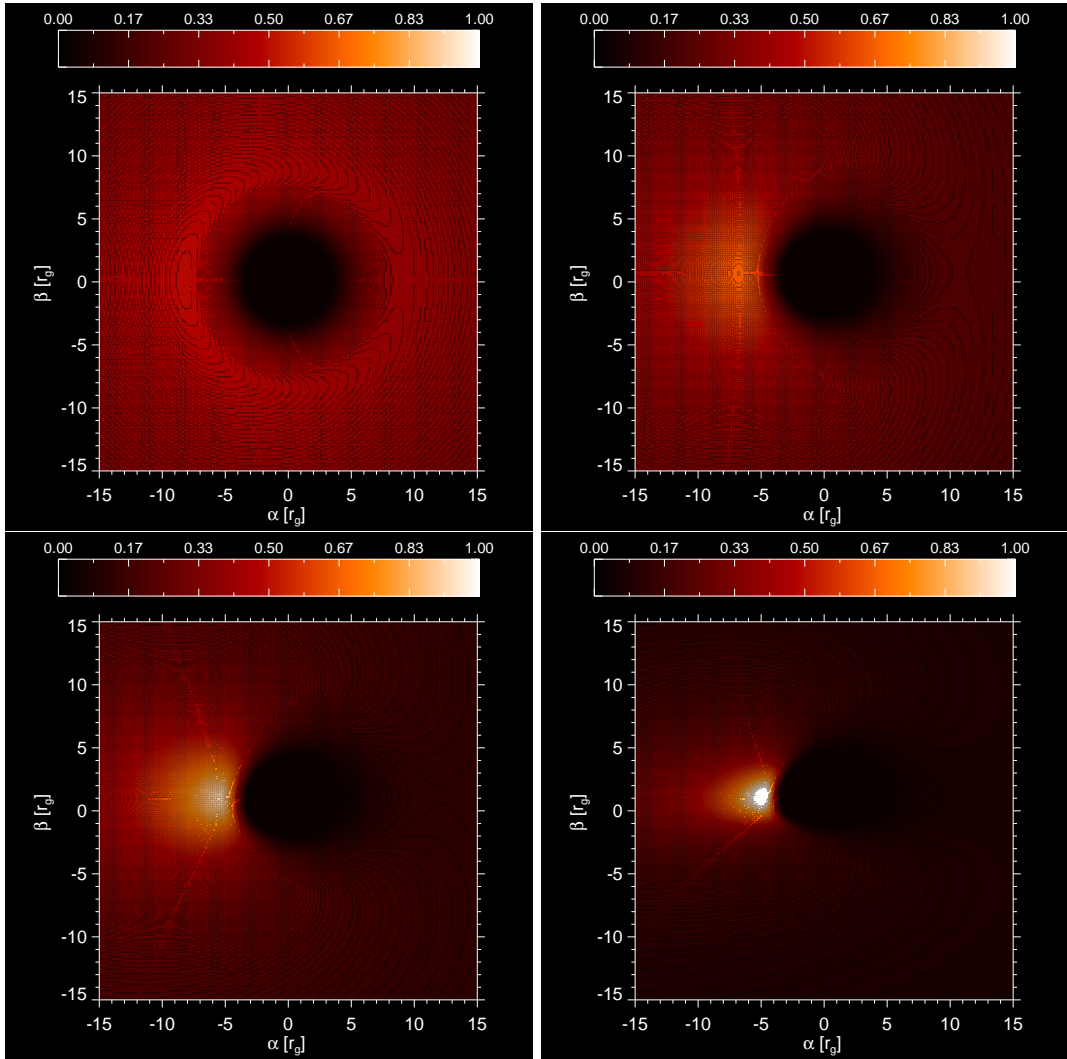


**Figure 4.8:** Images of an optically thick standard accretion disk around a Kerr black hole ( $a = 0.5$ ). The observer's inclination is  $5^\circ$  (top left),  $25^\circ$  (top right),  $45^\circ$  (bottom left) and  $65^\circ$  (bottom right).

The above discussion demonstrates that it is essential to consider the gravitational shearing time scale as a variable in the simulations. I have implemented this effect in my modelling by introducing a dimensionless characteristic shearing time scale:

$$\tau_{sh} = \frac{T(r_{spot})}{T(r_{spot} + r_0) - T(r_{spot} - r_0)} \quad (4.24)$$

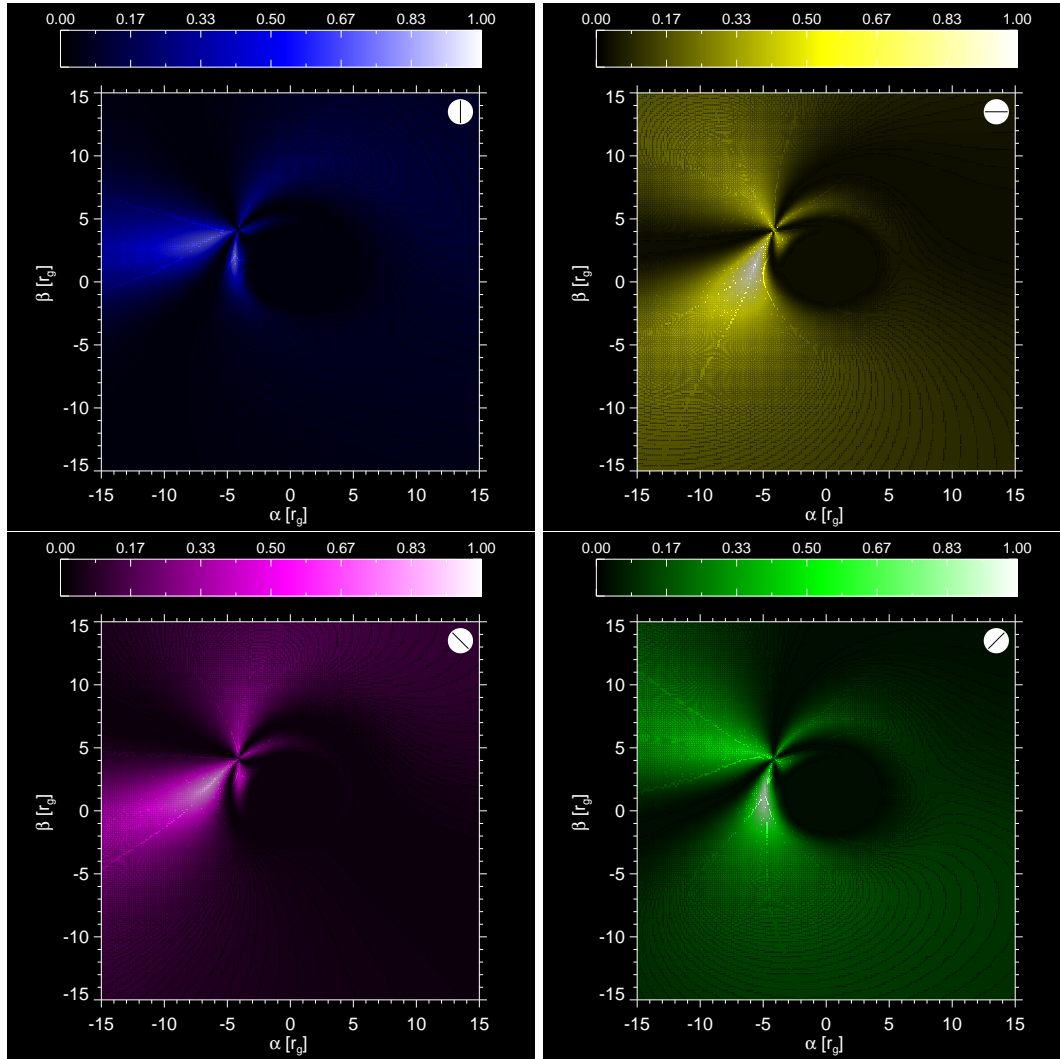


**Figure 4.9:** Images of an optically thick standard accretion disk around a Kerr black hole ( $a = 0.5$ ). The images were obtained in different polarization channels:  $0^\circ$  channel (top left),  $90^\circ$  channel (top right),  $45^\circ$  channel (bottom left) and  $135^\circ$  channel (bottom right). The observer's inclination is  $50^\circ$ .

where for the initial spatial distribution of the relativistic electrons I have used a spherical Gaussian distribution with its maximum being located at the radius  $r = r_{spot}$  with FWHM of  $r_0 = 1r_s$ . In my simulations,  $\tau_{sh}$  varies between  $\infty$  and 0.8.  $\tau_{sh} = \infty$  corresponds to the situation in which the spot preserves its shape for a long time. The mechanism that stabilizes the spot is not known, although several possibilities have

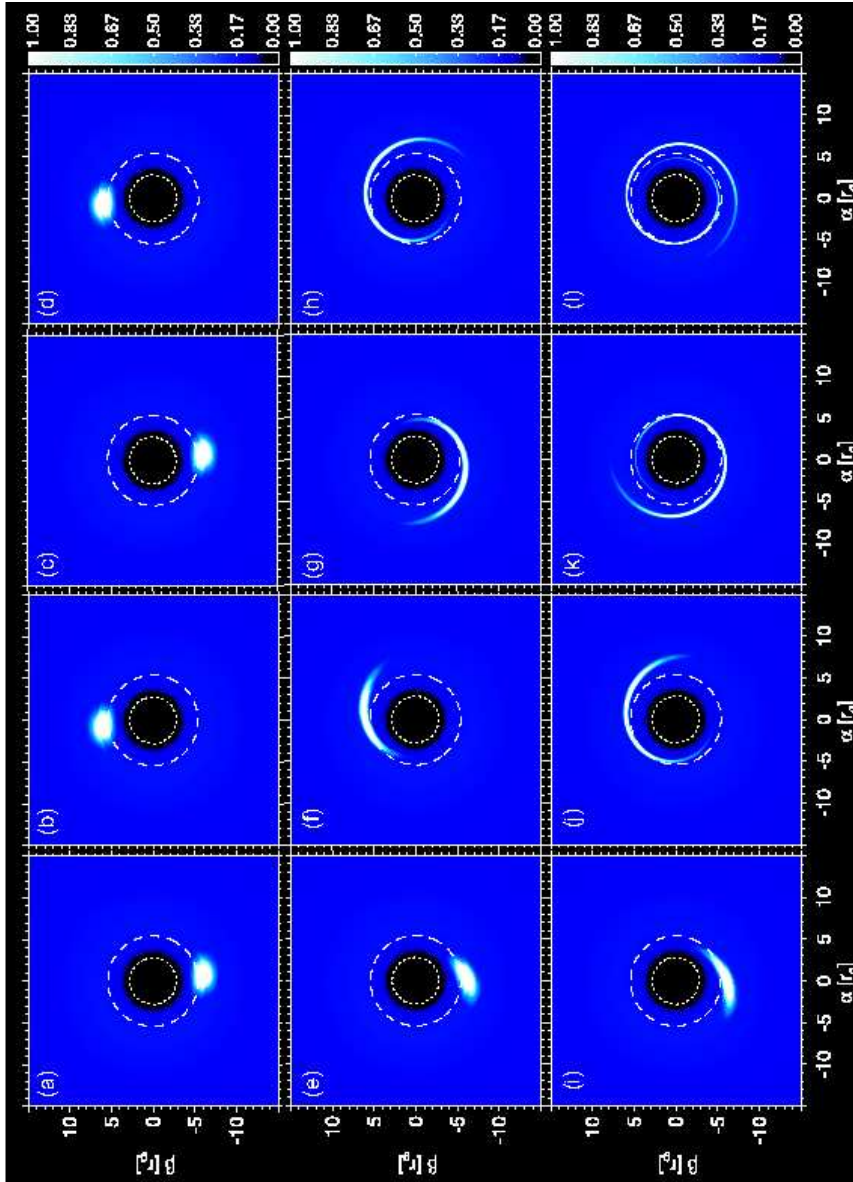


**Figure 4.10:** Snapshots of orbiting anomalies inside the accretion disk as they appear to a distant observer looking along a line of sight inclined by  $0^\circ$  (relative to the normal to the disk), at times after  $\frac{1}{4}T$ ,  $\frac{3}{4}T$ ,  $\frac{5}{4}T$  and  $\frac{7}{4}T$  (left to right). Each row shows how the event evolves in time for different values of the characteristic shearing time scale:  $\tau_{sh} = \infty$  (a-d),  $\tau_{sh} = 2.0$  (e-h) and  $\tau_{sh} = 1.0$  (i-l). The spin of the black hole is set to 0.5. The dotted and dashed lines indicate the position of the event horizon and marginally stable orbit, respectively. Each row has been scaled by its maximum intensity for illustrative purposes.  $\alpha$  and  $\beta$  are the projections of the impact parameter of the emitted photons as the coordinates on the sky of the observer. Both coordinates are labeled in  $r_g$  ( $\simeq 5\mu\text{as}$ ) units.

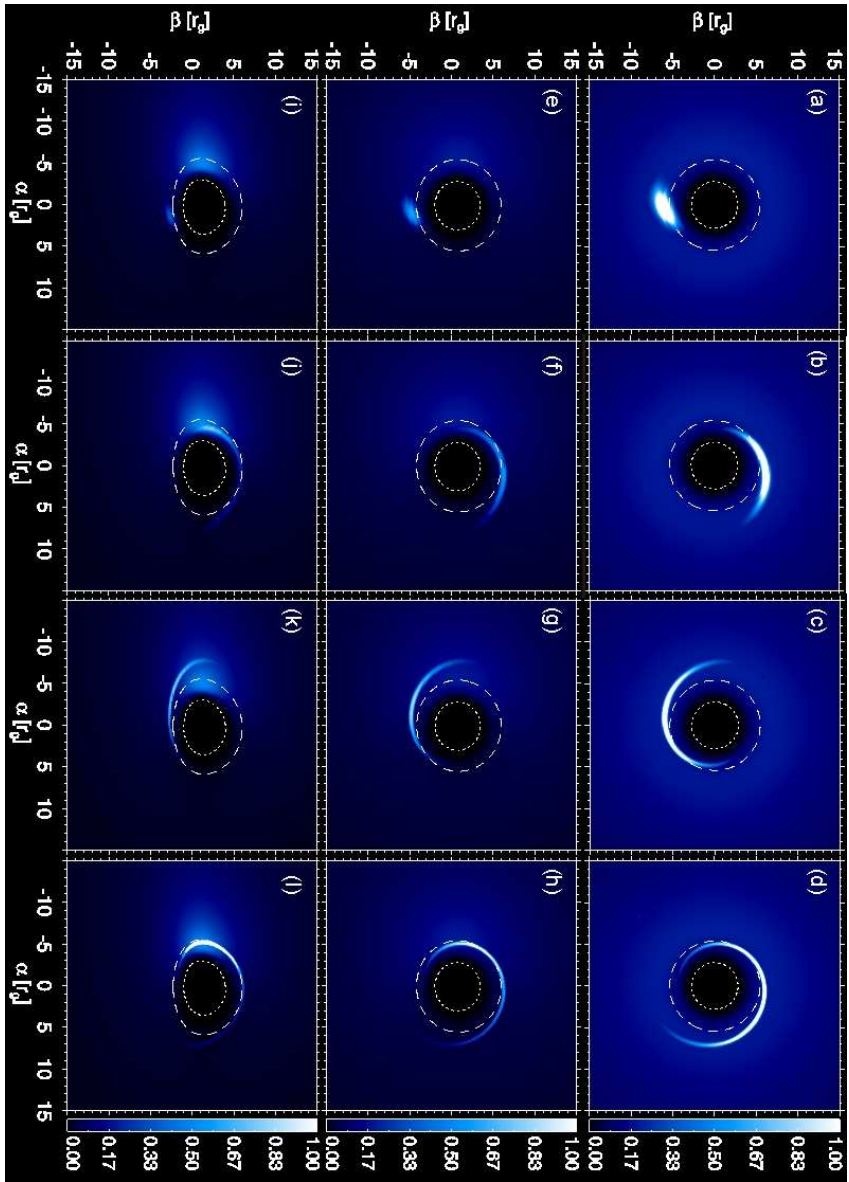


*Figure 4.11: Snapshots of an orbiting inside the accretion disk as it appears to a distant observer looking along a line of sight inclined by  $0^\circ$  (a-d),  $30^\circ$  (e-h) and  $60^\circ$  (i-l) (relative to the normal to the disk) at times after  $\frac{1}{4}T$ ,  $\frac{3}{4}T$ ,  $\frac{5}{4}T$  and  $\frac{1}{4}T$  (left to right). See also caption of Fig. 4.10.*

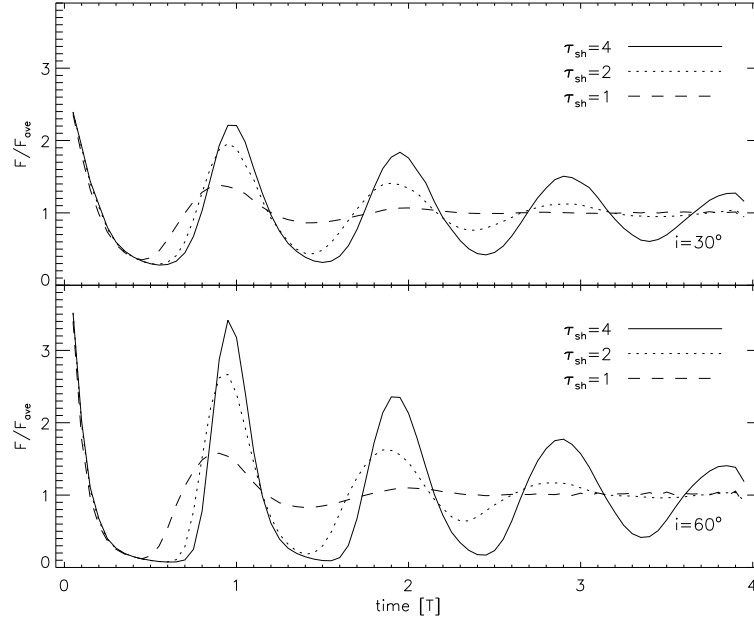


**Figure 4.12:** Flux modulations of an evolving perturbation close to the marginally stable orbit of a Kerr black hole with spin parameter of 0.5. The light curves show how different values of shearing parameter and inclination affects the resultant light curve.

been proposed and explored in the literature. In particular, the existence of persistent vortices on accretion disks has been explored (Abramowicz et al. 1992; Adams & Watkins 1995). However, my modeling suggests that shearing effects are indeed important, and can be well represented within the multi-component scheme or in the spiral pattern scheme generalizing the original spot scenario. The  $\tau_{sh} = 0.8$  corresponds to a pure Keplerian shearing for a spot located at the marginally stable orbit of an extremal spinning black hole ( $a = 1$ ). One must note that MHD simulations are unable to produce hot spots with long life-times comparable to the observed flare time scales (Hawley et al. 2001, Krolik et al. 2002). Schnittman et al. (2006) used a model for creation and annihilation of spots with short life times, distributed by random phase within a belt close to the marginally stable orbit. They show that their model can resemble the observed quasi-periodicity in the X-ray light curves. Eckart et al. (2008a) successfully modeled the simultaneous NIR/X-ray flares of Sgr A\* by following the same basic idea of a multi-component model. As mentioned before, following the results of Pecháček et al. (2008) these kind of multi-component models are able to reproduce the red noise behavior of PSDs, while some bright individuals can show their signatures in polarized light (see Fig. 4.18 and also discussion in Eckart et al. 2008a).

Fig. 4.10 shows how a hot spot is created and evolves in time for three different values of  $\tau_{sh}$ . A comparison between the rows shows how pure Keplerian shearing disrupts the initial shape of the spot and produces an elongated spiral shape. Fig. 4.11 shows the apparent images of a spot with mild shearing environment ( $\tau_{sh} = 2.0$ ) for three different inclination angles. When we look face-on to the event ( $i \simeq 0^\circ$ ), there are no modulations by relativistic effects. For higher inclination angles ( $i = 30^\circ$  and  $i = 60^\circ$ ) lensing and boosting effects play major roles in the observed flux modulations. Specially for high inclinations, one can see how an Einstein arc develops when the spot passes behind the black hole and how photons coming from the accretion disk are blue-shifted on the left hand side of the image according to Doppler boosting. This set up allows us to simulate light curves for a wide range of possible free parameters, mainly by covering the range of all possible inclinations and spins of the black hole. Fig. 4.12 shows examples of light curves for different values of inclination and shearing time scale.

### 4.3 Pattern Recognition Analysis: Signatures of Lensing Effects

Fig. 4.13 shows the typical magnification of flux, polarization angle and degree of an orbiting spot emission as function of time. Here I showed the spots located at different distances from the black hole. These plots indicate the typical behavior of light curves when the strong gravitational regime is prominent and the strong lensing and boosting is happening. As one can see, the sweep in the polarization angle precedes the peak in flux magnification, while the peak of the degree of polarization follows the magnification peak (see Broderick and Loeb 2006 for a detailed discussion). Fig. 4.14 shows this typical behavior clearer according to the position of the corresponding cross-correlation's peaks. It is specially apparent that even with changing the position of the emitting source with respect to the black hole, this effect remains approximately the same.

This constant behavior encourages to check whether or not this type of pattern is manifested in the NIR light curves of Sgr A\*. For this purpose I used a simple pattern recognition algorithm mainly via multiplication of different cross correlation functions. Similar pattern recognition algorithms are used to identify gravitational wave signals from noisy data (Pappa et al. 2003, Goggin 2008).

Defining multiplication of two cross correlation functions (namely  $\sigma_i$  and  $\sigma_j$ ) as below:

$$\Sigma_{ij} = \sqrt{(\sigma_i + 1)(\sigma_j + 1)} - 1 \quad (4.25)$$

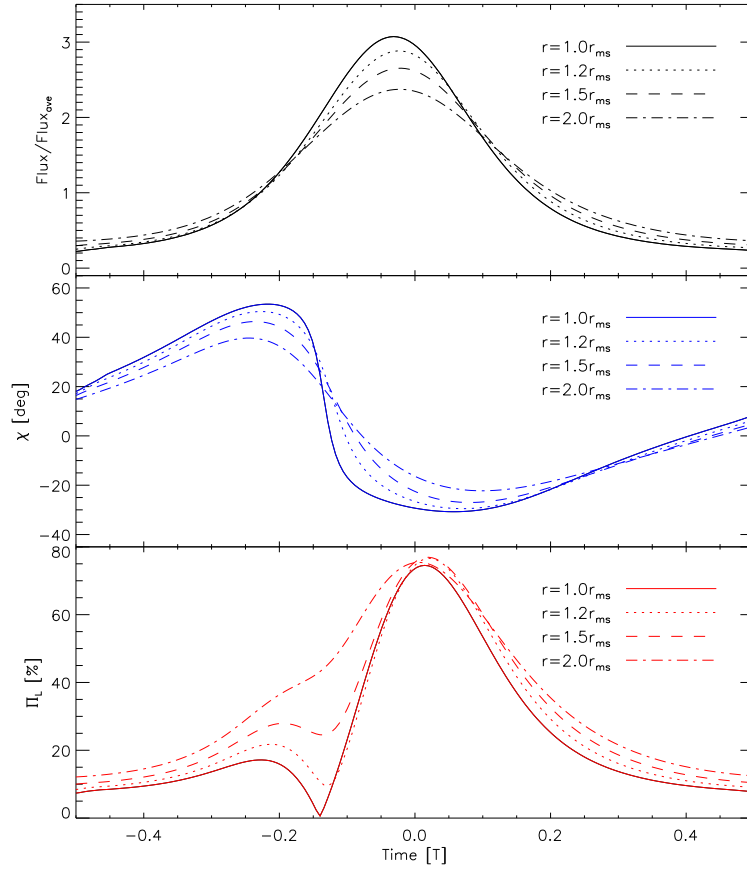
and repeating this procedure for cross correlation functions between observed flux and the theoretical magnification light curve ( $\sigma_f$ ), cross correlation functions between observed polarization angle and the theoretical polarization angle light curve ( $\sigma_\chi$ ) and the same function for the degree of polarization ( $\sigma_\Pi$ ), I derived a final pattern recognition coefficient product ( $\Sigma$ ). Fig. 4.15 shows how this pattern recognition coefficient is defined.

Fig. 4.16 shows the result of my pattern recognition analysis for the polarized flare events discussed in this thesis. In order to estimate how significant the peaks in the  $\Sigma$  function are, I have repeated the same analysis for  $10^4$  random red noise light curves simulated with the same method mentioned in chapter 3. In all but one case the patterns shown in Fig. 4.16 can be identified at the  $> 3\sigma$  to  $5\sigma$  level. This shows that strong lensing patterns are significantly manifested in my sample of NIR light curves. The detection of this strong lensing pattern strengthen the existence of a (clumpy) accretion disk around Sgr A\*.

### 4.3.1 A Spotted Accretion Disk?

Fig. 4.17 shows a selected 100 minutes window of the simulated light curves of the flux density, polarization degree and angle for a spot with constant shape ( $\tau_{sh} = \infty$ ), orbiting around a Kerr black hole ( $a = 0.5$ ) close to its marginally stable orbit ( $r = 1.1 \times r_{mso}$ ). The line of sight is inclined by 60 degrees ( $i = 60^\circ$ ). Gaussian white noise has been added to the simulated data in order to make the comparison of the periodicity and cross correlation with corresponding observational results easier. The level of the noise and the average error bars have been set from the average rms of corresponding observed light curves. The surface brightness of the components follows a profile similar to  $F(t; t_0, \tau)$  with  $\tau = 25$ . The maximum degree of polarization which can be achieved via synchrotron mechanism is around 70%. Since any kind of deviation from the ideal isotropic distribution of electrons around the magnetic field lines will suppress the degree of linear polarization, I set the initial value for the radiation from the spot to be 50%. I assumed that the photons originating from the non-flaring part of the accretion disk are weakly polarized ( $\sim 1\%$ ) since the main population of its NIR photons have thermal origin and relativistic electrons are randomly distributed around the magnetic field lines.

Fig. 4.17 (middle panel) also shows the result from autocorrelation and Lomb-Scargle analysis (similar to Figs. 3.10 & 3.13) and Fig. 4.17 (right panel) shows the results of the cross correlation analysis (similar to Fig. 3.16). The peaks close to the 0 minute time-lag are of special interest since they have the least dependency on the choice of free parameters and are mainly related to the basic idea that the flux modulations



**Figure 4.13:** Flux modulation (top), changes in polarization angle (middle) and degree (bottom) for a spot on circular orbit at  $1.0 \times r_{ms}$  (solid),  $1.2 \times r_{ms}$  (dotted),  $1.5 \times r_{ms}$  (dashed),  $2.0 \times r_{ms}$  (dot-dashed) around a Kerr black hole with spin parameter 0.5. The time unit is orbital time scale ( $T$ ).

are caused by relativistic effects. Figs. 4.17 and, 4.17 show that an orbiting spot is able to produce the same cross correlation pattern observed in my sample but the orbital frequency of the spot will be detected significantly as a quasi-periodic signal in Lomb-Scargle and ZDCF functions. The corresponding correlation functions of the 30 July 2005 observation are over-plotted in Fig. 4.17 for a better comparison. The main peak close to  $\tau = 0$  coincides very well for both observed and simulated cross-correlations.

Furthermore, I have simulated a spotted accretion disk. In this case spots are born, evolve and finally fade away as a function of time. These anomalies are distributed in the inner part of the accretion disk in a belt between  $1 - 2 \times r_{mso}$ . Radial and

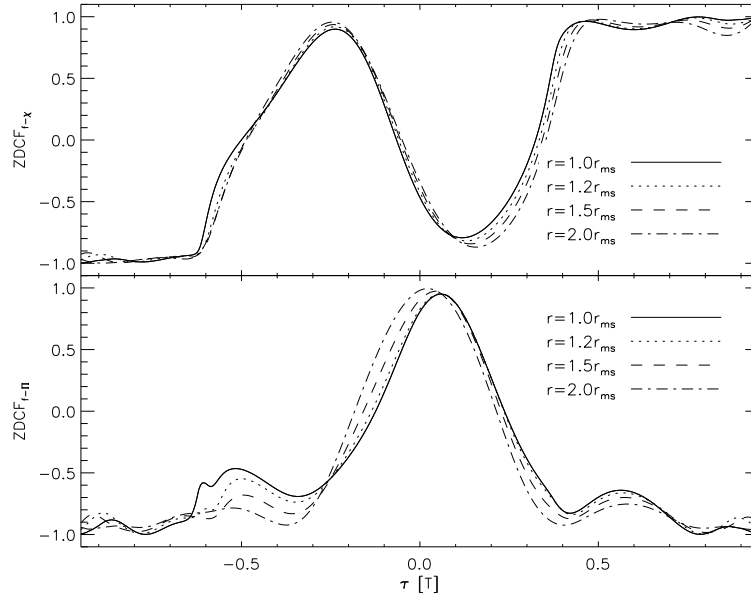


**Figure 4.14:** Cross correlation between changes in flux and polarization angle (top), and flux and polarization degree (bottom) for spot circular orbits at  $1.0 \times r_{ms}$  (solid),  $1.2 \times r_{ms}$  (dotted),  $1.5 \times r_{ms}$  (dashed),  $2.0 \times r_{ms}$  (dott-dashed) around a Kerr black hole with spin parameter 0.5 (Fig. 4.13). The time unit is orbital time scale ( $T$ ).

azimuthal distribution of the anomalies are completely random and their distribution in time follows a simple Poisson point process (see Pechacek et al. 2008).

Fig. 4.18 shows the snapshots of the spotted disk scenario as viewed by a distant observer from different inclination angles. The resultant magnification and polarimetric light curves are depicted in Fig. 4.19. White noise is added to all light curves in order to make the comparison between ZDCF and Lomb-Scargle results with corresponding observational results easier. As it can be seen in Fig. 4.18, the random distribution of the spots strongly suppresses the periodic signal in the Lomb-Scargle periodogram while the cross correlation between the magnification and changes in polarized flux still carries significant signal from the modulations influenced by strong gravity (Fig. 4.18). As a conclusion one can say that a general relativistic simulation of turbulences in the inner parts of an accretion disk resembles the observed behavior of Sgr A\* very well.

One must note that for the simulated data I have chosen typical values for spin and inclination (consistent with previous results by Eckart et al. 2006b and Meyer et al. 2006a,b), not trying to fit the actual data. As we can see, the data analysis and

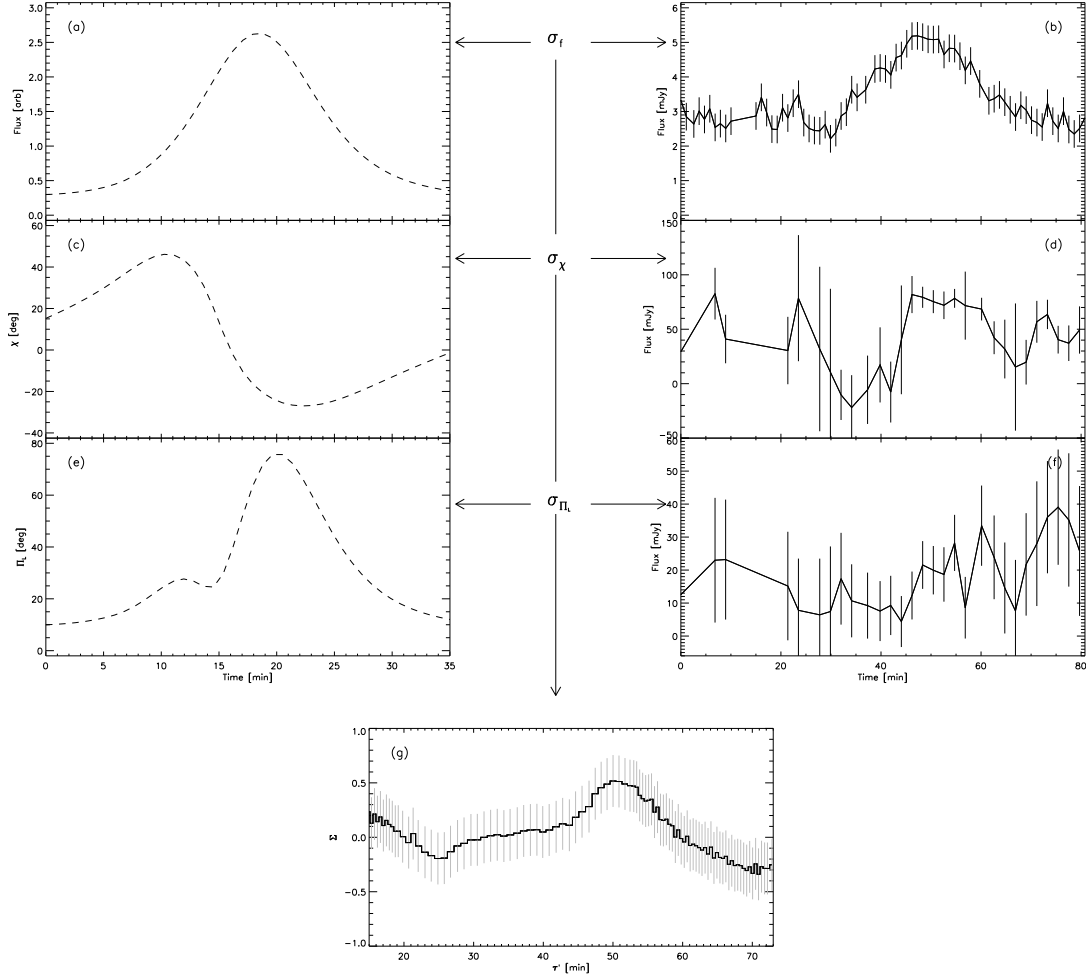


**Figure 4.15:** A sketch showing how the pattern recognition coefficient ( $\Sigma$ ) is defined.  $\Sigma$  is the multiplication product of cross correlation between observed and theoretical flux ( $\sigma_f$ ), observed and theoretical polarization angle ( $\sigma_X$ ) and observed and theoretical polarization degree ( $\sigma_\Pi$ ) light curves following Eq. 4.25. Note that  $\Sigma(\tau')$  (g) is defined as a function of  $\tau' = \tau + \frac{T_{sim}}{2}$  (where  $\tau$  is the time lag in units of minutes) in order to make it easier to match the position of its peaks with the position of the lensing events in the observations.

simulations show that even if there exists a low-level activity physical process in Sgr A\* which can be explained as random red-noise, the kind of observed correlations between the flux and polarization data can not be produced via a completely random process (without taking into account relativistic effects). Actually, the similarity between Figs.

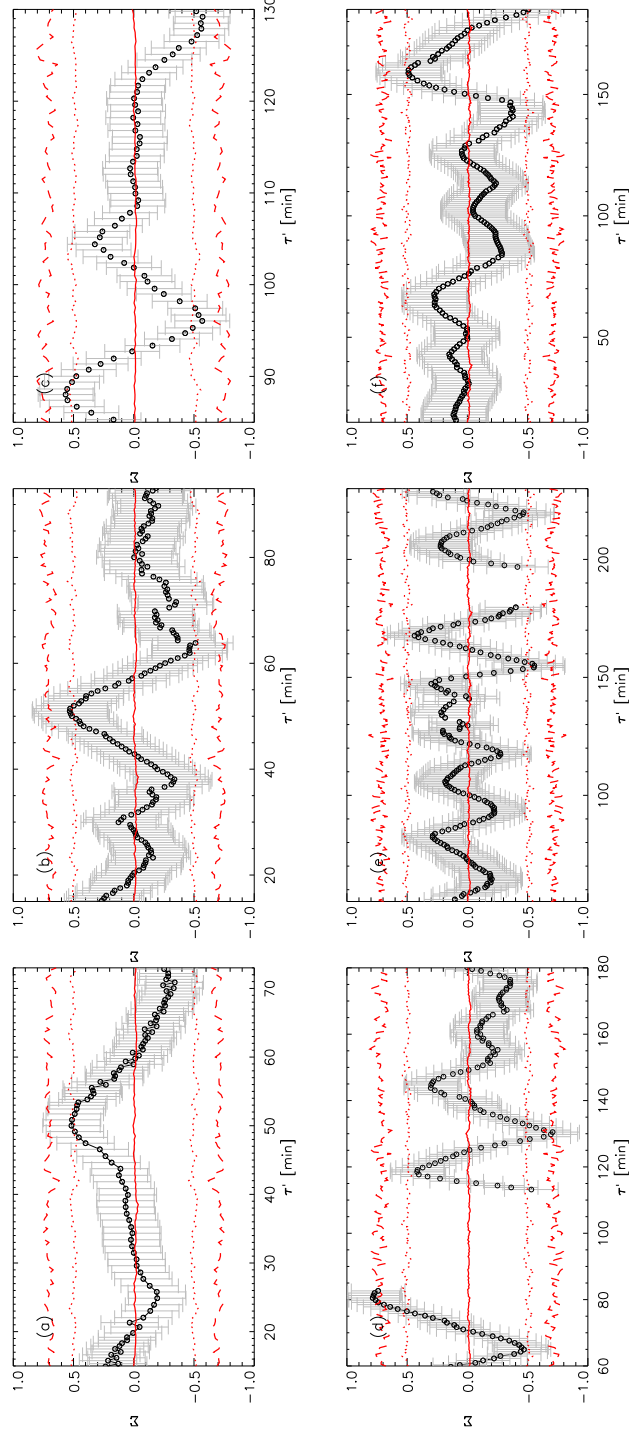


**Figure 4.16:** Pattern recognition coefficients (circles) as function of time for my sample of observations [13 June 2004 (a), 30 July 2005 (b), 1 June 2006 (c), 15 May 2007 (d), 17 May 2007 (e) and 28 May 2008 (f)]. The median (solid lines), 99.8% (dotted lines) and 99.99% (dashed lines) significance levels derived from  $10^4$  random red noise light curves are depicted in each image.

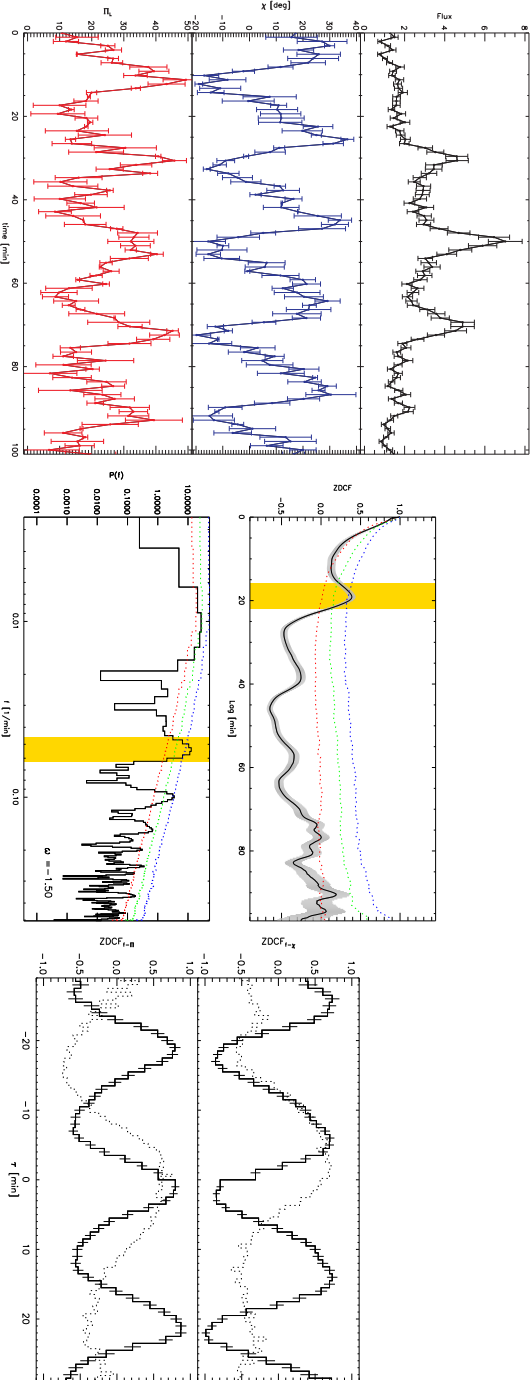


**Figure 4.17:** Left panel: A selected 100 minutes window of the white noise added simulated light curves of an orbiting spot plus a temporary variability in the accretion disk. The flux density is presented in arbitrary units (top). Middle and bottom panels show the changes in the angle (degree) of polarization. The spin of the black hole is set to be  $a = 0.5$  and the inclination fixed on  $i = 60^\circ$ . Middle panel: Same as Figs. 3.10 and 3.13 for the simulated light curves of Fig. 4.17. Top shows the autocorrelation of the flux while bottom is the Lomb-Scargle periodogram. The colored regions indicate the position of the peaks corresponding to the  $0.8 - 1.2 \times r_{mso}$  orbital time scales of a Kerr black hole with spin 0.5. Dotted lines show the median (red), 68.3% (green) and 99.8% (blue) confidence levels of the red noise. Right panel: Top (bottom): Cross correlation between total flux and polarization angle (degree) of the simulated light curve. Dotted lines indicate the corresponding cross correlation functions for the 30 July 2005 flare as the most similar case to the predictions of hot spot model.

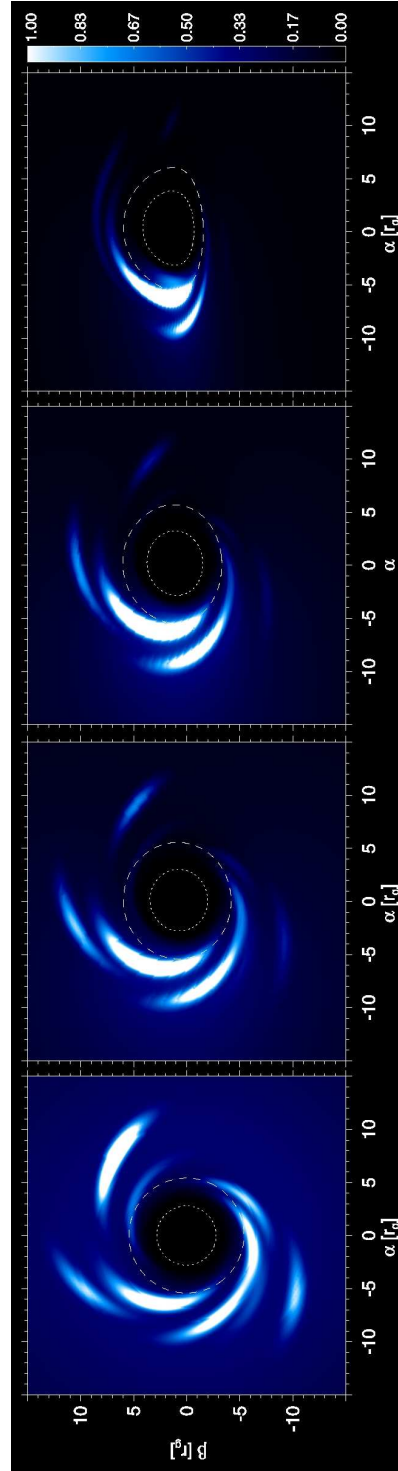


**Figure 4.18:** Same as Fig. 4.11 for the multi-component scenario. The observer's inclination is set to  $0^\circ$  (a),  $30^\circ$  (b),  $45^\circ$  (c) and  $70^\circ$  (d) (see discussion in the body of the text and Table. A.2 in Eckart et al. 2008a).

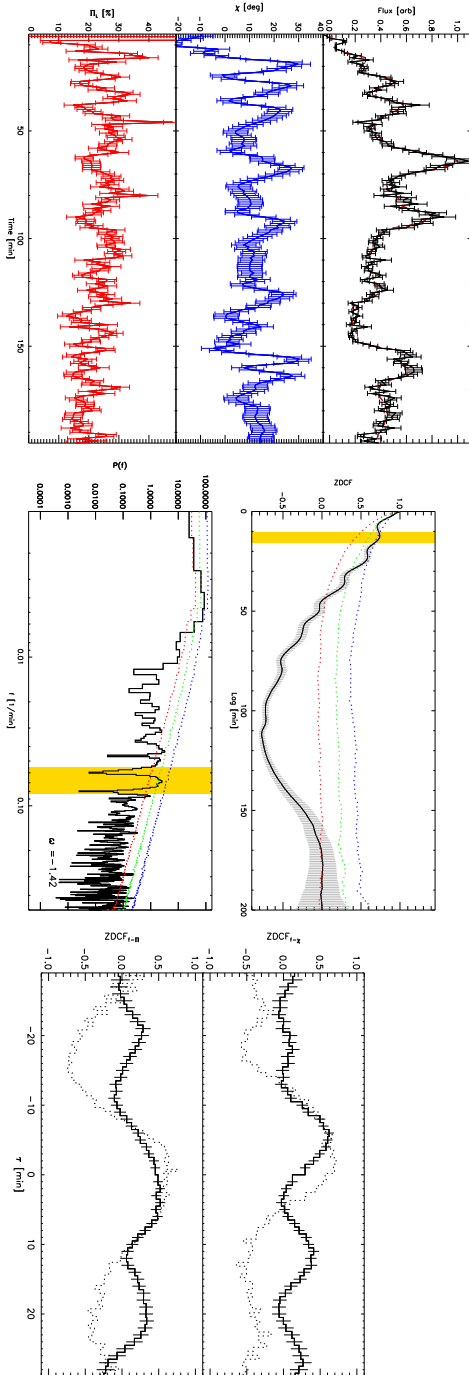


**Figure 4.19:** Left panel: Same as Fig. 4.17 for a selected 200 minutes window of the multi component scenario. Middle panel: Same as Figs. 4.17 for the multi component scenario. Right panel: Same as Figs. 4.17 for the multi component scenario.

4.17 & 4.18 and what is already observed in at least three different Sgr A\* flares (Figs. 3.13 and 3.16), supports the idea of orbiting matter around the galactic super-massive black hole.

## 4.4 Alternative Models

### 4.4.1 Relativistic Echoes

As mentioned before, the strength of ZDCF's peaks in Fig. 3.10 seems to be correlated with the brightness of flare events. This dependency on the brightness of the flares, and also the shape of the resulting ZDCFs, are very similar to the expected autocorrelation if the flux variations originate from geometric "light echoes" (Bursa et al. 2007; Fukumura et al. 2009). The expected periodicities from these models are different from the ones observed here, but their very close similarity keeps it open for future discussions. If a more detailed modeling of random flares happening at a distance from the black hole can show a possible  $\sim 20$  minutes QPO, then the light curves observed on 15 and 17 May 2007 could be the first observations of second images created from separated photon "bunches" (Fukumura 2009).

### 4.4.2 Jet Model

Shocks in relativistic jets can produce correlated total flux and polarized intensity. There is a possibility that under special circumstances (e.g special inclination, special magnetic field configuration etc.) a (episodic) relativistic outflow could produce the same correlation and pattern I have discovered in my observations.

Even though some NIR observations showed signs of QPOs (K-band: Genzel et al. 2003, Eckart et al. 2006b, Meyer et al. 2006a,b as well as in a recent L-band light curve: Trippe 2007), they are not present in all NIR light curves (e.g. see L-band light curve by Hornstein et al. 2007). Emission from a jet is sometimes used to explain radio to X-ray properties of Sgr A\* (see e.g. Markoff, Bower & Falcke 2007, Markoff, Nowak & Wilms 2005). It is a source structure associated with almost all galactic nuclei. Therefore I discuss the polarization and variability data also in the framework of a possible jet model.

The intrinsic source structure may affect the orientation of the polarization angle. Specially for a jet, the E-vector may prefer certain orientation with respect to the jet

direction. In Pollack, Taylor & Zayala (2003), a sample of 177 sources show a flat distribution of position angles with a tendency of the E-vector being perpendicular to the jet direction. While Rusk (1988) and Gabuzda & Cawthorne (2000) find weak indications for parallel orientations in stronger beamed jet sources. The mean 230 and 345 GHz intrinsic position angle is  $167^\circ \pm 7^\circ$  (E of N) with variations of  $\sim 31^\circ$  (Marrone et al. 2007). This position angle (within the errors) is orthogonal to that of the NIR polarized emission at about  $60\text{--}80^\circ$  (E of N). Both position angles also show a similar amount of variability (about  $30^\circ$ ; Eckart et al. 2006b, Meyer et al. 2006a,b). Alteration of orthogonal polarization angles is a common characteristic observed in jets. The flare spectrum of Sgr A\* is most likely to peak in the THz regime. In this case, orthogonal polarization angles between frequencies above (NIR) and below (mm/sub-mm domain) the synchrotron cutoff frequency are expected. However, Liu et al. (2006) also explain the millimeter and sub-millimeter polarization properties with their model of the emission being originated entirely from a hot accretion disk. This confines the emission to small regions and associate it with flare events occurring either in the corona of the disk or within the last stable orbit. This shows that the polarization angle by itself is not a sufficient indicator to decide between a jet and disk structure.

If the emission is originating from the foot point of a jet, then the time dependency of the flux density is not expected to be necessarily inferred via the amplification curves of the orbiting spot model, but only from jet instabilities and the synchrotron cooling. Here I investigate the effect of the synchrotron cooling and show in Fig. 4.20 simulated simultaneous light curves at  $2.2\mu\text{m}$  and  $3.8\mu\text{m}$ . For a mean magnetic field of  $B \sim 60$  G I took the frequency dependence of the synchrotron cooling time into account. The light curve was calculated using the SSC formalism described in the previous sections resulting in source components with different upper synchrotron cut-off frequencies. I also assumed that the synchrotron heating time is shorter than the cooling time and that at any time the NIR/MIR spectrum is dominated by a single source component. Source components that are bright at wavelengths  $\leq 2.2\mu\text{m}$  are bright at  $3.8\mu\text{m}$  for a correspondingly longer time. For source components that only appear at  $3.8\mu\text{m}$  I assumed a minimum cooling time of 3 minutes.

The middle curve in Fig. 4.20 (labeled  $2.2\mu\text{m}@3.8\mu\text{m}$ ) shows the  $3.8\mu\text{m}$  flux density contribution of the components that are bright at  $2.2\mu\text{m}$  and shorter wavelengths. All additional flux density contributions that are included in the  $3.8\mu\text{m}$  light curve are due to source components with synchrotron cut-offs at wavelengths long-ward of  $2.4\mu\text{m}$ . Figure 4.20 shows that, if the synchrotron cooling time is the only responsible effect for the observed flux density variations, then the light curves at longer infrared wavelengths will be strongly influenced by all lower energy synchrotron events and will not at all resemble the light curves observed at shorter NIR wavelengths. The quasi-simultaneous K- and L-band observations by Hornstein et al. (2007) show that the light curves at

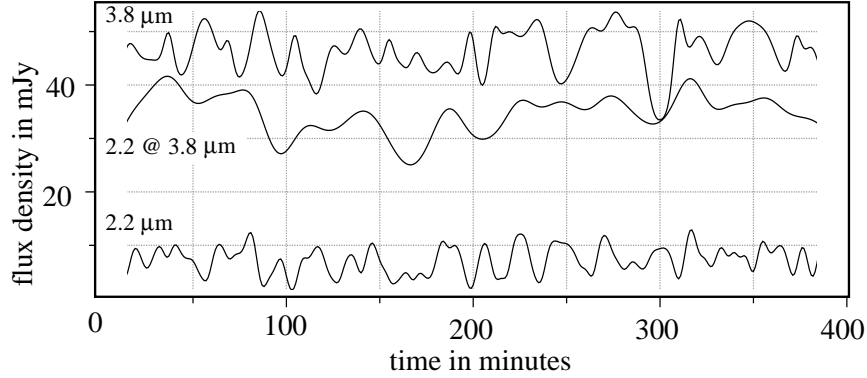


**Figure 4.20:** Simulated light curves at  $2.2\ \mu\text{m}$  and  $3.8\ \mu\text{m}$  wavelengths. The time scale has been set such that the rate of positive flux density excursions matches approximately the variability observed at  $2.2\ \mu\text{m}$ . The smooth central line shows the contribution of the  $2.2\ \mu\text{m}$  events at  $3.8\ \mu\text{m}$ . All additional flux density variations seen at  $3.8\ \mu\text{m}$  are due to lower energy components radiating long-ward of  $2.2\ \mu\text{m}$  (figure from Eckart et al. 2008a).

both wavelengths are well correlated, implying that the synchrotron cooling time scale is not relevant in this case. This suggests that the heating time scale was longer or that the component responsible for the flare event was stabilized by some unknown mechanism.

In the case of a jet, the  $17\pm 3$  minute infrared (optically thin) flux density variations may possibly be resultant from variations in the accretion process (or jet instabilities) rather than modulation from an orbiting spot. In this case one may expect that red noise variations on these short times scales are a natural extension of the variability found for longer periods. Fig. 4.21 shows the Sgr A\* flare amplitude as a function of the flare rate at  $2.2\ \mu\text{m}$ , under the assumption that the characteristic flare duration is of the order of 100 minutes (see Eckart et al. 2006a). Longer average flare durations will shift the graph towards lower rates and vice versa. The  $17\pm 3$  minute flux density variations lie close to the extrapolation of the power law line derived from flare measurements. However, while the sub-flare variability appears to be a natural extension of the flare rate spectrum, there is no evidence for a large number of  $2.2\ \mu\text{m}$  flares with durations between 100 and  $\sim 20$  minutes. The sub-flare variations also lie to the right of the flare rate power spectrum, as it would be expected for any signal that is clearly discernible from the variations imposed by the flares. It therefore appears to be equally likely that the sub-flare variations are due to a separate mechanism and lie beyond the possible cut-off for low flare amplitudes as discussed in Eckart et al. (2006a) or beyond an

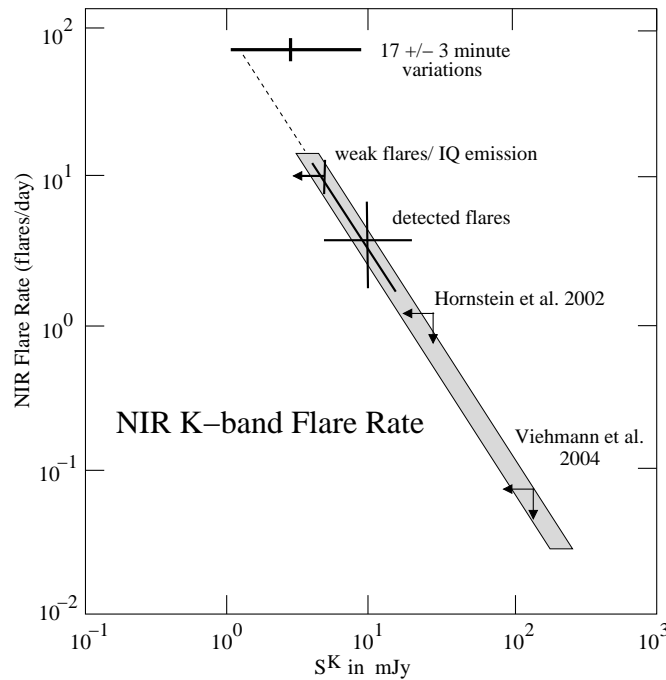


**Figure 4.21:** Flare rate as a function of flare amplitude for the NIR K-band emission from Sgr A\* under the assumption that the characteristic flare duration is of the order of 100 minutes (see Eckart et al. 2006a). The  $17 \pm 3$  minute variations observed as the sub-flare structure lies close to the extrapolation of the power law line derived from flare measurements (figure from Eckart et al. 2008a).

equally likely cut-off for high flare rates. Both cut-offs can be explained within the disk model proposed by Meyer et al. (2006a) in which the flare is due to a sound wave travelling within a finite disk. The disk size limitation may reflect itself in a typical flare duration and flux density, as well as a possible drop in power for shorter variations. The higher sub-flare rates are then due to typical turbulence size scales of components within the disk (e.g. Hawley & Balbus 1991, Arlt & Rüdiger 2001). The brightest of these orbiting components would give rise to the claimed QPOs. The finite orbiting disk may, however, be identical to the foot point of a jet or wind (see e.g. Markoff, Bower & Falcke 2007, Markoff, Nowak & Wilms 2005).

### 4.4.3 A Disk Plus a Short Jet

A source structure in which an accretion disk is associated with a short jet may explain most of the observed properties of Sgr A\*. Details of expected jet geometries are discussed by Markoff, Bower & Falcke (2007). The higher energy events would be responsible for the observed NIR/X-ray flares. The lower energy events would contribute most to long wavelength infra-red emission. Higher energy events within the disk may be more stable and result in the observed sub-flare properties. Lower energy events may occur more detached from the disk, less stable and more dominated by the effects of synchrotron cooling. While the sub-mm emission will be intimately associated with the SSC flare events, the mm-emission will originate after adiabatic expansion, further down stream the wind or jet emanating from the accretion disk. In addition, radial and azimuthal expansion of the emission zone within the disk may occur. This is consistent with the traveling sound wave picture presented by Meyer et al. (2006a). Further expansion of the wind or jet towards more extended and diffuse source components that dominate the cm-emission will occur.

A number of essential scenarios that comprise most of the properties associated with infrared/X-ray Sgr A\* light curves can be explained within the model:

1. Let us assume that the mean upper synchrotron cut-off lies short-ward of the NIR K-band, the source components are stable for several cooling time scales, and the flux density variations are due to their orbital motion around Sgr A\*: In this case correlated variabilities should be observed in the NIR K- and L-bands. This situation corresponds to the orbiting spot model, represents events that take place within the accretion disk and will give rise to observed polarized infrared light curves that show quasi-periodic sub-flare structure.
2. Here I assume that the mean upper synchrotron cut-off lies in or long-ward of the NIR K-band, but the flare events producing flux at increasingly longer wavelengths take place at increasing distances above the accretion plane: In this case variations are preferentially observed at short NIR wavelengths. At longer wavelengths they are less likely to occur and the variations are not strongly correlated with those at shorter NIR wavelengths. This scenario would be consistent with the presence of a short jet and would again be valid especially for lower energy events.
3. The mean upper synchrotron cut-off lies short-ward of the NIR K-band, but the source components are stable for only a few cooling time scales. In this case sub-flares should be observed in e.g. the NIR K- and L-bands, but they should be largely uncorrelated with respect to each other. This could especially be the case

for lower energy events that result in infrared flux density variations but are not accompanied by significant X-ray flares.

4. If the source component flux density variations are dominated by the synchrotron cooling time scale and are not due to relativistic effects caused by the orbital motion of the components around Sgr A\*, then the K- and L-band light curves are not correlated with each other and no significant variations are observed. Such a scenario may be observed if the flux density variations occur above the disk, along the short jet or within the disk at larger disk radii. The quasi-simultaneous K- and L-band measurements by Hornstein et al. (2007) make cases 3 and 4 less likely. Very weak X-ray events have also been reported by Eckart et al. (2006a). In these cases the X-ray peak flux density was only of the order of 1.2 to 1.8 times the quiescent X-ray flux density associated with Sgr A\*. Such weak X-ray events require that the constant bremsstrahlung and variable SSC component of Sgr A\* can be distinguished through sensitive, high angular resolution X-ray measurements as provided by the ACIS-I instrument aboard the *Chandra X-ray Observatory*. However, I need to measure more flares to obtain a higher statistical significance.

If the entire NIR/X-ray flare event happens to occur above the Sgr A\* accretion disk or extends a few  $r_g$  into the disk corona, then the modulation expected from an orbital spot may be significantly reduced. Above the disk the spot radiation will be subject to less gravitational bending from the black hole and potentially more extended. In that case a larger section of the underlying disk will be heated by the X-ray flare and an increasing amount of the lower infrared flare emission will be inverse Compton scattered rather than synchrotron self Compton scattered. These effects will also lead to a significant reduction of any sub-flare contrast.

## 4.5 Geometry of the Emitting Region

In this section I discuss the basic assumption of the existence of an azimuthal asymmetry in the accretion flow of Sgr A\*. Recently, Falanga et al. (2007) and Karas et al. (2007) discussed that a global spiral pattern of disturbance, with an orbiting speed not directly associated with the underlying Keplerian velocity, can fit the observed NIR and X-ray modulations of Sgr A\*. Their model has been used to fit the observed X-ray flare on 31 August 2004 (Falanga et al. 2007).

In order to reproduce the same density profile in the inner part of the disk, I have

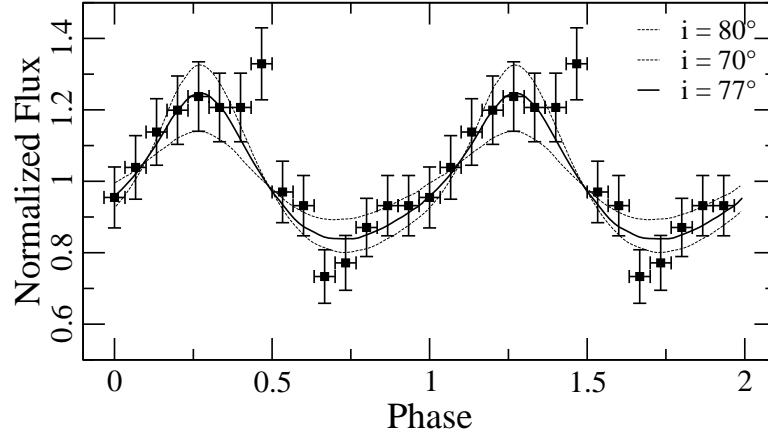


**Figure 4.22:** X-ray flare of the 31 August 2004 observed in the 2-10 keV energy band. The best fit model (inclination =  $77^\circ$ ) is shown by the solid line. The dashed line represent upper and lower limits inclination angles:  $80^\circ$  and  $70^\circ$ , respectively. (Figure from Falanga et al. 2008).

used a spiral pattern, characterized by the emissivity function given below:

$$I_\nu \propto r^{-\gamma} \sin^\beta(\phi + \alpha \log(\frac{r}{r_0})) \quad (4.26)$$

while the power-law index,  $\gamma$ , describes the overall radial decrease in the emissivity,  $\arctan(\alpha)$  is the pitch angle and  $r_0$  determines the outer radius where the pattern fades away. This parametrization approximates a spiral pattern evolving in the background of a Keplerian disk. The main emission mechanism is assumed to be synchrotron radiation from relativistic electrons with the same energy distribution as Eq. (1). The shape of the spiral pattern highly depends on  $\gamma, \beta, \alpha$  and  $r_0$ . I parametrize my model in such a way that it facilitates a straightforward comparison with Tagger et al. (2006).  $\gamma = 1, \alpha = \beta = 6$  and  $r_0 = 20$  give the best approximation (see Fig. 4.24). Fig. 4.25 shows the changes in the flux and polarimetric quantities, as measured by a distant observer for different inclinations. As mentioned before (and discussed in detail by Falanga et al. 2007 and Karas et al. 2008), such a spiral pattern can produce the same typical behavior in flux modulation as can be caused by an azimuthal anomaly in the accretion disk.

The main idea in my simulations is to include the polarimetric radiation transfer in curved space-time, which provides the possibility to compare the behavior of different geometrical configurations. It seems that even though both of these geometrical set ups (spiral shape or compact spot) show the same behavior in flux, the observed polarized flux will behave significantly different. In order to reduce the effects of my specific

assumptions about the emission process and magnify the signatures which result only from different geometrical structures, I have chosen a toy model for the initial polarized emission:  $Q_\nu = I_\nu$ ,  $U_\nu = V_\nu = 0$ . Fig. 4.25 shows that the spiral pattern is unable to produce strong changes in the polarization angle, while a compact azimuthal source produces a highly variable polarization angle. Due to aberration, photons that come from different parts of the disk are polarized differently, even for Schwarzschild black holes. For the Kerr case, the rotation of the polarization vector will be added because of gravitational frame dragging. The dependency of these changes on the position of the emitted photon, is depicted in Fig. 4.26. The top panel of Fig. 4.26 shows how the polarization vector of the emitted photons will be rotated due to the strong gravity of the central black hole. As one can see, there is a clear knot visible in this contour graph. If the radiating source passes through this knot, the observed polarization angle will swing dramatically (for a detailed discussion see Dovčiak et al. 2008). As the bottom panel of Fig. 4.26 shows, when a compact azimuthal source orbiting around the black hole close to its marginally stable orbit, this nod will be passed. The amount of change in the polarization angle depends on the compactness of the source, its position relative to the black hole, the inclination of the observer and the spin of the black hole. On the

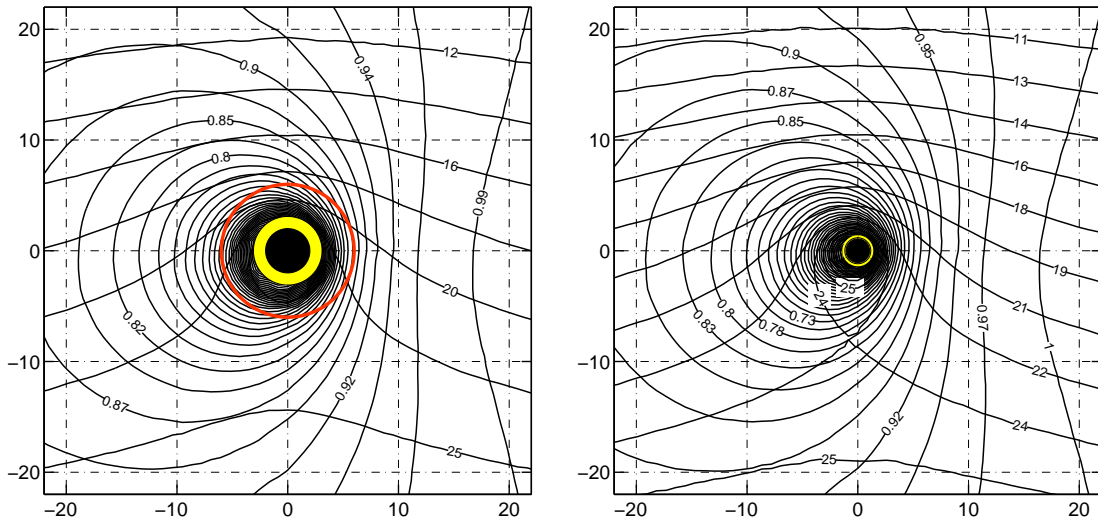


**Figure 4.23:** Levels of light-travel time  $t(r, \phi) = \text{const}$  (approximately horizontal direction of the contour lines) are plotted together with levels of the redshift function  $g(r, \phi) = \text{const}$  (roundish shape of the latter). The contours are constructed in the equatorial plane of Kerr black hole for two cases: a non-rotating hole ( $a = 0$ , left panel) and for a maximally rotating hole ( $a = 1$ , right panel). The observer is located towards top of the figure at an inclination of  $\theta_o = 20^\circ$  (Figure from Karas et al. 2007).

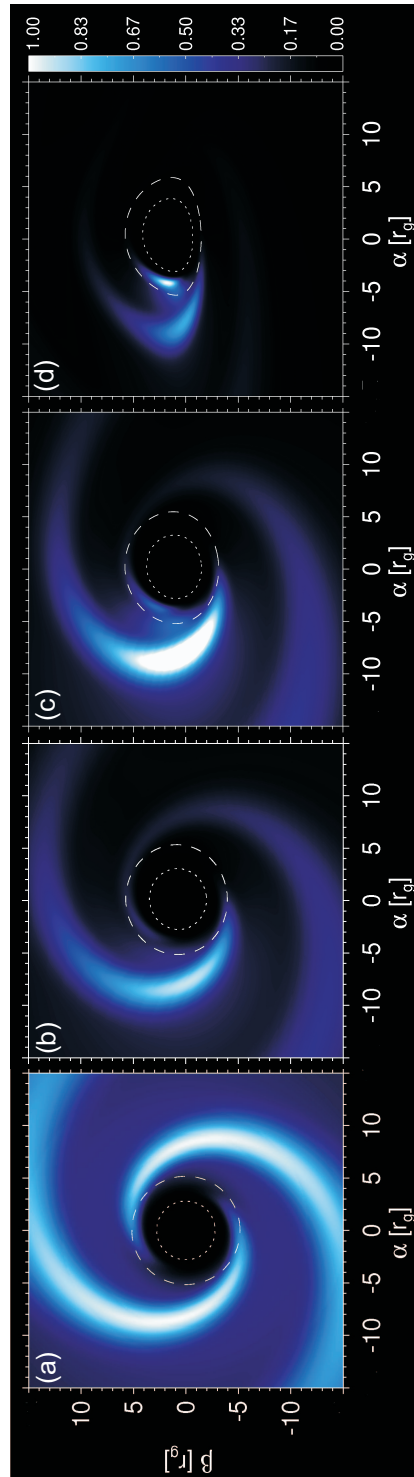


**Figure 4.24:** Snapshots of the orbiting spiral pattern as they appear to a distant observer looking along a line of sight inclined by  $0^\circ$  (a),  $30^\circ$  (b),  $45^\circ$  (c) and  $70^\circ$  (d) [relative to the normal to the disk]. See also caption of Fig. 4.10

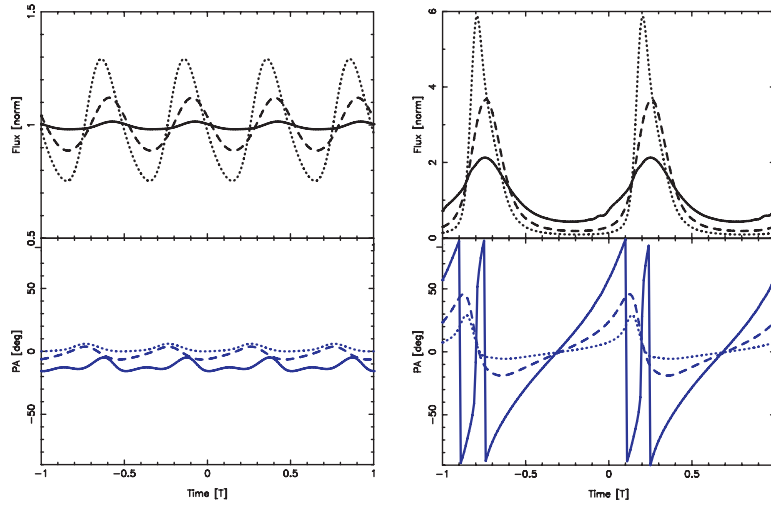


**Figure 4.25:** Light curves of the normalized flux (top, black) and polarization angle (bottom, blue) observed at infinity, resulted from general relativistic modulations associated with a spiral pattern (left) or a compact spot (right). Light curves are shown for three different inclinations:  $i = 30^\circ$  (solid line),  $i = 60^\circ$  (dashed line) and  $i = 80^\circ$  (dotted line). The modulations happen two times more for the spiral pattern than the spot in the same interval, according to the existence of two symmetrical arms. Flux values are normalized according to their average values. The spin of the black hole is set to be zero ( $a = 0$ ).

other hand, if the flare emitting region is a deformed pattern extending in both radial and azimuthal directions, the swing in the polarization angle will not be strong. This is because in each point of the light curve the polarization angle is the average of photons that come from different parts of the disk, and have different polarization angle (Fig. 4.26). As a result, the swings in the angles cancel each other out and no significant swing will be observed.

The presence of changes in the degree of NIR polarization and swings in the observed polarization angle simultaneous to the flux magnifications support the idea that the geometrical shape of the sources is dominated by compact azimuthal asymmetries rather than radially extended spiral patterns (see also discussion in the next chapter about the differences in the centroid motions of these two type of geometries). Here, I must note that as Tagger et al. (2006) have mentioned, a second initial configuration was used in their simulations (simulation no. 2, Tagger et al. 2006). In that set up, a clump of matter starts spiraling towards the black hole and produces the spiral Rossby wave instability. There, the ratio of the surface brightness between the hot core moving radially inward and the tail which is produced, plays a critical role in the resultant

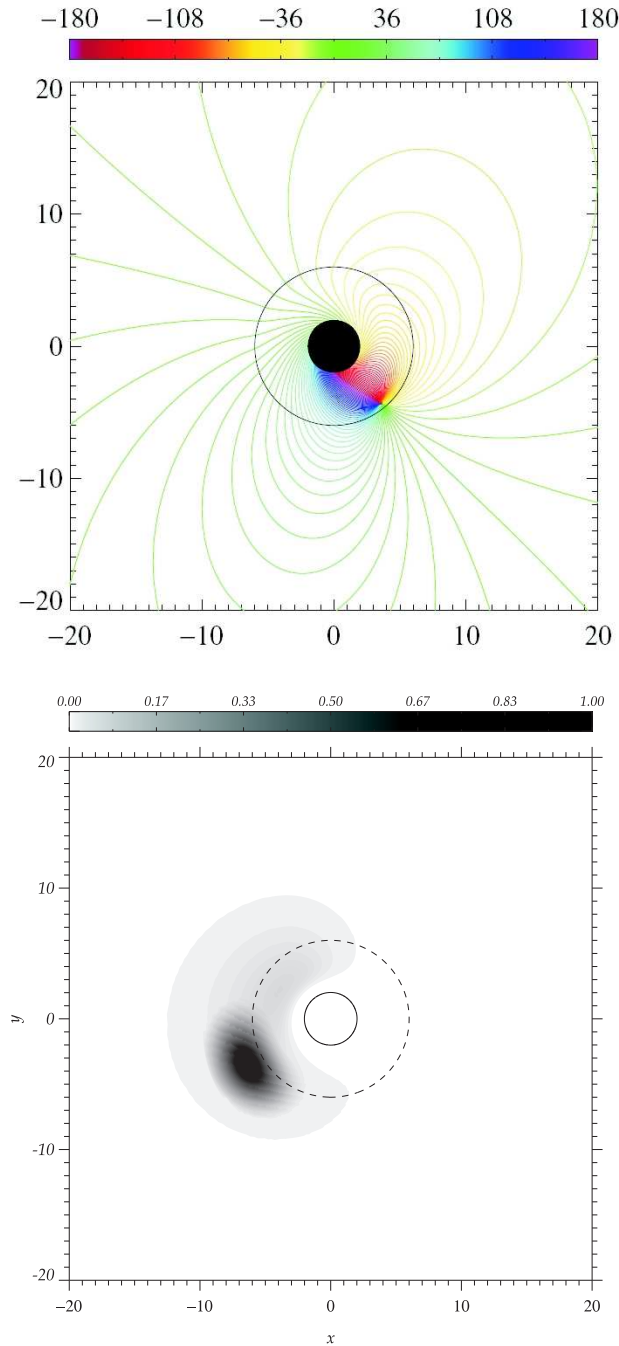


**Figure 4.26:** Top: Contour graphs showing the changes in polarization angle due to general relativistic effects. Bottom: Spatial emissivity distribution of a compact hot spot. The observer's inclination is  $i = 45^\circ$  and the black hole is assumed to be spin-less. The observer is located on the top of the pictures. The innermost stable orbit is shown in both images (solid line in top image and dashed line in the bottom). The graphs are represented in the coordinates  $x = r \cos \phi, y = r \sin \phi$  in the equatorial plane where  $r$  and  $\phi$  are Boyer-Lindquist coordinates. Units are  $r_g$  in the  $x$ - $y$  coordinates.

light curves. If the hot core is dramatically brighter than the tail, there is no practical difference between this scenario and the orbiting spot model. For a complete polarization study of Rossby wave instabilities, one needs simulated profiles of MHD surface densities as a function of time which is beyond the scope of this thesis.

## 4.6 Magnetic Field Structure and Geometrical Orientation of the System

In my simulations the structure of the magnetic field lines according to the black hole/accretion disk system can be controlled by a set of parameters  $[\eta, \psi]$ . Of special interest are two extreme configurations in which the envelope of the accelerated electrons is located inside the accretion disk with a global toroidal magnetic field (model I:  $[\eta = \frac{\pi}{2}, \psi = \frac{\pi}{2}]$ ) or inside a region with magnetic field lines perpendicular to the disk (model II:  $[\eta = 0, \psi = 0]$ ). The latter can be interpreted as the spot being located at

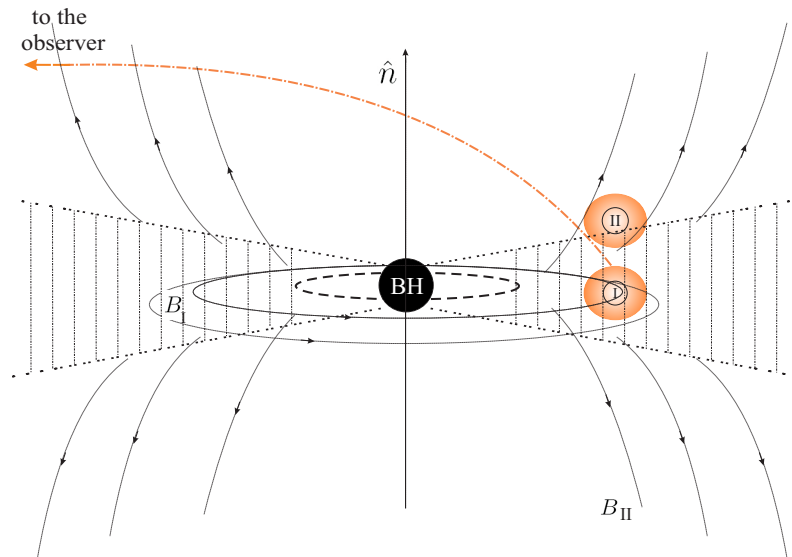


**Figure 4.27:** A sketch of the model (not to scale) of two extreme cases of global magnetic field configuration. Model I: the localized flare happens inside the accretion disk, where the dominant component of the magnetic field is toroidal ( $B_I$ ). Model II: over-density of the accelerated electrons happens at the tip of a possible short jet (wind). Magnetic field lines ( $B_{II}$ ) are assumed to be elongated toward the axial symmetry axis of the system, parallel to the normal to the disk ( $\hat{n}$ .)

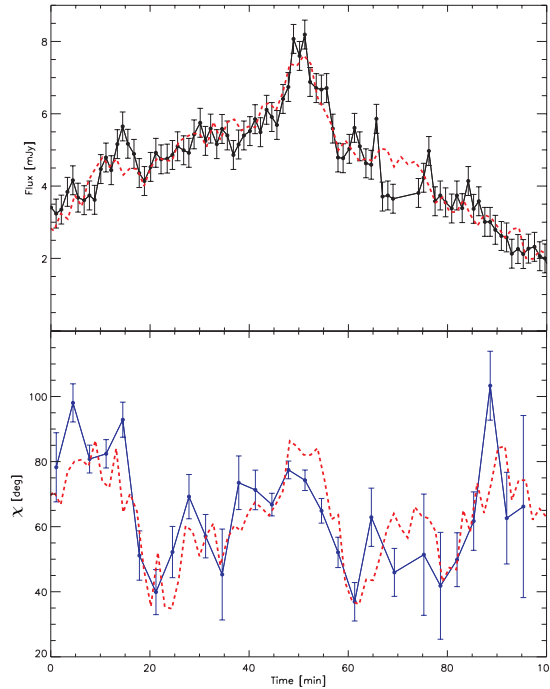


**Figure 4.28:** Best fit achieved for the flux and polarization angle of 30 July 2005 flare. The points and error bars represent the observation, red dashed lines show the model with Gaussian noise being added. The parameters are presented in Table 4.2.

the tip of a jet with magnetic field lines aligned parallel to its symmetry axis (see Fig. 4.27).

I assumed that the magnetic field inside the accretion disk is dominated by the toroidal component. This structure is compatible with the results of several MHD simulations (Hawley & Balbus 1991; Hirose et al. 2004; De Villiers et al. 2003). However, in my case it is not clear if the cloud of accelerated electrons is located inside the accretion disk, somewhere above it in the corona, or even inside the tip of a possible short jet/wind. In fact, there is a possibility that a source structure in which an accretion disk is associated with a short jet/collimated outflow can explain the multi-wavelength behavior of Sgr A\* (Markoff et al. 2001; Yuan et al. 2002; Eckart et al. 2005, 2006a, 2008a-c). Here I discuss how different orientations of the magnetic field lines inside the emitting region affect the resultant physical parameters that one can extract via fitting the model to the observed data.

The KY code allows us to simulate light curves for a wide range of free parameters, so one can fit the model parameters to the actual observed data (Meyer et al. 2006a,b,

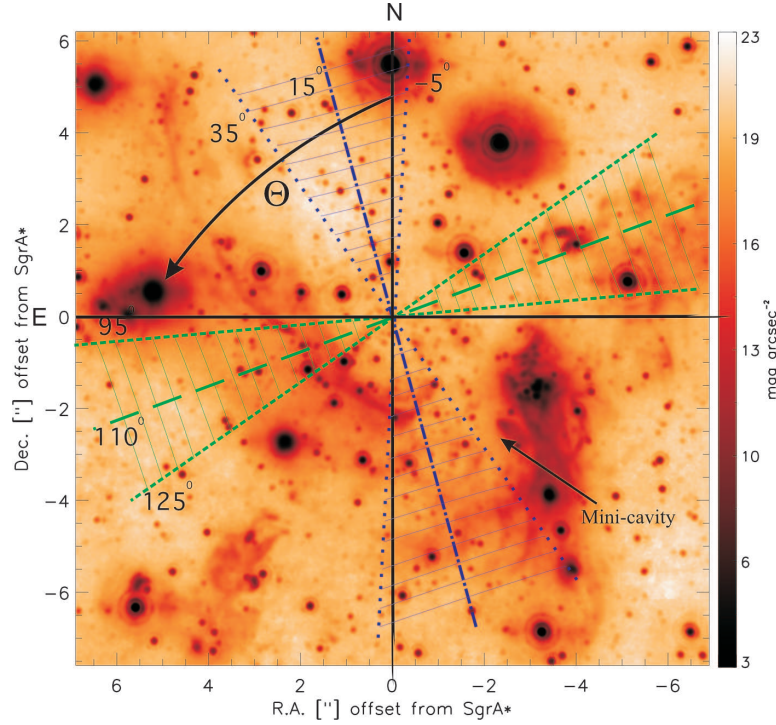


**Figure 4.29:** The resulting orientations for the direction of a possible collimated outflow from Sgr A\* ( $\Theta$ ) for model I (blue dashed dotted line) and model II (green long dashed line). The shaded regions indicate the range of possible values of  $\Theta$  for  $\chi_{red}^2 \pm 1$  interval. The background image shows the Galactic Center environment in NIR L' band. Sgr A\* is located at the center of the image. The position of the mini cavity (indicated by an arrow), coincides well with the predictions of model I.

2007; Eckart et al. 2006a,b, 2008). For this purpose, simulations have been carried out as they cover a wide enough range of possible inclinations ( $0.1^\circ \leq i \leq 85^\circ$ ), the initial degree of linear polarization ( $0\% \leq \Pi_L \leq 70\%$ ), possible combinations of  $\eta$  and  $\psi$ , and different orientations of the whole system on the sky ( $0^\circ \leq \Theta \leq 90^\circ$ ). Here  $\Theta$  defines the direction of the normal to the accretion disk projected on the sky. The spot has an initial radius of  $1R_s$  and orbits very close to the marginally stable orbit of a Kerr black hole ( $a = 0.5$ ). The dimensionless shearing time scale is fixed to be 2.0 ( $\tau_{sh} = 2.0$ ), and the ratio of the surface brightness of the spot to the torus is set to 5. I have chosen these values according to existing results of several fits to the NIR flares (Meyer et al. 2006a,b; Eckart et al. 2006b, 2008).

As a first step, I focus on model I ( $[\eta = \frac{\pi}{2}, \psi = \frac{\pi}{2}]$ ). In order to find the fit with best  $\chi_{red}^2$  I have carried out a grid search in the  $(i - \Theta - \Pi_L)$  parameter space. The steps

for  $i$ ,  $\Theta$  and  $\Pi_L$  have been chosen to be  $5^\circ$ ,  $5^\circ$  and  $5\%$ , respectively. The least  $\chi_{red}^2$  value was achieved for a high inclination angle ( $i = 60^\circ$ ),  $\Theta = 15^\circ$  and highly polarized source ( $\Pi_L = 50\%$ ) (see Fig. 4.28 and Table 4.2). Fig. 4.29 shows the resultant possible range for the orientation of the correlated outflow/wind in this scenario. Interestingly, the observed position of the mini cavity lies well within this interval. Mužić et al. (2007) have shown how a collimated outflow from the position of Sgr A\* can describe the observed motion of filamentary structures and the mini-cavity, according to their observations in the NIR  $L'$ -band. This observational evidence supports the idea that the NIR flares actually originate from accelerated electrons within an accretion disk.

For model II ( $[\eta = 0, \psi = 0]$ ), the envelope of relativistic electrons has been located somewhere in the bottom of an outflow. The least  $\chi_{red}^2$  achieved for this model and related parameters are presented in Table 4.2. Possible directions of this jet structure are depicted in Fig. 4.29. As one can see,  $\chi_{red}^2$  value values and observational facts support the idea that the NIR photons originate from the inner parts of an accretion disk rather than an outflow (Thorne 1994, Blandford 2001).

One can also invert the process, and try to constrain the magnetic field structure of the emitting region by fixing the direction of the outflow in the plane of the sky (model III). For this purpose, a  $\chi_{red}^2$  search has been carried out, assuming that the normal to the disk is fixed at  $\Theta = 30^\circ$ . This is the best value that can fit the observed position of the mini-cavity (Mužić et al. 2007). By a good approximation, the best fit is achieved for a toroidal magnetic field structure (see Table 4.2). This shows that if any future observations reveal traces of an outflow from Sgr A\*, NIR polarimetry could be used as a tool to constrain its magnetic field structure.

Model	$a$	$\eta$ [deg]	$\psi$ [deg]	$r_0$ [ $r_g$ ]	$r_{spot}$ [ $r_{mso}$ ]	$R$	$\Pi_L$ [%]	$i$ [deg]	$\Theta$ [deg]	$\chi_{red}^2 \pm 1$
I	0.5	90	90	4	1.1	5	50 $\pm$ 10	60 $\pm$ 15	15 $\pm$ 20	1.63 $\pm$ 1
II	0.5	0	0	4	1.1	5	50 $\pm$ 10	65 $\pm$ 10	110 $\pm$ 15	2.95 $\pm$ 1
III	0.5	78.56 $\pm$ 12	72 $\pm$ 18	4	1.1	5	60 $\pm$ 10	50 $\pm$ 20	30	1.54 $\pm$ 1

**Table 4.2:** Final parameters resulting from least  $\chi_{red}^2$  fit to the NIR flare observed on 30 July 2005, for the three models (I, II & III) discussed in the text. The grid search has been performed on  $\Pi_L$ ,  $i$  and  $\Theta$ . for the models I and II. The free parameters in model III are  $\Pi_L$ ,  $i$ ,  $\eta$  and  $\psi$ .

## Chapter 5

# Next Generation of NIR Interferometry

*Earth is round and attracts everything  
towards its center. This is Gravity.*

-A. Biruni (973 AD - 1048 AD)  
Physicist, astronomer, mathematician,  
chemist, philosopher, and historian.

### 5.1 Introduction

GRAVITY is a general purpose instrument for the Very Large Telescope Interferometer (VLTI; Glindemann et al. 2000) with two main capabilities: phase-referenced imaging, and narrow-angle astrometry. The design of the instrument is driven by a set of specific science cases, that also give its name (General Relativity Analysis via VLT InTerferometrY, or GRAVITY), namely to explore the so far untested regime of strong gravity encountered at a few hundred down to a few Schwarzschild radii from super-massive objects.

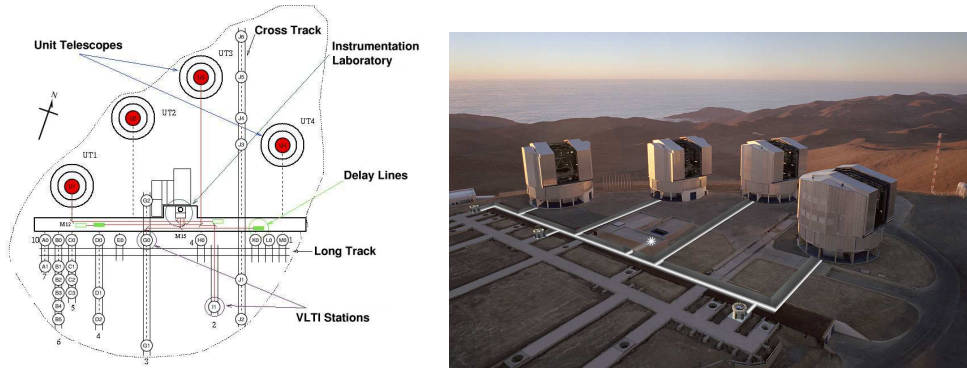


**Figure 5.1:** Schematic (left) and real (right) view of the ESO Paranal site showing the locations of the 8.4 m diameter Unit Telescopes (UTs) and various installations for the VLT Interferometer (VLTI). Three 1.8 m VLTI Auxiliary Telescopes (ATs) and paths of the light beams have been shown in the photos. Also seen are some of the 30 "stations" where the ATs will be positioned for observations and from where the light beams from the telescopes can enter the Interferometric Tunnel below. The straight structures are supports for the rails on which the telescopes can move from one station to another. The Interferometric Laboratory is at the center of the platform (Credit: ESO).

GRAVITY, an interferometric imager with  $10 \mu\text{as}$  astrometric capability, coupled with spectroscopic and polarization modes, and optimized to exploit the exquisite sensitivity of the  $4 \times 4$  VLTI system, will revolutionize dynamical measurements of celestial sources interacting by gravity. GRAVITY may be able to test General Relativity in the presently unexplored strong curvature limit. It will also be able to unambiguously detect and measure the mass of black holes in massive star clusters throughout the Milky Way and in many active galactic nuclei to  $z \sim 0.1$ . It will make unique measurements on gas jets in young stellar objects and active galactic nuclei. It will explore binary stars, exoplanet systems and young stellar disks. Because of its superb sensitivity GRAVITY will excel in milli-arcsecond phase-referenced imaging of faint celestial sources of any kind. Because of its outstanding astrometric capabilities, it will detect motions throughout the local Universe and perhaps beyond. Because of its spectroscopic and polarimetric capabilities it will be able to detect gas motions and magnetic field structures on sub-milliarcsecond scales. To reach these ambitious goals it is clearly needed to build the ultimate instrument that can be presently realistically conceived. State of the art detectors and wave-front sensing are required for reaching the faint source limits ( $K \sim 15 - 19$ ). A NIR wave-front sensor is needed for embedded objects and the GC.

## 5.2 GRAVITY at Work: Implications for Sgr A\*

Because of its proximity, Sgr A\* is known as the best candidate for studying the details of physical processes on the event horizon scales (Falcke et al. 2000; Bromley et al. 2001). VLT and Keck telescopes already have achieved angular resolutions as high as 40 mas in their imaging mode (Genzel et al. 2003; Eckart et al. 2004, 2006a,b; Ghez et al. 2005). In interferometric mode these telescopes can observe with resolutions of the order of only a few mas. The next generation of VLT Interferometer instrument, namely GRAVITY, would be able to achieve resolutions of the order of 10  $\mu$ as, in its phase reference tracking mode. GRAVITY will try to measure the position of the lumicenter of the flares with respect to a reference source. For such a measurement the  $1\sigma$  uncertainty is  $\pm 10\mu$ as with an integration time of 5 minutes on an assumed  $K = 15$  point source. The real necessary integration time for that precision is of course directly dependent on the magnitude of the flare. This resolution is high enough to track the centroid motion of NIR images of Sgr A\* with a resolution of the order of one Schwarzschild radius (Eisenhauer et al. 2005, 2008; Gillessen et al. 2006). These unique features make the next generation of VLTI a perfect instrument for high accuracy astrometry of the matter around Sgr A\*. Recently, Doeleman et al. (2008) proposed a VLBI configuration with a high enough time resolution that could possibly track the centroid motion of sub-mm images of Sgr A\* with even higher angular resolution. In this section we present the results of our study on centroid motion of the NIR image of Sgr A\*.

Some predictions of the centroid motions related to the hot spot model already have been studied by several authors (Broderick & Loeb 2006a,b; Paumard et al. 2006; Zamaninasab et al. 2008b; Hamaus et al. 2009). In previous works, it has been mainly assumed that the spots preserve their shape in time. This assumption has been mainly based on the presence of strong magnetic field lines or "unknown mechanisms" (Hamaus et al. 2009). Here I will show that actually it is crucial to take into account the effects of gravitational shearing inside the accretion disk, since the predicted results can change dramatically. The other crucial fact that must be considered in the simulations is due to the NIR photons, which come from the body of the accretion disk and confuse with the spot's emission. Since GRAVITY can only achieve its 10  $\mu$ as resolution in the phase reference tracking mode and not in the imaging mode, even a constant confusion from the (thermal) electrons inside the accretion disk can not be reduced.

Fig. 5.2 represents how these two mentioned parameters can affect the expected centroid tracks and may present a complication in detecting the plasma structure close to the event horizon of Sgr A\*. The simulated paths in Fig. 5.2 belong to a configuration where the observer is aligned approximately face-on ( $i \simeq 0^\circ$ ). This is the inclination in

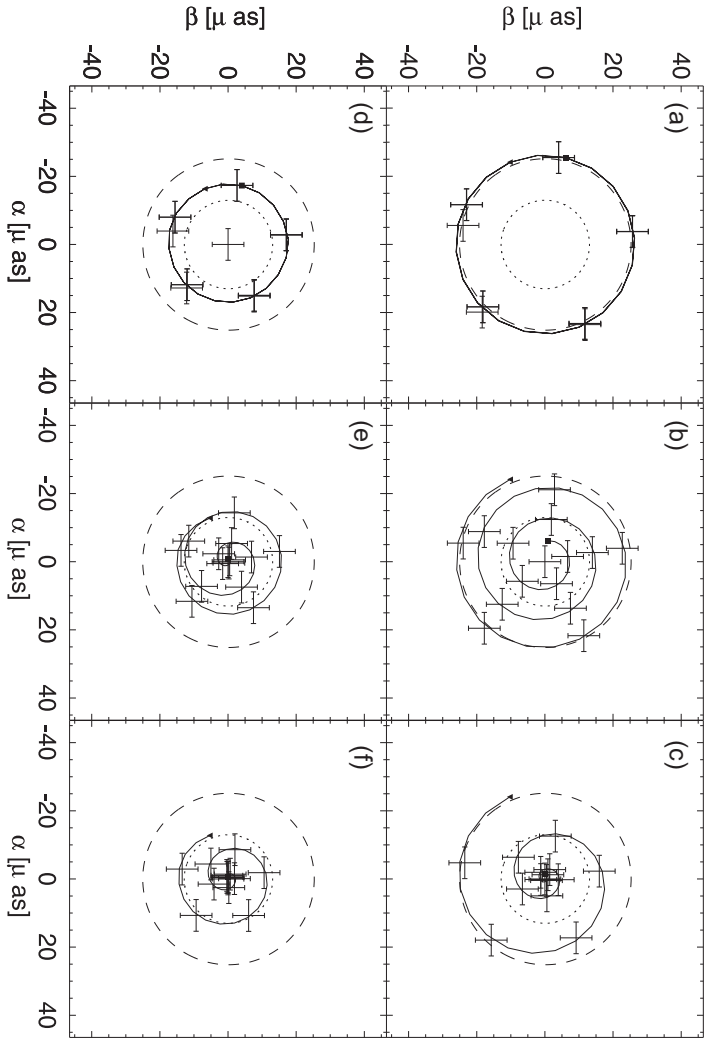


**Figure 5.2:** The centroid motion of NIR images viewed from  $0^\circ$  above the orbital plane for a Kerr black hole with spin 0.5. The first row shows the paths for the background-subtracted images for different values of gravitational shearing time scale. Each column shows the paths for the  $\tau_{sh}$  values  $\infty$ , 2.0 and 1.0 from left to right. The second row shows the same paths for the images without background subtraction. The error bars show the simulated positions as expected to be observed by GRAVITY (FWHM  $\sim 8.5\mu\text{as}$ ) with time resolution of 5 minutes. The whole paths belongs to three orbital times. A triangle indicates the beginning and a square the end of the track. Both coordinates are labeled in  $\mu\text{as}$  units. The dotted and dashed lines indicate the position of the event horizon and the marginally stable orbit, respectively.

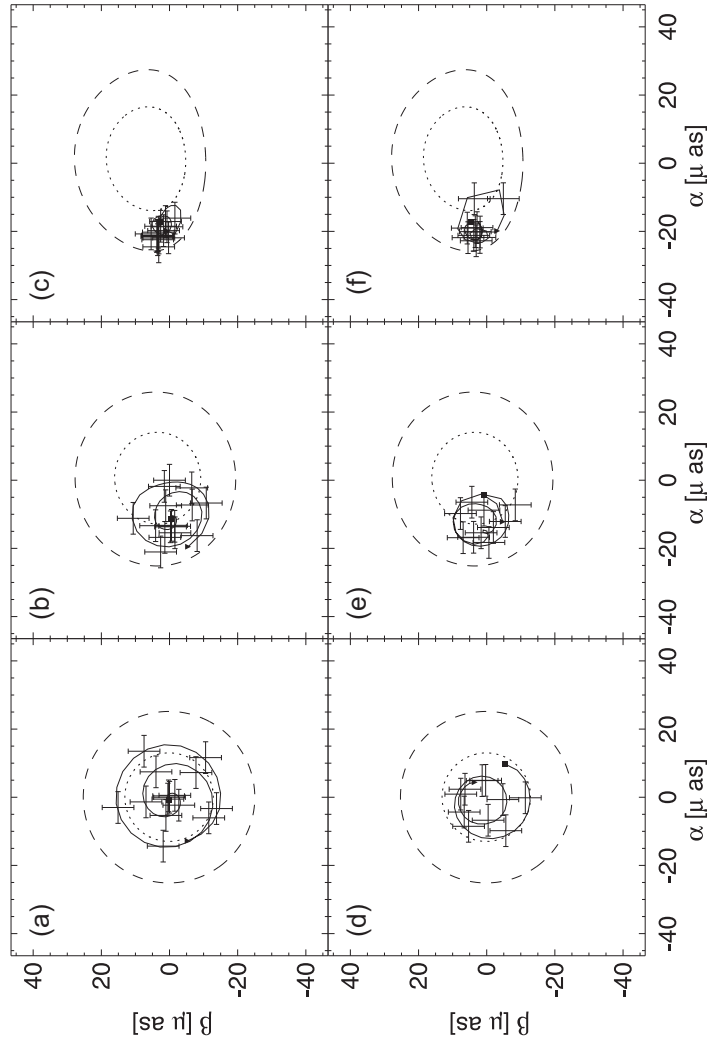


**Figure 5.3:** Similar to Fig. 5.2 where different columns represent different values of inclination (from left to right:  $i = 0.1^\circ$ ,  $i = 30^\circ$ ,  $i = 60^\circ$ ). (a-c) shows the centroid track of an orbiting spot with  $\tau_{sh} = 2.0$ . (d-f) shows the centroid for a multi component model (see Fig. 4.18).

which the clearest wobbling of the centroid is expected to be seen. Fig. 5.2a shows that the position wanders of the center of the images are large enough to be detected easily if GRAVITY could achieve its 5 minutes time resolution (simulated points). Panels b & c in Fig. 5.2 show how gravitational shearing changes the centroid track. Specially, one can see that in the case of pure Keplerian shearing the change in the center is detectable for approximately only six points. The second row (Fig. 5.2, panels *d-f*) shows the result of the simulated tracks including the effect of confusion due to the NIR photons coming from the inner parts of the accretion disk.

Fig. 5.3 shows the centroid paths of spots orbiting in a mild shearing environment ( $\tau_{sh} = 2.0$ ) for three different inclinations ( $i = 0.1^\circ, 30^\circ, 60^\circ$ ) in presence of confusion from the torus. Panel *c* shows that the detection of any position wander becomes even more difficult in the case of a shearing spot observed at high inclinations. The bottom row in Fig. 5.3 shows the centroid motion resultant from simulations including several emitting components (see Fig. 4.18). The photons originating from the spot are highly polarized, while the radiation from the torus is weakly polarized. This fact may lead us to a solution for compensating for this kind of confusion. Fig. 5.4 shows how different the apparent images of the flares will be when they are observed in total flux or two orthogonal polarized channels. One sees that the different centroid paths can be revealed, if GRAVITY could achieve its  $10 \mu\text{as}$  resolution in the polarimetry mode (Fig.5.4).

To summarize the results of this chapter, one can say that a non-detection of a position wander in NIR images of Sgr A\* will not rule out spotted disk scenario. On the other hand, a clear detection of such a position wander by GRAVITY would strongly favors the spot model, and would open a new era in studying the physics of high gravitational regimes.

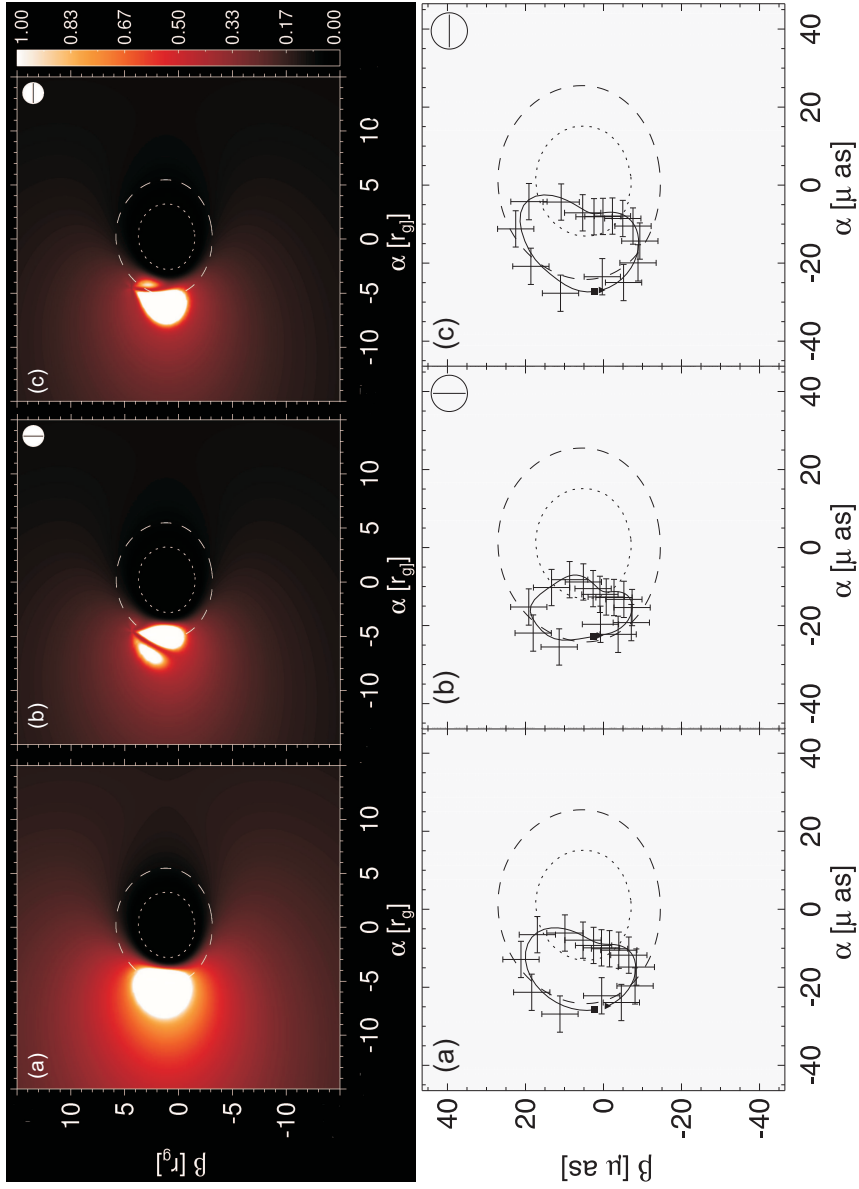


**Figure 5.4:** Top: Apparent images of flare event for a distant observer looking along a line of sight inclined by  $45^\circ$  in total flux (a), ordinary (b) and extra-ordinary polarized channels (c). Bottom: Centroid paths for the same inclinations as the top panel in the total flux (a), ordinary (b) and extra-ordinary (c) polarized channels. See also caption of Fig. 5.2.



## Chapter 6

# Near Infrared Polarimetry as a Tool for Testing Properties of Black Holes

*The secrets eternal neither you know nor I  
And answer to the riddle neither you know nor I  
Behind the veil there is such talk about us, why  
When the veil falls, neither you remain nor I*

-Omar Khayyám (1048 AD - 1131 AD)  
Astronomer, mathematician, philosopher,  
physician and poet.

As I have already mentioned, existence of orbiting spots in the inner parts of the accretion flows into very compact objects (e.g. black hole, Neutron stars) has been proposed by several authors as the responsible mechanism for their variable emissions that show QPO behavior. Here in this chapter I will focus on a new method of time resolved polarimetric observations that can lead to constrain the intrinsic parameters of these objects. Such an orbiting blob inside the accretion flow will produce observable effects both in flux and polarization. I discussed in detail (e.g. in section 4.3) how flux magnification and changes in polarization angle (degree) follow specific pattern in this scenario and I probed such a pattern inside our sample of the NIR flares of Sgr A\*. Here

in this chapter I will discuss a new and more straightforward method which can be used for constraining the physical parameters of black holes (or other compact objects with QPO behavior). The new method has several advantages, the most important is that it only deals with direct observables and there is no need for assuming (or constraining by a  $\chi^2$ -fit) any intrinsic physical properties for the accretion flow (e.g. initial degree of polarization). This makes the predictions of the model clearer and testing against the observations more straightforward.

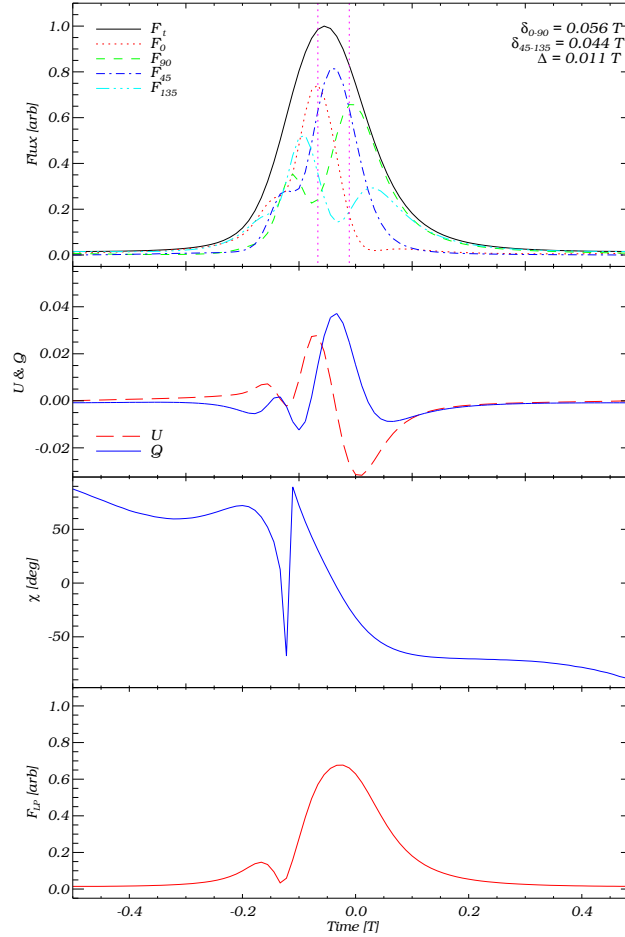
## 6.1 Time Delay Between Polarization Channels: Predictions of the Hot Spot Model

Figure 6.1 shows the behavior of flux light curves in 4 orthogonal polarization channels (namely  $0^\circ$ ,  $45^\circ$ ,  $90^\circ$  and  $135^\circ$  channels) for a blob located at the ISCO of a Schwarzschild black hole, viewed by an observer inclined by  $60^\circ$ . One can see that each channel reaches its maximum in a different time. The reason for this behavior is the strong Doppler beaming as well as the light focusing, especially at high viewing angles when the spot orbit is seen almost edge-on. Furthermore, the rotation of the polarization plane along the photon trajectory plays a role. The latter effect is particularly strong for small radii of the spot orbit, in which a critical point occurs (Dovciak et al. 2008a,b, see also section 4.5). As Figs. 6.1 and 6.2 show, the time-lag between each orthogonal pair of polarization channels can be measured with two different methods: a maximum to maximum time delay measurement (Fig. 6.1 top) or making a cross-correlation between  $0^\circ - 90^\circ$  and  $45^\circ - 135^\circ$  channels (Fig. 6.2 bottom). There is another parameter that can provide useful information about the properties of a light curve: the so called *magnification factor*. I have defined this value as

$$\mu = \frac{T}{\Phi} \quad (6.1)$$

where  $T$  is the period and  $\Phi$  is the FWHM of a Gaussian fit to the light curve. This factor is a measure of how much the flux is magnified by lensing or boosting effects.

The main question is how these time-lags ( $\delta_{0-90}$  and  $\delta_{45-135}$ ) and magnification factor ( $\mu$ ) are sensitive to changes in the global parameters of the model. The main free-parameters are the spin of the black hole  $a$ , inclination of the observer  $i$ , and the distance of the blob from the black hole (here is controlled by the parameter  $\mathbf{pos}$ ;  $r_{sp} = \mathbf{pos} \times r_{ms}$ ). I have performed a full analysis of how such measurements can be used to determine precisely the spin and inclination of the temporarily bright accreting matter around Sgr A\*. Figures 6.3 - 6.6 show the  $\delta_{0-90}$ ,  $\delta_{45-135}$ ,  $\mu$  and  $T$  as functions



**Figure 6.1:** Total flux magnification and the corresponding polarization channels (top), Stokes parameters  $U$  and  $Q$  (second row), polarization angle (third row) and polarized fraction of the total flux (bottom) for a spot orbiting at the marginally stable orbit of a Schwarzschild black hole and viewed by an observer inclined by  $60^\circ$ . The measured maximum-maximum time-lags of two orthogonal channels ( $\delta_{0-90}$  and  $\delta_{45-135}$ ) and their absolute difference ( $\Delta$ ) are depicted on the right top corner of the first panel.

of spin and inclination for a black hole of the mass  $4 \times 10^6 M_\odot$  (comparable to the mass of Sgr A\*). In each figure the functions have been shown for two distances of the spot from the black hole ( $\text{pos}=1.0$  and  $\text{pos}=1.5$ ). I have calculated these functions for

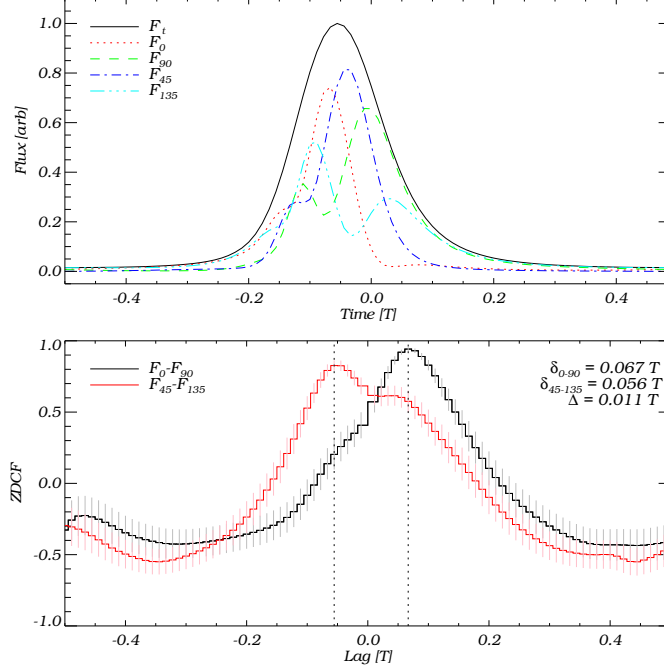


**Figure 6.2:** Cross-correlation between orthogonal channel light curves similar to Fig. 6.1 ( $0^\circ$  &  $90^\circ$  (black) and  $45^\circ$  &  $135^\circ$  (red)).  $\Delta$  is the absolute of the difference between the maxima of two cross-correlation functions.

a wide range of acceptable values of this parameter ( $\text{pos}=0.5\dots3.0$ ; with a step of 0.1). One can see that these four different functions behave independently from each other in the  $a - i$  space. This fact shows that these functions can be used together as a tool for constraining spin and inclination of an accreting system. I will discuss in the next section the implications of such a model on Sagittarius A\*.

## 6.2 Implications for Sgr A\*

Both VLT and Subaru telescopes are able to obtain rapid time series of the polarized emission from Sgr A\* in NIR  $K_s$ -band in order to determine the time delay between the flares in orthogonal polarization channels. As I discussed in chapter 2, several flares of Sgr A\* already have been observed in polarimetry mode with the time resolution of

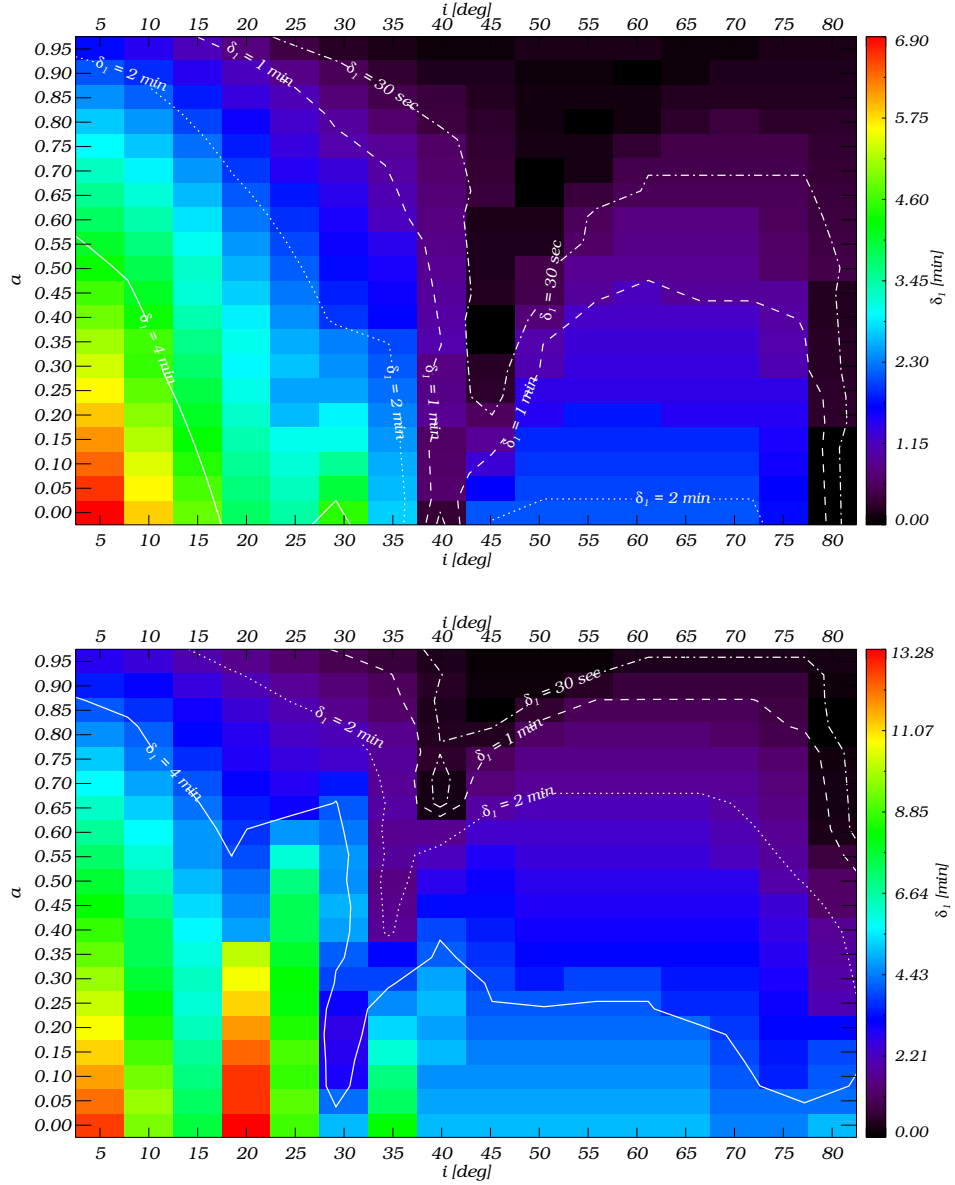


**Figure 6.3:** Time-lag between  $0^\circ$  and  $90^\circ$  channels ( $\delta_1 \equiv \delta_{0-90}$ ) as a function of spin and inclination for  $pos=1.0$  (top) and  $pos=1.5$  (bottom). The contours of  $\delta_1 = 0.5, 1, 2$  and  $4$  minutes are over-plotted on each image. The black hole mass is set to  $4 \times 10^6 M_\odot$ .

$\sim 2 - 3$  minutes. Figure 6.7 show the best example of such event. Each channel shows

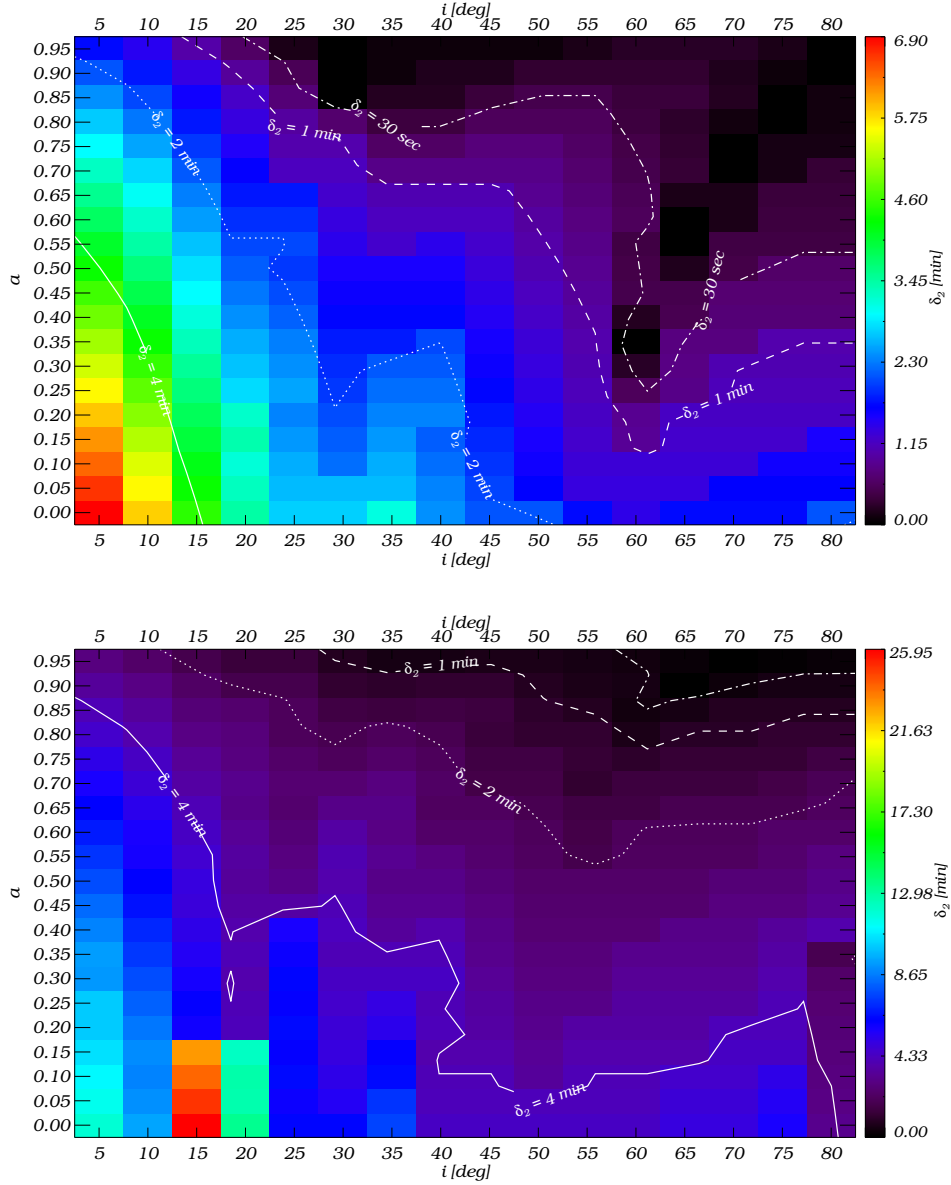


**Figure 6.4:** Time-lag between  $45^\circ$  and  $135^\circ$  channels ( $\delta_2 \equiv \delta_{45-135}$ ) as a function of spin and inclination for  $pos=1.0$  (top) and  $pos=1.5$  (bottom). The contours of  $\delta_2 = 0.5, 1, 2$  and  $4$  minutes are over-plotted on each image. The black hole mass is set to  $4 \times 10^6 M_\odot$ .

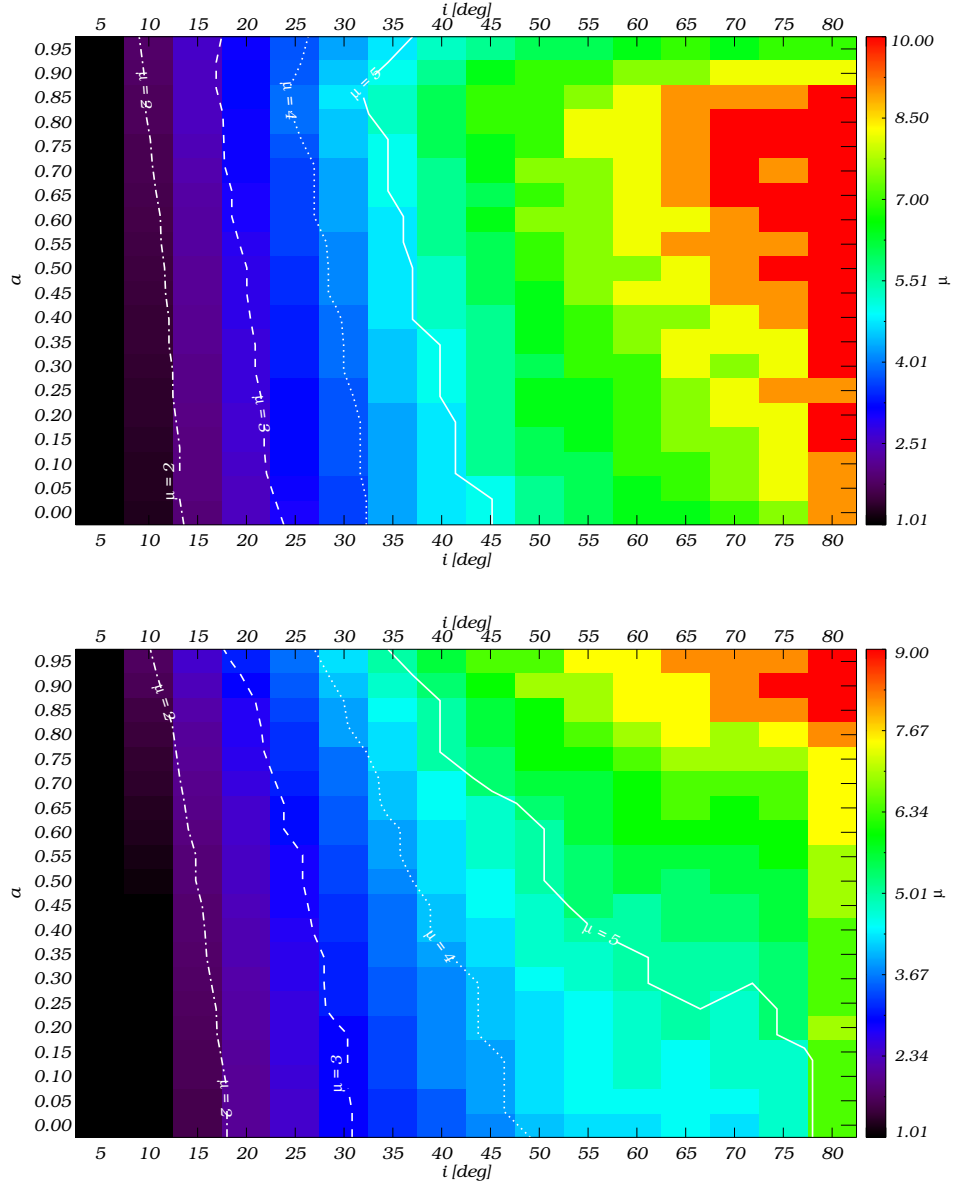


**Figure 6.5:** Flux magnification ( $\mu$ ) as a function of spin and inclination for  $\text{pos}=1.0$  (top) and  $\text{pos}=1.5$  (bottom). The contours of  $\mu=2, 3, 4$  and  $5$  are over-plotted on each image. The black hole mass is set to  $4 \times 10^6 M_{\odot}$ .

an approximate Gaussian behavior while clear time-lags between maxima (specially

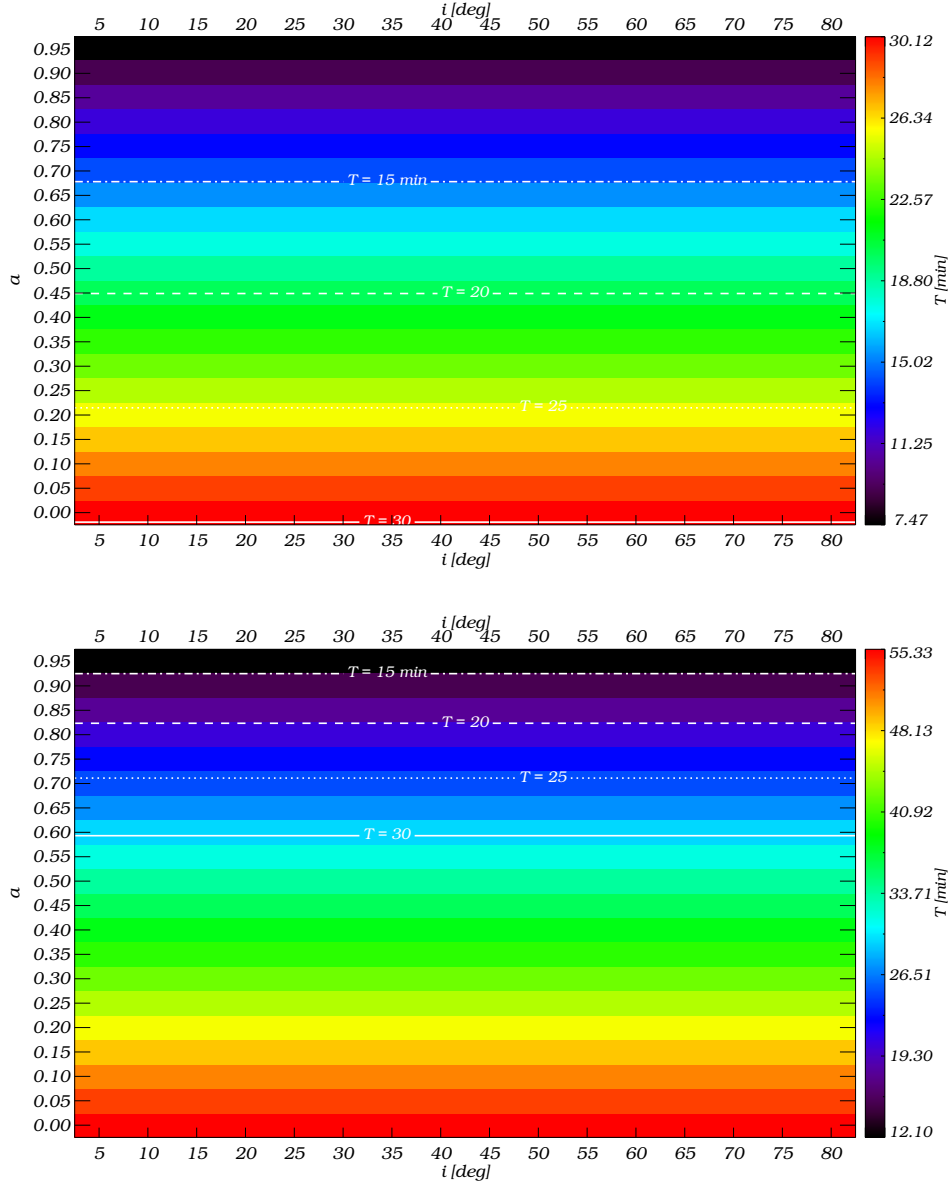


**Figure 6.6:** Orbital time scale ( $T$ ) as a function of spin and inclination for  $pos=1.0$  (top) and  $pos=1.5$  (bottom). The contours of  $T=15$ , 20, 25 and 30 minutes are overplotted on each image. The black hole mass is set to  $4 \times 10^6 M_{\odot}$ .

between orthogonal pairs) are visible. Observationally, the rate at which high SNR

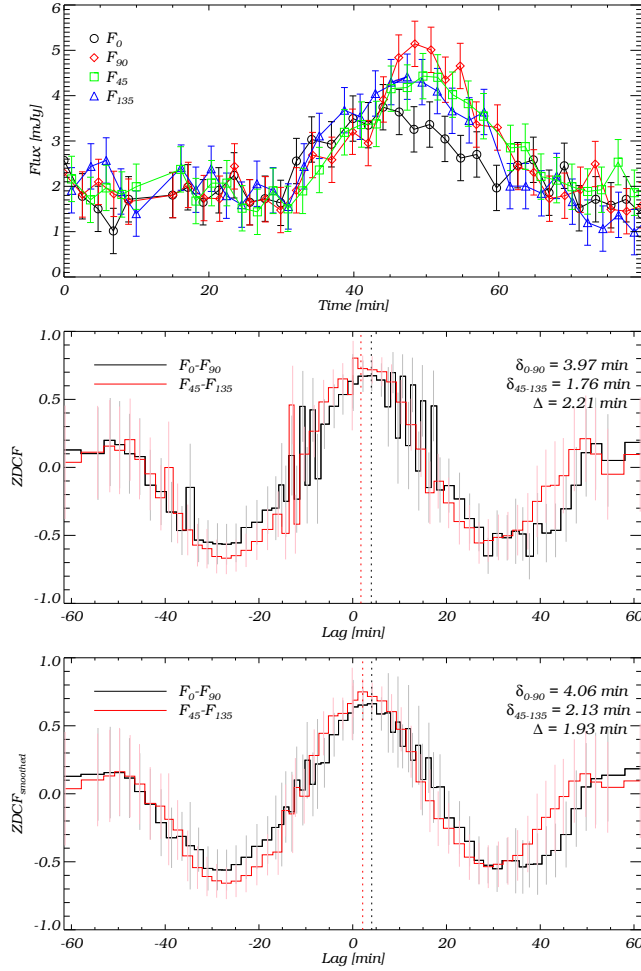


**Figure 6.7:** NIR flare event observed on 13 June 2004. Four different polarized channels indicated with different colors (top). In order to derive the time-lags a cross-correlation analysis has been performed. Maximum of two curves have been indicated with two different methods: center of weight method (middle) and smoothing (bottom). The average values of  $\delta_1 = 4.02 \pm 0.1$  min,  $\delta_2 = 1.95 \pm 0.2$  min and  $\mu = 2.45 \pm 0.5$  resulted from both analysis. One must note that the sampling rate of the observation was  $\sim 2$  min, so the level of confidence specially for the  $\delta_2$  value is low.

images in polarized flux density are taken, can be increased significantly in the following way: rather than taking data through two  $\frac{\lambda}{2}$ -plane/Wollaston-prism settings with a separation of  $45^\circ$  on the sky - in a new approach - we can take long time series through a single polarization setting only. We can change between the  $0^\circ - 90^\circ$  and  $45^\circ - 135^\circ$  configurations for consecutive nights or after significant flare events.

Figure 6.2 shows the cross-correlation between each pair of orthogonal channels. For the cross-correlation function I have followed Alexander et al. (1997, see also chapter 3). Even though both methods of the maximum-maximum difference and the cross-correlation function for determining the time-lag between channels of the simulated light curves give approximately the same answer (see Figs. 6.1 and 6.2); for the real observations we have to take into account all the effects caused by the limited number of the available data points. Figure 6.7 shows how the ZDCF of the two pairs of orthogonal channels look like for the light curves observed on 13 June 2004. Since the ZDCF is varying dramatically from point to point, it is not easy to determine the place of its maximum. Here I have applied two independent methods for doing so. First I have used the definition of the center of weight as below

$$\tau_{max} = \frac{\sum_i ZDCF(\tau_i) \times \tau_i}{\sum_i ZDCF(\tau_i)} \quad (6.2)$$

which leads to the first estimations of  $\delta_1 \equiv \delta_{0-90}$  and  $\delta_2 \equiv \delta_{45-135}$  ( $\delta_{0-90} = 3.97$  min,  $\delta_{45-135} = 1.76$  min). For the second method I have smoothed the ZDCF function so its maximum could be well estimated ( $\delta_{0-90} = 4.06$  min,  $\delta_{45-135} = 2.13$  min). One can see that the values of both methods are well in agreement with each other. Averaging the values from both methods leads to  $\delta_1 = 4.02 \pm 0.1$ min and  $\delta_2 = 1.95 \pm 0.2$ min. Furthermore, the magnification of the light curve can be constrained to  $\mu = 2.45 \pm 0.5$ . Here I must note that the sampling rate of this observation was  $\sim 2$ min, so the level of confidence specially for the  $\delta_2$  value is low. In order to improve these estimations we need high SNR images observed in polarimetry with higher time resolutions.

Although the time resolution of the available data is not less than 2 minutes, it is enough to rule out some parts of the  $a - i$  plane with high enough confidence. I have shown in Figs. 6.8 and 6.9 how one can rule out the configurations that predict values of  $\delta_1 \geq 6$  min,  $\delta_1 \leq 2$  min,  $\delta_2 \geq 4$  min,  $\delta_2 \leq 0.5$  min,  $\mu \leq 2$  and  $\mu \geq 5$ . In each image the white region shows the acceptable range of the values for  $a$  and  $i$ . Basically, one can rule out the value which is located below the contours plotted for the orbital time scale if a clear periodic signal is detectable in the light curve. I have not done so since the mentioned light curve shows no  $> 3\sigma$  QPO signal in its PSD.

As one can notice in these figures, one problem remain untouched. Where is the exact location of the orbiting blob with respect to the black hole? It is clear from the

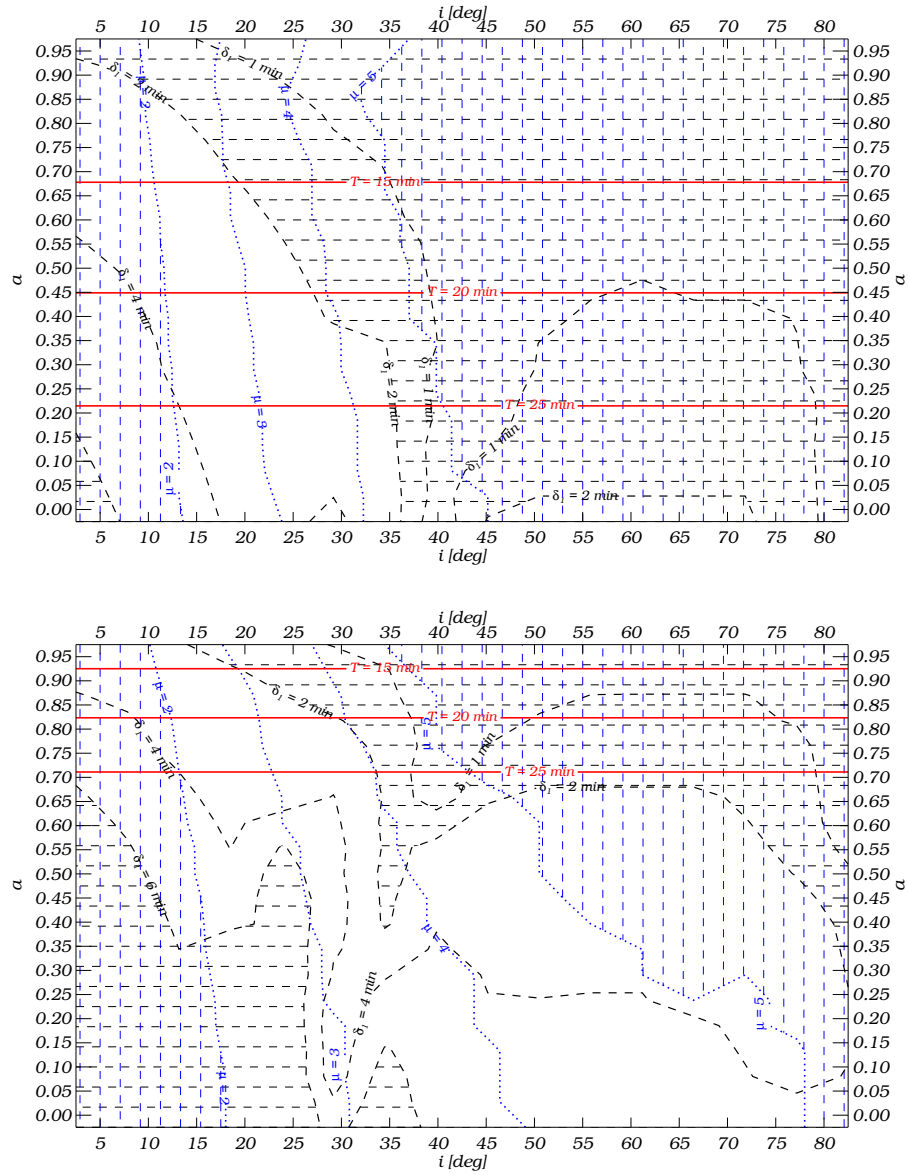


**Figure 6.8:** Over-plot of the contours of  $\delta_1$ ,  $\mu$  and  $T$  for  $pos=1.0$  (top) and  $pos=1.5$  (bottom) and a black hole of the mass  $4 \times 10^6 M_\odot$ . The areas where the values can be excluded by  $\pm 3\sigma$  level of confidence (according to the observed values in Sgr A\* NIR light curves) are shaded. The white area shows the acceptable range of values for  $a$  and  $i$ .



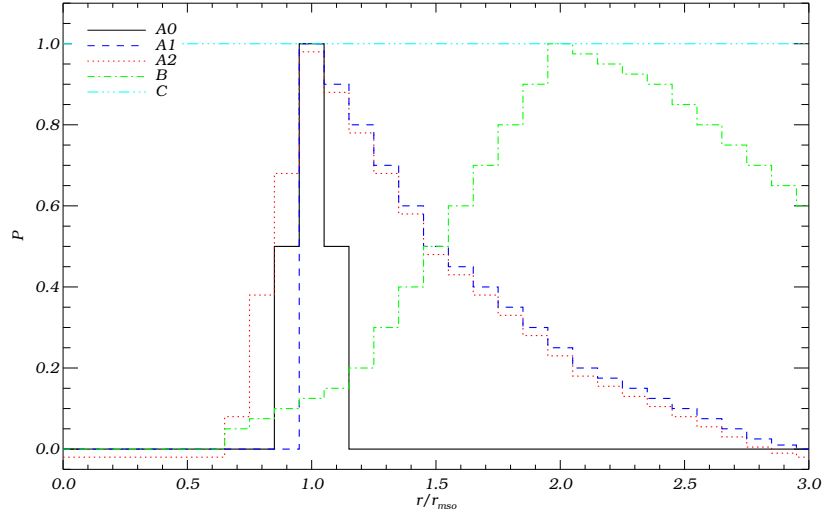


**Figure 6.10:** Normalized probability of the creation of spots inside the accretion disk as a function of distance to the black hole ( $r/r_{mso}$ ). Different curves correspond to the different assumptions: spots always created very close to the ISCO ( $A_0$ ), dominant creation happens at ISCO with a truncation below it ( $A_1$ ), or with no truncation ( $A_2$ ). The possibility that the maximum stress and energy dissipation -i.e. maximum possibility for spot creation happens at  $2r_{ms}$  (model B, see Shafee et al. 2009) or equal probability everywhere inside the disk (model C) are also considered.

images that the results are sensitive to this free parameter (see predictions for  $\text{pos}=1.0$  and  $\text{pos}=1.5$  in each image). Unfortunately, there is no direct way to constrain such a parameter. A lot of efforts have been devoted to understand where the radiation edge or the stress edge of an accretion disk are located and how they depend on the assumptions of different models (Beckwith et al. 2008, Shafee et al. 2008, Noble et al. 2009, 2010). Since it is not yet clear how and where inside an accretion disk spots can be created, I have assumed five different type of models for the probability distribution of the spots as a function of distance from the black hole (Fig. 6.10). I have considered models of which the main creation of spots happens only around the ISCO (model  $A_0$ ), distributed over the disk with the maximum at the ISCO and truncated at it (model  $A_1$ ), distributed over the disk with the maximum at the ISCO without truncation (model  $A_2$ ), distributed over the disk with the maximum at the  $2 \times r_{ms}$  without truncation (model B, see Shafee et al. 2008) and an equal distribution for the probability that spot is located somewhere inside the disk.

Figures 6.11 - 6.15 show the predictions of this time-lag analysis for each model

set-up. I have shown the contours of the  $\delta_1$ ,  $\delta_2$ ,  $\mu$  and  $T$  separately and also all over-plotted in one image. The results show how the acceptable range of values for  $a$  and  $i$  changes for different assumptions for the spatial probability distribution of the spots. The advantage of this method is that we have integrated over the probability that a spot is located somewhere inside the accretion disk, hence the predictions of the model only depend on two main parameters  $a$  and  $i$ . But we still can go one step further. Since the models I have considered cover a wide range of assumptions (mainly most physically possible scenarios) it is possible to calculate a probability distribution for the possible values of  $a$  and  $i$  derived from all five mentioned results. It is a very rough estimate for these values but it is probably the best one can achieve till the moment we reach a much better understanding of the physical processes happening very close to the black holes.

Although all I have discussed in this section was mainly about Sagittarius A\*, the main advantage of this method is its applicability for a wide range of compact sources which show QPO behavior. Since the current technical difficulties do not allow for polarimetric observations with time resolutions less than  $\sim 30$  seconds, the method is currently applicable to sources with the mass  $\gtrsim 10^6 M_\odot$ . This makes objects like RE J1034+396 perfect candidates for testing predictions of the hot spot model (Fig. 6.16). Unfortunately, there is no polarimetric observation of this source available so far. The mass of the object is also not well determined (the estimations vary from  $6.3 \times 10^5$  to  $3.6 \times 10^7 M_\odot$ ). The average magnification of the source can be estimated from the available X-ray light curves  $\bar{\mu} = 4.34 \pm 0.5$  (Fig. 6.16). This source looks to be a promising target for future NIR polarimetry if its mass estimation can be improved (using reverberation mapping for example).

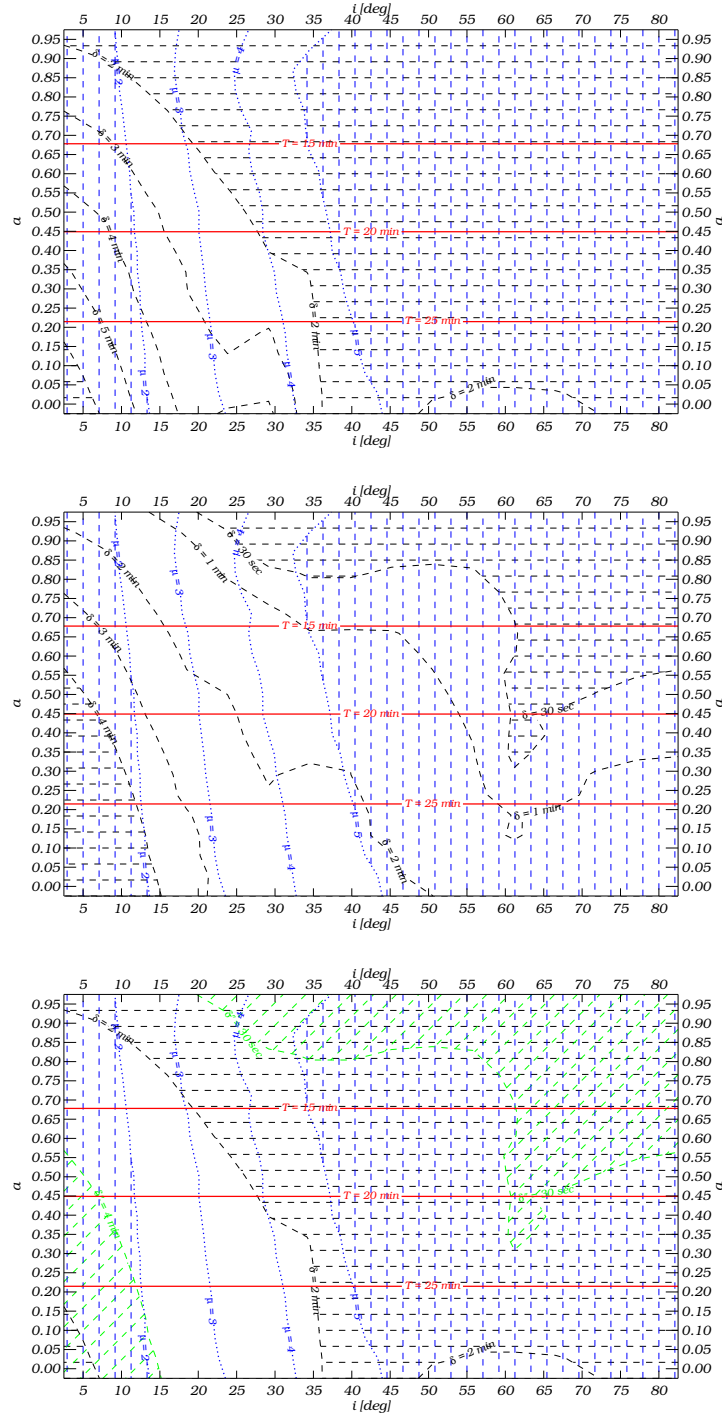


**Figure 6.11:** Over-plot of the contours of  $\delta_1$ ,  $\mu$  and  $T$  (top) and  $\delta_2$ ,  $\mu$  and  $T$  (middle) and all of them together (bottom) for the model  $A_0$ . The areas where the values can be excluded by  $\pm 3\sigma$  level of confidence (according to the observed values in Sgr A\* NIR light curves) are shaded. The white area shows the acceptable range of values for  $a$  and  $i$ .

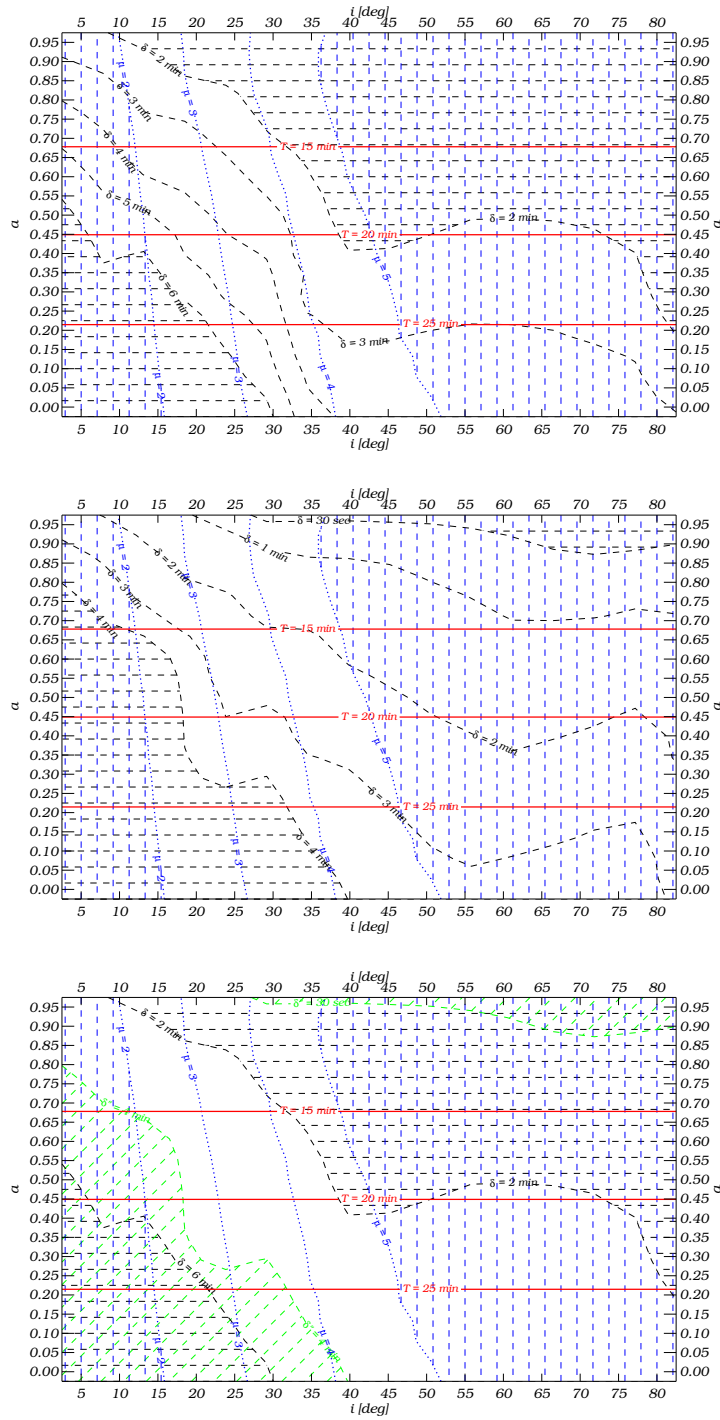


Figure 6.12: Same as Fig. 6.11 for model  $A_1$ .

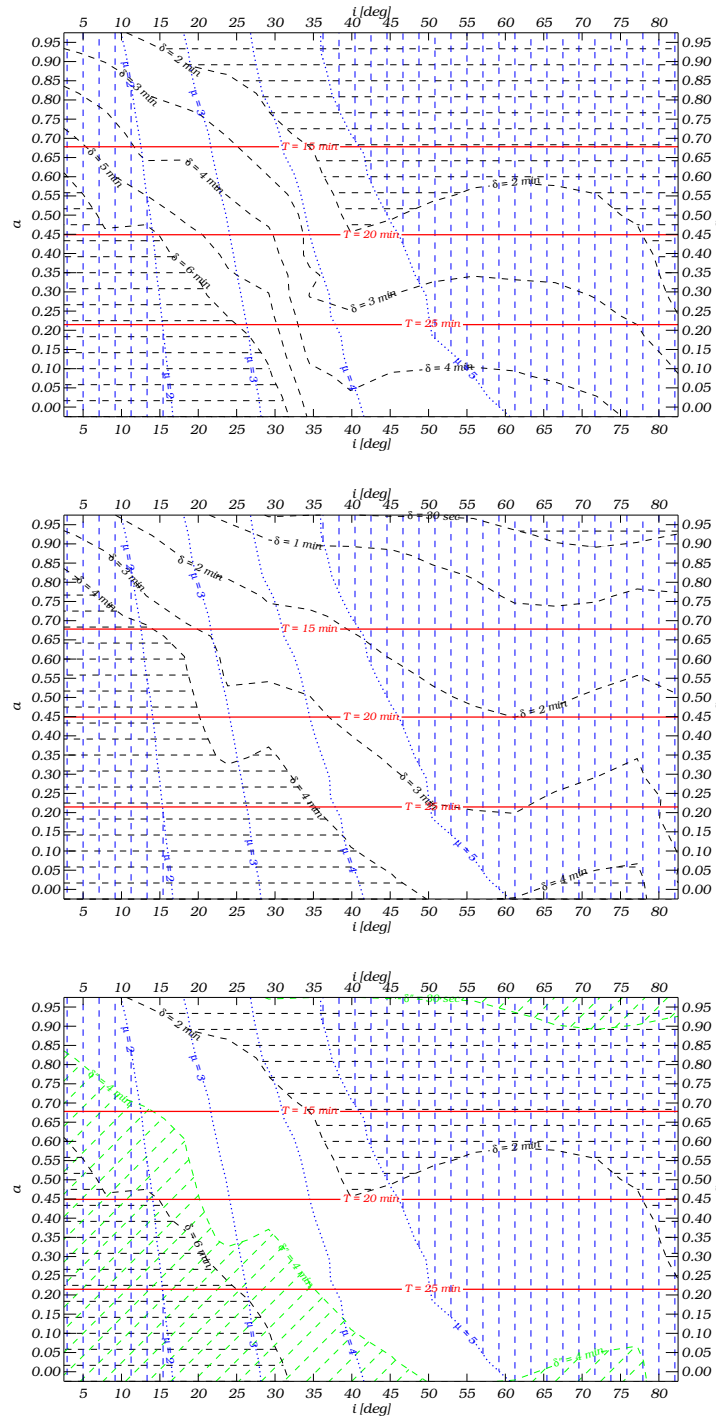


Figure 6.13: Same as Fig. 6.11 for model A<sub>2</sub>.

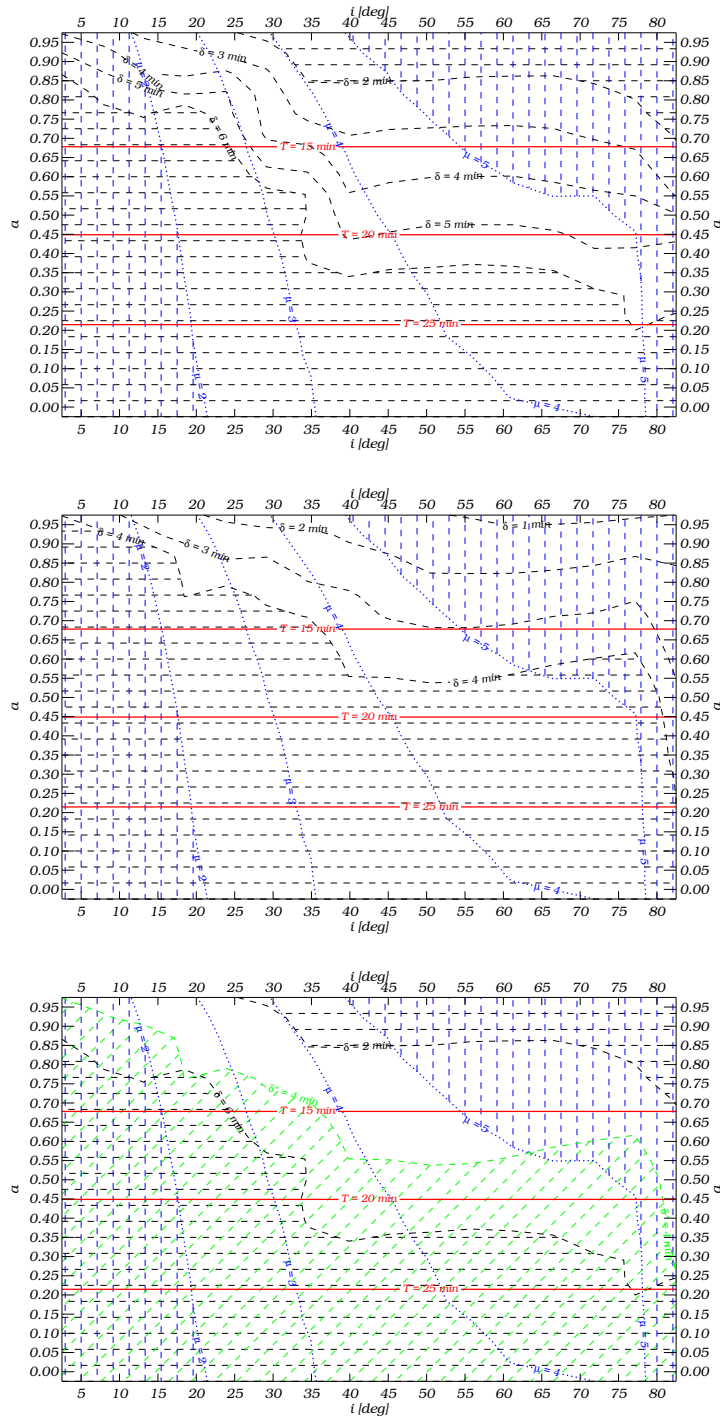


Figure 6.14: Same as Fig. 6.11 for model B.

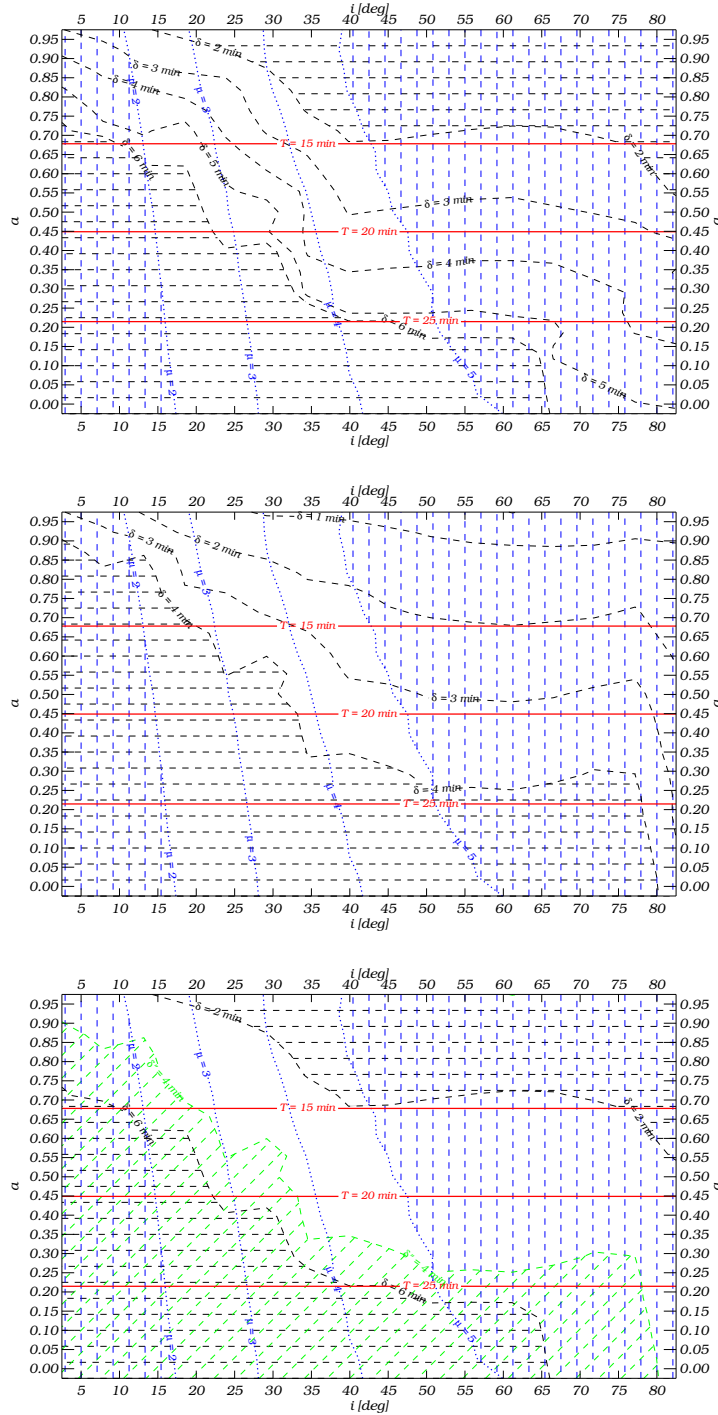
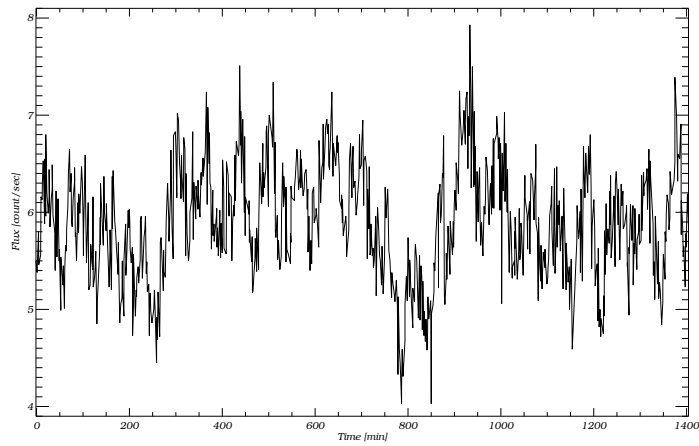


Figure 6.15: Same as Fig. 6.11 for model C.



*Figure 6.16:* X-ray light curve of RE J1034+396 shows a clear periodic signal at  $62 \pm 2$  min. There is no polarimetric observation of the source available so far. The mass of the object is also not well determined.

## Chapter 7

# Summary and Conclusion

*Up from Earth's center through the seventh Gate  
I rose, and on the throne of Saturn sate  
And many Knots unravel'd by the road  
But not the master-knot of human death and fate.*

-Omar Khayyám (1048 AD - 1131 AD)  
Astronomer, mathematician, philosopher,  
physician and poet.

I have used a sample of NIR flares of Sgr A\* observed in polarimetry mode to study the nature of the detected variability. Using the z-transformed discrete correlation function algorithm, I found a significant correlation between changes in the measured polarimetric data and total flux densities. This provides evidence that the variations probably originate from inner parts of an accretion disk while strong gravity's effects are manifested inside them.

In order to obtain this information polarization data is indispensable, since the corresponding signals are very difficult or even impossible to extract from simple total intensity light curves only (Do et al. 2008). The presence of significant signals from orbiting matter then calls for detailed modeling of the NIR polarized light curves in order to analyze the distribution of the emitting material and the magnetic field structure within the accretion disk (e.g. Eckart et al. 2006a, 2008a, Meyer et al. 2006ab, 2007).

In addition, the pattern recognition algorithm I employed in this thesis is an efficient tool to search for flare events that carry the signature of strong gravity in light curves that are significantly longer than the orbiting time scale over which such an event can typically occur. Other methods that make simultaneous use of the entire light curve (like e.g. the Lomb-Scargle algorithm) tend to dilute these signals and lower the possibility for significant detections dramatically (Do et al. 2008, Meyer et al. 2009).

In order to constrain the physical properties of the emitting region I employed a relativistic disk model with azimuthal over-densities of relativistic electrons. A combination of a synchrotron mechanism and relativistic amplifications allowed me to fit the real observed data, and make predictions about astrometric parameters of the accretion disk around Sgr A\*. The modeled light curves show the same correlation between the flux and polarimetric data that has been deduced from observations.

Simulations were carried out such that they cover a wide range of parameters, including the effects of gravitational shearing inside the accretion disk, heating and cooling time scales, inclination and spin of the black hole. I discussed how the observed swings in the polarization angle support the idea of a compact source for the emission, instead of radially extended spiral shapes. Moreover, I presented a model in which the observed NIR polarization angle can lead to confining the expected region for the possible outflow/wind from Sgr A\*. The model also predicts that when observations can possibly resolve the position of such an outflow, the magnetic field structure inside the accretion disk could be confined.

Furthermore, the centroid paths of the NIR images are discussed. In comparison with the results by Broderick & Loeb (2006a,b) and Hamaus et al. (2009), I have shown that the geometrical structure of the emitting region (elongation of the spot according to the Keplerian shearing, multi-component structures, spiral arms, confusion caused by the radiation from the hot torus) can affect the expected centroid tracks. While all the mentioned geometries are able to fit the observed fluxes, I have shown how the future NIR interferometer GRAVITY on the VLT can break these degeneracies. The results of simulations propose that focusing GRAVITY observations on the polarimetry mode could reveal a clear centroid track of the spot(s). I conclude that even though a non detection of centroid shifts can not rule out the multi-components model or spiral arms scenarios, a clear position wander in the center of NIR images during the flares will support the idea of bright long lived spots orbiting occasionally around the central black hole.

Finally, I have discussed how time resolved NIR polarimetry can very well constrain the intrinsic properties of Sagittarius A\*. I have developed a new straightforward

method for comparing the results of the model and the observations. This new method opens a new window for testing the physics very close to the edge of infinity.



# Bibliography

- [1] Abramowicz, M. A., Bao, G., Lanza, A., Zhang, X.-H., 1991, A&A 245, 454
- [2] Abramowicz, M. A., Lanza, A., Spiegel, E. A., Szuszkiewicz, E., 1992, Nature 356, 41-43
- [3] Adams, F. C., Watkins, R., 1995, ApJ v.451, 314
- [4] Aharonian, F., Akhperjanian, A. G., Anton, G., et al., 2009, A&A 503, 3, 817-825
- [5] Alexander, T., 1997, ASSL 218, 163
- [6] Arlt, R.; Rudiger, G., 2001, A&A 374, 1035
- [7] Armitage, P. J., Reynolds, C. S., 2003, MNRAS 341, 1041
- [8] Asaoka I., 1989, PASJ, 41, 763
- [9] Baganoff, F. K., Bautz, M. W., Brandt, W. N., et al., 2001, Nature, 413, 45
- [10] Baganoff, F. K., Maeda, Y., Morris, M., et al., 2003, ApJ, 591, 2, 891-915
- [11] Bao G., Hadrava P., & Østgaard E. 1994, ApJ, 435, 55
- [12] Bao G., Hadrava P., Wiita P., & Xiong Y. 1997, ApJ, 487, 142
- [13] Bardeen, J. M., Press, W. H., Teukolsky, S. A., 1972, ApJ 178, 347
- [14] Beckwith K., & Done C. 2004, MNRAS 359, 4, 1217-1228
- [15] Beckwith, K, Hawley, J. F., Krolik, J. H., 2008, MNRAS 390, 1, 21-38
- [16] Belanger, G., Terrier, R., de Jager, O. C., Goldwurm, A., Melia, F., 2006, JPhCS 54, 420
- [17] Belanger, G., Goldwurm, A., Renaud, M., 2006, ApJ, 636, 1, 275-289

- 
- [18] Blandford, R. D., 2001, Progress of Theoretical Physics Supplement 143, 182
- [19] Bondi, H., 1952, MNRAS 112, 195
- [20] Bowyer, S., Byram, E. T., Chubb, T. A., Friedman, H., 1965, Science 147, 3656, 394-398
- [21] Broderick, A. E., Loeb, A., 2006a, ApJ 636L, 109
- [22] Broderick, A. E., Loeb, A., 2006b, MNRAS 367, 905
- [23] Broderick, A.E., Loeb, A., Narayan, R., 2009, ApJ 701, 2, 1357-1366
- [24] Bromley B. C., Chen K., & Miller W. A., 1997, ApJ, 457, 57
- [25] Bromley, B. C., Melia, F., Liu, S., 2001, ApJ 555L, 83
- [26] Bursa, M., 2007, IAUS 238, 333
- [27] Čadež, A., Calvani, M., Gomboc, A., Kostić, U., 2006, AIPC 861, 566
- [28] Chan, C., Liu, S., Fryer, C. L., et al., 2006, ApJ 701, 521-534
- [29] Chan, C., 2009, ApJ 704, 68-79
- [30] Connors P. A., Stark R. F., & Piran T., 1980, ApJ, 235, 224
- [31] Cunningham, J. M., Bardeen, C. T., 1973, ApJ 183, 237
- [32] Devillard, N., 1999, ASPC 172, 333
- [33] De Villiers, J, Hawley, J. F., 2003, ApJ 589, 458
- [34] Diolaiti, E., Bendinelli, O., Bonaccini, D., et al. 2000, ASPC 216, 623
- [35] Do, T., Ghez, A. M., Morris, M. R., et al. 2009, ApJ 691, 1021
- [36] Doeleman, S. S., Fish, V. L., Broderick, A. E., Loeb, A., Rogers, A. E. E., 2009, ApJ 695, 1, 59-74
- [37] Dovčiak, M., Karas, V., Yaqoob, T., 2004, ApJS 153, 205
- [38] Dovčiak, M., Karas, V., Matt, G., Goosmann, R. W., 2008a, MNRAS 384, 361
- [39] Dovčiak, M., Muleri, F., Goosmann, R. W., Karas, V., Matt, G., 2008b, MNRAS 391, 32
- [40] Eckart, A., & Genzel, R. 1996, Nature 383, 415

- [41] Eckart, A., & Genzel, R. 1997, MNRAS 284, 576
- [42] Eckart, A., Genzel, R., Ott, T. and Schödel, R. 2002, MNRAS, 331, 917
- [43] Eckart, A., Baganoff, F. K., Morris, M., et al., 2004, A&A 427, 1
- [44] Eckart, A., Baganoff, F. K., Schödel, R., et al. , 2006a, A&A 450, 535
- [45] Eckart, A., Schödel, R., Meyer, L., et al., 2006b, A&A 455, 1
- [46] Eckart, A., Schödel, R., Meyer, L., et al., 2006c, ESO Messenger 125, 2
- [47] Eckart, A., Baganoff, F. K., Zamaninasab, M., et al., 2008a, A&A 479, 625
- [48] Eckart, A., Schödel, R., Baganoff, F. K., et al., 2008b, JPhCS 131a, 2002
- [49] Eckart, A., Schödel, R., García-Marín, M., et al., 2008c, A&A 492, 337
- [50] Eckart, A., Baganoff, F. K., Morris, M. R M., et al., 2009, A&A 500, 935-946
- [51] Edelson, R. A., Krolik, J. H., 1988, Astrophysical Journal 333, 646-659
- [52] Einstein, A. 1916, Annalen der Physik 49, 769
- [53] Eisenhauer, F., Schödel, R., Genzel, R., et al. 2003, ApJ 597, L121
- [54] Eisenhauer, F., Genzel, R., Alexander, T., 2005a, ApJ 628, 246
- [55] Eisenhauer, F., Perrin, G., Rabien, S., et al. 2005b, AN 326, 561
- [56] Eisenhauer, F., Perrin, G., Brandner, W., et al. 2008, SPIE 7013E, 69
- [57] Falanga, M., Melia, F., Tagger, M., Goldwurm, A., Bélanger, G., 2007, ApJ 662L, 15
- [58] Falanga, M., Melia, F., Prescher, M., Bélanger, G., Goldwurm, A., 2008, ApJ 679L, 93
- [59] Falcke, H, Goss, W. M.; Matsuo, H, 1998, Astrophysical Journal 499, 731
- [60] Falcke, H., Melia, F., Agol, E., 2000, ApJ 528L, 13
- [61] Ferrarese, L., and D. Merritt, 2000, ApJL 539, L9
- [62] Fisher, R. A., 1921, Metron 1, 4, 1
- [63] Fukumura, K., Kazanas, D., Stephenson, G., 2009, ApJ 695, 2, 1199-1209
- [64] Gabuzda, D.C.; Cawthorne, T.V., 2000, MNRAS 319, 1056

- [65] Genzel, R., Eckart, A., Ott, T., & Eisenhauer, F., 1997, MNRAS 291, 1, 219-234
- [66] Genzel, R., Schödel, R., Ott, T., et al., 2003, Nature, 425, 934
- [67] Ghez, A., Morris, M., Becklin, E.E., Tanner, A. & Kremenek, T., 2000, Nature 407, 349
- [68] Ghez, A. M., Becklin, E., Duchjne, G., et al., AN, Supplementary Issue 1, Proceedings of the Galactic Center Workshop 2002, 527-533
- [69] Ghez, A. M., Wright, S. A., Matthews, K., et al., 2004, ApJ 601, 2, L159-L162
- [70] Ghez, A. M., Salim, S., Hornstein, S. D., et al., 2005a, ApJ 620, 744
- [71] Ghez, A. M., Hornstein, S. D., Lu, J. R., et al., 2005b, ApJ 635, 1087
- [72] Giacconi, R., Gursky, H., Paolini, F.R., and Rossi B.B., 1962, PRL 9, 439-443
- [73] Gierliński, M., Middleton, M., Ward, M., Done, C., 2008, Nature 455, 369
- [74] Gillessen, S., Perrin, G., Brandner, W., et al. 2006, JPhCS 54, 411
- [75] Gillessen, S., Eisenhauer, F., Trippe, S., et al. 2009, ApJ 692, 1075
- [76] Glindemann, A., Abuter, R., Carbognani, F., et al., 2000, Proc. SPIE Vol. 4006, 2-12
- [77] Goggin, L. M., 2008, PhD Thesis, California Institute of Technology
- [78] Gould, R.J., 1979, A&A 76, 306
- [79] Hamaus, N., Paumard, T., Müller, T., et al. 2009, ApJ 692, 902
- [80] Hawley, J. F., Balbus, S. A., 1991, ApJ 376, 223
- [81] Hirose, S., Krolik, J. H., De Villiers, J.-P., Hawley, J. F., 2004, ApJ, 606, 1083
- [82] Hollywood, J. M., Melia, F., Close, L. M., McCarthy, D. W. Jr., Dekeyser, T. A., 1995, ApJ 448L, 21
- [84] Hornstein, S. D., Ghez, A. M., Tanner, A., et al., 2002, ApJ 577, 1, L9-L13
- [84] Hornstein, S. D., Matthews, K., Ghez, A. M., et al. 2007 ApJ 667, 900
- [85] Karas, V. & Bao, G., 1992, A&A 257, 531
- [86] Karas, V., Vokrouhlicky, D., Polnarev, A. G., 1992, MNRAS 259, 569

- 
- [87] Karas V., Dovčiak M., Eckart A., Meyer L. 2007, in Proceedings of the Workshop on the Black Holes and Neutron Stars, 99-108 [arXiv:0709.3836]
- [88] Kerr, R. P., 1963, PRL 11, 237-238
- [89] Kojima Y. 1991, MNRAS, 250, 629
- [90] Kormendy, J., Gebhardt, K., 2001, Relativistic Astrophysics: 20th Texas Symposium. AIP Conference Proceedings 586, 363-381
- [91] Kostić, U., Čadež, A., Calvani, M., Gomboc, A., 2009, [arXiv:0901.3447]
- [92] Krolik, J. H., Hawley, J. F., 2002, ApJ 573, 754
- [93] Laor A. 1991, ApJ, 376, 90
- [94] Liu, Siming, Melia, F., 2002, ApJ 566L, 77
- [95] Liu, S., Melia, F., Petrosian, V., 2006, ApJ 636, 798
- [96] Liu, S.; Qian, L.; Wu, X.-B.; Fryer, C.L., Li, H., 2007, ApJ 668, 2, L127-L130
- [97] Luminet, J.-P., 1979, A&A 75, 1-2, 228-235.
- [98] Lynden-Bell, D., & Sanitt, N., 1969, MNRAS 143, 167
- [99] Lyubarskii, Y. E., 1997, MNRAS 292, 679
- [100] Maeda, Y., Baganoff, F. K., Feigelson, E. D., 2002, ApJ 570, 2, 671-687
- [101] Markoff, S., Falcke, H., Yuan, F., Biermann, P. L., 2001, A&A 379L, 13
- [102] Markoff, S., Nowak, M.A., Wilms, J., 2005, ApJ 635, 1203
- [103] Markoff, S., Bower, G.C.; Falcke, H., 2007, MNRAS 379, 4, 1519-1532
- [104] Marrone, D.P.; Moran, J.M.; Zhao, J.-H.; Rao, R., 2007, ApJ 654, L57
- [105] Marrone, D. P., Baganoff, F. K., Morris, M., et al., 2008, ApJ 682, 373
- [106] Marscher, A.P. 1983, ApJ, 264, 296
- [107] Martocchia A., Karas V., & Matt G. 2000, MNRAS, 312, 817
- [108] Mashoon, B., 1973, PRD 7, 2807
- [109] Matt G., Fabian A. C., & Ross R. R. 1993, MNRAS, 264, 839
- [110] Mauerhan, J.C.; Morris, M.; Walter, F.; Baganoff, F.K., 2005, ApJ 623 L25

- 
- [111] Melia, F., Bromley, B. C., Liu, S., Walker, C. K., 2001, *ApJ* 554, 37
- [112] Melia, F., *The Galactic Supermassive Black Hole*, Princeton University Press, 2007
- [113] Meyer, L., Eckart, A., Schödel, R., et al., 2006a, *A&A* 460, 15
- [114] Meyer, L., Schödel, R., Eckart, A., et al., 2006b, *A&A* 458, L25
- [115] Meyer, L., Schödel, R., Eckart, A., et al., 2007, *A&A* 473, 707
- [116] Meyer, L., Do, T., Ghez, A., et al., 2009, *ApJL* 694, 1, L87-L91
- [117] Mužić, K., Eckart, A., Schödel, R., Meyer, L., Zensus, A., 2007, *A&A* 469, 993
- [118] Nayakshin, S., Cuadra, J., Sunyaev, R., 2004, *A&A* 413, 173
- [119] Newman, E. T., Couch, E., Chinnapared, K., et al., *Journal of Mathematical Physics* 6, 918-919
- [120] Nishiyama, S., Tamura M., Hatano, H., 2009, *ApJL* 702, L56-L60
- [121] Noble, S. C., Krolik, J. H., Hawley, J. F., 2009, *ApJ* 692, 1, 411-421
- [122] Noble, S. C., Krolik, J. H., Hawley, J. F., 2010, [arXiv:1001.4809]
- [123] Nordström, G., 1918, *Proc. Acad. Sci. Amsterdam* 20, 1238
- [124] Novikov, I.D. & Thorne, K.S., 1973, in *Black Holes*, eds. C. De Witt and B. De Witt (New York: Gordon & Breach), 343
- [125] Nowak, M. A., Lehr, D. E., 1998 npad.conf, 233
- [126] Palmer, D.M. 2009, *ApJ* 695, 496-502
- [127] Papa, M. A., Schutz, B. F., Sintes, A. M., *Proceedings of the conference "Gravitational waves: a challenge to theoretical astrophysics"*, ICTP Lecture Notes Series
- [128] Paumard, T., Eisenhauer, F., Genzel, R., et al. 2006, via conf., 257
- [129] Pecháček, T., Karas, V., Czerny, B., 2008, *A&A* 487, 815
- [130] Pollack, L. K.; Taylor, G. B.; Zavala, R. T., 2003, *ApJ* 589, 733
- [131] Porquet, D., Predehl, P., Aschenbach, et al. 2003, *A&A* 407, L17
- [132] Porquet, D., Grosso, N., Predehl, P., et al. 2009, *A&A* 488, 49

- 
- [133] Press, W. H., Rybicki, G. B., 1989, ApJ 338, 277
- [134] Press, W. H., Flannery, B. P. Teukolsky, S., Vetterling, W. T. 1988, CAMBRIDGE UNIVERSITY PRESS, 733
- [135] Priestly, M.B., 1989, Spectral Estimation and Time Series, San Diego: Academic Press, 389
- [136] Qian, L., Abramowicz, M. A., Fragile, P. C., et al. 2009, A&A 498, 2, .471-477
- [137] Quataert, E., 2003, AN 324, Special Supplement "The central 300 parsecs of the Milky Way", 435
- [138] Reid, M. J., Broderick, A. E., Loeb, A., Honma, M., Brunthaler, A., 2008, ApJ 682, 1041
- [139] Reissner, H., 1916, Ann. Physik 50, 106
- [140] Rusk, R.E., Thesis (Ph.D.), University of Toronto (Canada), 1988
- [141] Sabha, N., Witzel, G., Eckart, et al., accepted for publication in A&A [arXiv:1001.1351]
- [142] Shafee, R., Narayan, R., McClintock, J. E., 2008, ApJ 676, 1, 549-561
- [143] Shakura, N. I. & Sunyaev, R. A., 1973, A&A, 24, 337 - 355
- [144] Schmidt, M., 1963, Nature 197, 1040
- [145] Schnittman, J.D., 2005, Ph.D dissertation, 2005, MIT, Publication Number: AAT 0808149. DAI-B 66/05
- [146] Schnittman, J. D., Krolik, J. H., Hawley, J. F., 2006, ApJ 651, 1031
- [148] Schödel, R., Ott, T., Genzel, R., et al., 2002, Nature 419, 694
- [148] Schödel, R., Eckart, A., Alexander, T., et al., 2007, A&A 469, 125
- [149] Schulz, M., Mudelsee, M., 2002, Computers & Geosciences 28, 3
- [150] K. Schwarzschild, 1916, Sitzungsber. Preuss. Akad. Wiss., Phys. Math. Kl. 189
- [152] Tagger, M., Melia, F., 2006, ApJ 636L, 33
- [152] Timmer, J., König, M., 1995, A&A 300, 707
- [153] Thorne, K. S., Black holes and time warps : Einstein's outrageous legacy, 1994, Norton & Company

- 
- [154] Trippe S., 2007, proceeding of the Workshop "Celebrating 15 years of precision astronomy in the Galactic Center" (Ringberg Castle), Bavaria, Germany
- [155] van der Klis, M., 1989, Annual Review of Astronomy and Astrophysics 27 (A90-29983 12-90), 517-553
- [156] Vaughan, S., Edelson, R., Warwick, R. S., Uttley, P., 2003, MNRAS 345, 1271
- [157] Vaughan, S., Uttley, P., 2005, MNRAS 362, 1, 235-244
- [158] Vaughan, S. 2010, MNRAS 402, 1, 307-320
- [159] Viergutz S. U. 1991, A&A, 272, 355
- [160] Witzel, G., 2008, Diploma Thesis, University of Cologne
- [161] Yuan, F., Markoff, S., Falcke, H., 2002, A&A 383, 854
- [162] Yuan, F., Quataert, E. & Narayan, R., 2003, ApJ, 598, 301
- [163] Yuan, F., Quataert, E. & Narayan, R., 2004, ApJ 606, 894
- [164] Yusef-Zadeh, F., Wardle, M., Rho, J., Sakano, M., 1998, ApJ 585, 1, 319-323
- [165] Yusef-Zadeh, F., Bushouse, H., Dowell, C. D., et al., 2006a, ApJ 644, 198
- [166] Yusef-Zadeh, F., Roberts, D., Wardle, M., Heinke, C. O., Bower, G. C., 2006b, ApJ 650, 189
- [167] Yusef-Zadeh, F., Wardle, M., Cotton, W. D., Heinke, C. O., Roberts, D. A., 2007, ApJ 668, 47
- [168] Yusef-Zadeh, F., Wardle, M., Heinke, C., et al. 2008, ApJ 682, 361
- [169] Yusef-Zadeh, F., Bushouse, H., Wardle, M., et al., 2009, ApJ 706, 1, 348-375
- [170] Zakharov A. F. 1994, MNRAS, 269, 283
- [171] Zamaninasab, M., Eckart, A., Kunneriath, D., et al., 2008a, MmSAI 79, 1054
- [172] Zamaninasab, M., Eckart, A., Meyer, L., et al., 2008b, JPhCS 131a
- [173] Zamaninasab, M., Eckart, A., Witzel, G., et al., 2010, A&A 510, id.A3
- [174] Zylka, R., Mezger, P. G., Ward-Thompson, D., Duschl, W. J., Lesch, H., 1995, A&A 297, 1, 83-97

# List of Figures

1.1	Specific radii in the equatorial plane of a Kerr black hole . . . . .	11
1.2	X-ray image of Cygnus X-1 . . . . .	13
1.3	Jet of the Radio Galaxy M87 . . . . .	14
1.4	GC in optical, NIR and X-ray . . . . .	15
1.5	X-ray image of Sgr A* . . . . .	16
1.6	H, K and $L'$ band composite image of the GC . . . . .	17
1.7	Orbit of star S2 (1992-2002) . . . . .	18
1.8	Orbit of star S2 (1992-2008) . . . . .	19
1.9	SED of Sgr A* . . . . .	20
1.10	NIR flaring of Sgr A* . . . . .	22
2.1	VLT and Subaru . . . . .	26
2.2	Sgr A* observed in different polarization channels . . . . .	27
2.3	Sgr A* observed by CIAO . . . . .	29
2.4	Sample of NIR light curves of Sgr A* . . . . .	30

3.1	Simulated white noise light curves . . . . .	37
3.2	Simulated flicker noise light curves . . . . .	38
3.3	Simulated red noise light curves . . . . .	39
3.4	RE J1034+396 X-ray light curve . . . . .	41
3.5	Timing analysis of RE J1034+396 X-ray light curve . . . . .	42
3.6	Timing analysis of 16 June 2003 light curve . . . . .	43
3.7	Timing analysis of 30-31 July 2005 light curve . . . . .	44
3.8	Timing analysis of 1-7 April 2007 light curve . . . . .	45
3.9	Sample of light curves of Sgr A* (flux only) . . . . .	46
3.10	ZDCF of the flux light curves of the sample . . . . .	48
3.11	ZDCF of $10^4$ simulated red noise light curves . . . . .	49
3.12	Lomb-Scargle periodograms for the flux light curves (1) . . . . .	50
3.13	Lomb-Scargle periodograms for the flux light curves (2) . . . . .	51
3.14	Averaged Lomb-Scargle periodograms . . . . .	52
3.15	Averaged and binned Lomb-Scargle periodograms . . . . .	53
3.16	Cross-correlation between the flux and polarization angle (degree) light curves of Fig. 2.4 . . . . .	55
3.17	Simulated noise light curves of four different polarimetric channels . . . . .	57
3.18	Sketch showing the derivation of the cross-correlations . . . . .	58
3.19	Probability of a significant correlation detection for the simulated noise and observation . . . . .	59

---

4.1	Diagnostic diagrams for two representative synchrotron models . . . . .	68
4.2	Distribution of angular momentum on the equatorial plane of the accretion disk . . . . .	72
4.3	Orbital time scale on the equatorial plane of the accretion disk . . . . .	73
4.4	The geometry used for the emission model . . . . .	76
4.5	Content of the KY data tables . . . . .	77
4.6	Contour levels of relativistic factors ( $a = 0$ ) . . . . .	78
4.7	Contour levels of relativistic factors ( $a = 1$ ) . . . . .	79
4.8	Images of an optically thick standard accretion disk (1) . . . . .	81
4.9	Images of an optically thick standard accretion disk (2) . . . . .	82
4.10	Snapshots of an orbiting anomaly inside the accretion disk (1) . . . . .	83
4.11	Snapshots of an orbiting anomaly inside the accretion disk (2) . . . . .	84
4.12	Flux modulations of an evolving perturbation . . . . .	85
4.13	Light curves for a spot on circular orbit close to the black hole . . . . .	88
4.14	Cross correlation between changes in flux and polarization light curves . . . . .	89
4.15	A sketch showing the definition of the pattern recognition coefficient . . . . .	90
4.16	Pattern recognition coefficients as functions of time . . . . .	91
4.17	A selected 100 minutes window of the simulated light curves . . . . .	92
4.18	Snapshots for multi-component scenario . . . . .	93
4.19	Same as Fig. 4.17 for the multi component scenario . . . . .	94
4.20	Simulated light curves at $2.2 \mu\text{m}$ and $3.8 \mu\text{m}$ . . . . .	97

---

4.21	Flare rate as a function of flare amplitude . . . . .	98
4.22	Light curve of the 31 August 2004 X-ray flare . . . . .	101
4.23	Levels of light-travel time . . . . .	102
4.24	Snapshots of the orbiting spiral pattern . . . . .	103
4.25	Light curves resulted from a spiral pattern or a compact spot . . . . .	104
4.26	Contour graphs showing the changes in polarization . . . . .	105
4.27	A sketch of the model of two extreme cases of global magnetic field configuration . . . . .	106
4.28	Best fit achieved for the flux and polarization angle of 30 July 2005 flare	107
4.29	The resulting orientations for the direction of a possible collimated out-flow from Sgr A* . . . . .	108
5.1	VLTI . . . . .	112
5.2	The centroid motion of NIR images (1) . . . . .	114
5.3	The centroid motion of NIR images (2) . . . . .	115
5.4	The centroid motion of NIR images for polarimetric observations . . . . .	117
6.1	Total flux magnification and the corresponding 4 orthogonal polarization channels . . . . .	121
6.2	Cross-correlation between orthogonal channel light curves . . . . .	122
6.3	Time-lag between $0^\circ$ and $90^\circ$ channels . . . . .	123
6.4	Time-lag between $45^\circ$ and $135^\circ$ channels . . . . .	124
6.5	Flux magnification ( $\mu$ ) as a function of spin and inclination . . . . .	125

---

6.6	Orbital time scale ( $T$ ) as a function of spin and inclination . . . . .	126
6.7	NIR flare event observed on 13 June 2004 . . . . .	127
6.8	Over-plot of the contours of $\delta_1$ , $\mu$ and $T$ . . . . .	129
6.9	Over-plot of the contours of $\delta_2$ , $\mu$ and $T$ . . . . .	130
6.10	Normalized probability of the creation of spots as a function of distance to the black hole . . . . .	131
6.11	Over-plot of the contours of $\delta_1$ , $\mu$ and $T$ . . . . .	133
6.12	Same as Fig. 6.11 for model $A_1$ . . . . .	134
6.13	Same as Fig. 6.11 for model $A_2$ . . . . .	135
6.14	Same as Fig. 6.11 for model B. . . . .	136
6.15	Same as Fig. 6.11 for model C. . . . .	137
6.16	X-ray light curve of RE J1034+396 . . . . .	138



# List of Tables

2.1	Observations log . . . . .	31
4.1	Input parameters for the synchrotron and SSC models . . . . .	66
4.2	Final parameters resulting from least $\chi_{red}^2$ fit to the NIR flare observed on 30 July 2005 . . . . .	110



# List of Acronyms

$A_K$	Extinction in K-band
ADAF	Advection Dominated Accretion Flow
AGN	Active Galactic Nucleus
AO	Adaptive Optics
AR1	First Order Autoregressive Function
BH	Black Hole
CONICA	High Resolution IR Camera and Spectrometer
CIAO	Coronagraphic Imager with Adaptive Optics
DCF	Discrete Correlation Function
ESO	European Southern Observatory
FOV	Field of view
FWHM	Full Width at Half Maximum
GC	Galactic Center
GR	General Relativity
GRAVITY	General Relativity Analysis via VLT InTerferometrY
HFQPO	High-frequency Quasi-Periodic Oscillation
HST	Hubble Space Telescope
ISCO	Innermost Stable Circular Orbit, also: marginally stable orbit
IR	Infrared
Keck	W. M. Keck Observatory, two 10m telescopes
KY	Ray tracing code by Dovciak et al. (2004)
LR	Lucy-Richardson
MBH	Massive Black Hole
MHD	Magneto-Hydrodynamics
MRI	Magneto Rotational Instability
MSO	Marginally Stable Orbit
NACO	NAOS/CONICA adaptive optics device/near-infrared camera at the VLT
NAOS	Nasmyth Adaptive Optics System

---

NICMOS	Near Infrared Camera and Multi-Object Spectrometer (on board of the HST)
NIR	Near-infrared
PSD	Power Spectral Density
PSF	Point Spread Function
QPO	Quasi-Periodic Oscillation
RIAF	Radiatively Inefficient Accretion Flow
SED	Spectral energy distribution
Sgr A*	Sagittarius A*
SMBH	Supermassive Black Hole
SNR	Signal to noise ratio
SSC	Synchrotron Self Compton
UV	Ultraviolet
VLA	Very Large Array
VLBA	Very Long Baseline Array
VLBI	Very Long Baseline Interferometry
VLT	Very Large Telescope
VLTI	Very Large Telescope Interferometry
ZDCF	z-transformed Discrete Correlation Function

# Acknowledgements

I would like to express my gratitude and to thank all the people who supported and inspired me during my thesis work and without whom this thesis would not be possible.

First of all, I would like to thank my supervisor Prof. Andreas Eckart for all the support during the last years. I would also like to thank Rainer Schödel and Macarena García-Marín for being such great friends and all of their kind guidance. I am also grateful to Leo Meyer for all his support during my first months in Cologne. I specially like to say thanks to Prof. Vladimir Karas and Michal Dovčiak for all the enjoyable and inspiring scientific discussions that we had. I would like to thank them for their hospitality. Parts of this work was done during my stays in Prague, which were financially supported by the Czech Academy of Science and also the exchange program between Charles University of Prague and University of Cologne.

I would like to thank the entire *aegroup* for the enjoyable working atmosphere and help. Specially, Christian Straubmeier, Jens Zuther, Steffen Rost and Sebastian Fischer for all the technical support. I am grateful to all the Ph1 secretaries for making my life in Cologne easier.

This work was financially supported by the International Max Planck Research School (IMPRS) for Astronomy and Astrophysics at the MPIfR and the Universities of Bonn and Cologne. I would like to thank my co-referee Prof. A. Zensus for his time and support. I specially like to express my gratitude to Gabi Breuer for all her efforts. I am also grateful to Eduardo Ros and Simone Pott. Also thanks to my friend Miguel Requena Torres for all the fun times in Bonn.

I would like to thank my friends in Cologne: all the residence of the *girls office*, Monica Valencia-Schneider, Sabine König, Devaky Kunneriath and Nadeen Sabha for their *Gastfreundschaft* during the *coffee times*. A big thanks goes to my fellow residents of the (former!) *Republic of Montenegro*: Frau Dr. Mužić, Devaaaky Kunaariath,

Gunther Witzel and Rene Gießübel (integrated German residents). Thank you Kora for introducing me to the colorful world of IDL; I am sure you can see your footprints in all colorful images of this thesis.

My special thanks to Behrang Jalali, Atefeh Motalebi and Shahlaa Mohammadi for being my best friends. Nadeen! *Shokran Jazeelan le Kollo Shaay!!*. Last but not least, I wish to thank my parents and my brother for everything: *Merci baraye hame chiz!!*.

# Erklärung

Ich versichere, daß ich die von mir vorgelegte Dissertation selbständig angefertigt, die benutzten Quellen und Hilfsmittel vollständig angegeben und die Stellen der Arbeit – einschließlich Tabellen, Karten und Abbildungen –, die anderen Werken im Wortlaut oder dem Sinn nach entnommen sind, in jedem Einzelfall als Entlehnung kenntlich gemacht habe; daß diese Dissertation noch keiner anderen Fakultät oder Universität zur Prüfung vorgelegen hat; daß sie – abgesehen von unten angegebenen Teilpublikationen – noch nicht veröffentlicht worden ist sowie, daß ich eine solche Veröffentlichung vor Abschluß des Promotionsverfahrens nicht vornehmen werde. Die Bestimmungen dieser Promotionsordnung sind mir bekannt. Die von mir vorgelegte Dissertation ist von Prof. Dr. Andreas Eckart betreut worden.

Köln, 08.02.2010

## Teilpublikationen

- **Zamaninasab, M.**, Eckart, A., Witzel, G., Dovciak, M., Karas, V., Schödel, R., Gießübel, R., Bremer, M., García-Marín, M., Kunneriath, D., Mužić, K., Nishiyama, S., Sabha, N., Straubmeier, C. and Zensus, A: "*Near Infrared Flares of Sagittarius A\*: Importance of Near Infrared Polarimetry*", A&A 510, A3 (2010) [arXiv:0911.4659v1].
- **Zamaninasab, M.**, Eckart, A., Meyer, L., Schödel, R., Dovciak, M., Karas, V., Kunneriath, D., Witzel, G., Gießübel, R., König, S., Straubmeier, C., Zensus, A.: "*An evolving hot spot orbiting around Sgr A\**", JoP: Conference Series, Volume 131, Issue 1, 2008.
- **Zamaninasab, M.**, Eckart, A., Kunneriath, D., Witzel, G., Schödel, R., Meyer, L., Dovciak, M., Karas, V., König, S., Krichbaum, T., Lu, R. S., Straubmeier, C., Zensus,

J. A.: *"Flares of Sgr A\*: from X-ray to mm"*, Memorie della Societa Astronomica Italiana, volume 79, 1054, 2008.

- **Zamaninasab, M.**, Eckart, A. Witzel, G., Dovciak, M., Karas, V., Schödel, R., Gießübel, R., Bremer, M., García-Marín, M., Kunneriath, D., Mužić, K., Nishiyama, S., Sabha, N., Straubmeier, C. and Zensus, A.: *"Near infrared polarimetry as a tool for testing the properties of radiation from Sagittarius A\*"*, to be published in "The Galactic Center: a Window to the Nuclear Activity of Disk Galaxies", eds. Mark Morris et al., Astron. Soc. Pacific, 2010.
- Eckart, A., Baganoff, F. K., **Zamaninasab, M.**, Morris, M. R., Schödel, R., Meyer, L., Muzic, K., Bautz, M. W., Brandt, W. N., Garmire, G. P., Ricker, G. R., Kunneriath, D., Straubmeier, C., Duschl, W., Dovciak, M., Karas, V., Markoff, S., Najarro, F., Mauerhan, J., Moultaqa, J., Zensus, A.: *"Polarized NIR and X-ray flares from Sagittarius A\*"*, A&A 479, 3, 2008.
- Eckart, A., Baganoff, F. K., Morris, M. R., Kunneriath, D., **Zamaninasab, M.**, Witzel, G., Schödel, R., García-Marín, M., Meyer, L., Bower, G. C., Marrone, D., Bautz, M. W., Brandt, W. N., Garmire, G. P., Ricker, G. R., Straubmeier, C., Roberts, D. A., Mužić, K., Mauerhan, J. and Zensus, A.: *"Modeling mm- to X-ray flare emission from Sagittarius A\*"*, A&A 500, 3, 2009.
- Eckart, A., Schödel, R., García-Marín, M., Witzel, G., Weiss, A., Baganoff, F. K., Morris, M. R., Bertram, T., Dovciak, M., Duschl, W. J., Karas, V., König, S., Krichbaum, T. P., Krips, M., Kunneriath, D., Lu, R.-S., Markoff, S., Mauerhan, J., Meyer, L., Moultaqa, J., Mužić, K., Najarro, F., Pott, J.-U., Schuster, K. F., Sjouwerman, L. O., Straubmeier, C., Thum, C., Vogel, S. N., Wiesemeyer, H., **Zamaninasab, M.**, Zensus, J. A.: *"Simultaneous NIR/sub-mm observation of flare emission from Sagittarius A\*"*, A&A 492, 2, 2009.

### Weitere Publikationen

- Muzic, K., Eckart, A., Schödel, R., Buchholz, R., **Zamaninasab, M.**, and Witzel, G.: *"Cometary shaped sources at the Galactic Center: Probing the wind from the central 0.2 pc"*, submitted to A&A.
- Sabha, N., Witzel, G., Eckart, A., Buchholz, R. M., Bremer, M., Gießübel,

R., García-Marín, M., Kunneriath, D., Muzic, K., Schödel, R., Straubmeier, C., **Zamaninasab, M.**, and Zernickel, A.: "*The Extreme Luminosity States of Sagittarius A\**", accepted for publication in A&A.

- García-Marín, M., Eckart, A., Weiss, A., Witzel, G., Bremer, M., **Zamaninasab, M.**, Morris, M. R., Schödel, R., Kunneriath, D., Nishiyama, S., Baganoff, F., Dovciak, M., Sabha, N., Duschl, W. J., Moulataka, J., Karas, V., Najarro, F., Muzic, K., Straubmeier, C., Vogel, S., Krips, M., and Wiesemeyer, H.: "*Extended sub-mm emission of the Galactic center and NIR/sub-mm variability of its super-massive black hole*", submitted to A&A.

- Kunneriath, D., Witzel, G., Eckart, A., **Zamaninasab, M.**, Gießübel, R., Schödel, R., Baganoff, F.K., Morris, M. R., Dovciak, M., Duschl, W.J., García-Marín, M., Karas, V., König, S., Krichbaum, T. P., Krips, M., Lu, R.-S., Mauerhan, R., Moulataka, J., Muzic, K., Sabha, N., Najarro, F., Pott, J.-U., Schuster, K. F., Sjouwerman, L. O., Straubmeier, C., Thum, C., Vogel, S. N., Teuben, P., Weiss, A., Wiesemeyer, H., Zensus, J. A.: "*Coordinated NIR/mm observations of flare emission from Sagittarius A\**", submitted to A&A.

- Kunneriath, D., Eckart, A., Vogel, S., Sjouwerman, L., Wiesemeyer, H., Schödel, R., Baganoff, F. K., Morris, M., Bertram, T., Dovciak, M., Dowries, D., Duschl, W. J., Karas, V., König, S., Krichbaum, T., Krips, M., Lu, R.-S., Markoff, S., Mauerhan, J., Meyer, L., Moulataka, J., Muzic, K., Najarro, F., Schuster, K., Straubmeier, C., Thum, C., Witzel, G., **Zamaninasab, M.**, Zensus, A.: "*Coordinated mm/sub-mm observations of Sagittarius A\* in May 2007*", JoP: Conference Series, Volume 131, Issue 1, 2008.

- Eckart, A., Schödel, R., Baganoff, F. K., Morris, M., Bertram, T., Dovciak, M., Dowries, D., Duschl, W. J., Karas, V., König, S., Krichbaum, T., Krips, M., Kunneriath, D., Lu, R.-S., Markoff, S., Mauerhan, J., Meyer, L., Moulataka, J., Muzic, K., Najarro, F., Schuster, K., Sjouwerman, L., Straubmeier, C., Thum, C., Vogel, S., Wiesemeyer, H., Witzel, G., **Zamaninasab, M.**, Zensus, A.: "*Coordinated multi-wavelength observations of Sgr A\**", JoP: Conference Series, Volume 131, Issue 1, 2008.

- Eckart, A., Schödel, R., García-Marín, M., Witzel, G., Weiss, A., Baganoff, F., Morris, M. R., Bertram, T., Dovciak, M., Downes, D., Duschl, W., Karas, V., König, S., Krichbaum, T., Krips, M., Kunneriath, D., Lu, R.-S., Markoff, S., Mauerhan, J., Meyer, L., Moulataka, J., Muzic, K., Najarro, F., Pott, J.-U., Schuster, K., Sjouwerman, L., Straubmeier, C., Thum, C., Vogel, S., Wiesemeyer, H., **Zamaninasab, M.**, Zensus, A.: "*Probing Sagittarius A\* and its Environment at the Galactic Centre: VLT*"

*and APEX Working in Synergy*", The Messenger, vol. 133, 2008.

- Eckart, A., Witzel, G., Kunneriath, D., König, S., Straubmeier, C., Bertram, T., **Zamaninasab, M.**, Schödel, R., Muzic, K., Tremou, E., Meyer, L., Rost, S., Vogel, S., Wiesemeyer, H., Sjouwerman, L., Herbst, T.: *"Prospects for observing the Galactic Center: combining LBT LINC-NIRVANA observations in the near-infrared with observations in the mm/sub-mm wavelength domain"*, Optical and Infrared Interferometry: Proceedings of the SPIE Conference, Volume 7013, 70134L-70134L-12, 2008.
- Eckart, A., García-Marín, M., Witzel, G., König, S., Kunneriath, D., Straubmeier, C., **Zamaninasab, M.**: *"Coordinated multi-wavelength observations of the Dark Mass at the Center of the Milky Way"*, Proceedings of "Identification of dark matter 2008". Stockholm, Sweden, 38, 2008.

# Lebenslauf

## Persönliche Angaben

Name: Mohammad Zamaninasab  
Anschrift: I. Physikalisches Institut, Universität zu Köln  
Zülpicher Str. 77, 50937 Köln  
Email: zamani@ph1.uni-koeln.de  
Geburtsdatum und -ort: 14.08.1982 in TorbateJam, Iran

## Ausbildung

Seit Mai 2007 Promotionstudent an der Universität zu Köln und dem  
Max-Planck-Institut für Radioastronomie  
wiss. Betreuer: Prof. Dr. Andreas Eckart  
2005 - 2007 Master der Physik an der Isfahan University of Technology,  
Isfahan, Iran  
wiss. Betreuer: Prof. Behrouz Mirza  
Titel: „Ruppeiner Geometry of Reissner-Nordström Black Holes“  
2000 - 2005 Bachelor der Physik an der Isfahan University of Technology,  
Isfahan, Iran  
wiss. Betreuer: Prof. Behrouz Mirza  
Titel: „Cosmological Expansion and Its Effect on Small Systems“  
1996 - 2000 National Organization for Development of Exceptional  
Talents (NODET) High School  
Birjand, Iran

## Stipendium

Seit Mai 2007 Stipendium der *International Max Planck Research School (IMPRS)*  
for Astronomy and Astrophysics